Extension of Upper Limit Servers and spectral analysis of the X-ray binary GRO J1744−28

Master's Thesis in Physics

Presented by
Ole König

Wednesday 31st July, 2019

Dr. Karl Remeis-Sternwarte & ECAP
Friedrich-Alexander-Universität Erlangen-Nürnberg

Supervisor: Prof. Dr. Jörn Wilms

Abstract

This thesis is about applications in the field of X-ray astronomy. It is divided into a software development and data analysis part.

The *Upper Limit Servers* allow the user to generate long-term lightcurves of X-ray sources. They combine historical data and calculate upper limits in real-time. A web-based front-end provides facile querying, plotting and downloading of the data. They utilize data from 12 satellites including current observatories such as *XMM-Newton*, back to *ROSAT*, *Einstein*, *Ariel V* and *Uhuru*. This enables the user to query 50 years of X-ray data and, for instance, study outburst behavior of transient sources. Part I of this thesis describes the software layout, database format, as well as nine X-ray missions, which I implemented. In particular, the implementation of catalog calls, image footprints, point spread functions, and vignetting is described. The count rate is converted to a flux by approximating the spectral shape with an absorbed power-law or black body. In order to outline possible applications of this software, I interpret four lightcurves.

In the second part, the spectral analysis of the low-mass X-ray binary GRO J1744−28 is presented. The ∼29 ks data was taken with the Nuclear Spectroscopic Telescope Array (NuSTAR) in 2017 February, during the source's fourth reactivation phase after three years of quiescence. No bursts are visible in the *NuSTAR* lightcurve, likely due to a low accretion rate, which corresponds to a luminosity of $3.2 \times 10^{36}\ (D/8\ \mathrm{kpc})^2\ \mathrm{erg\,s^{-1}}$ (3–50 keV). This places the source in the sub-critical regime. The spectral shape is modeled with an absorbed power-law with exponential cut-off and additional iron line component. I perform a detailed cyclotron line search in the phase-averaged as well as phase-resolved spectra using statistical methods. I do not find a cyclotron resonant scattering feature in these low-flux data. The upper limit for such a line is not consistent with the values found in earlier observations, taken at higher luminosity. However, Monte Carlo simulations show that a unique statistical statement is not possible based on these low signal to noise data.

Zusammenfassung

Diese Masterarbeit gliedert sich in in einen Software und Datenanalyse Teil.

Im ersten Teil werden die "Upper Limit Server" beschrieben, welche einen Web-basierten Zugang zu Langzeit-Lichtkurven ermöglichen. Sie kombinieren historische Röntgendaten verschiedenster Missionen mit der Echtzeitberechnung von oberen Flussgrenzen. Insgesamt greifen die Server auf Daten von zwölf Röntgenmissionen zurück. Unter ihnen sind aktuelle Satelliten wie *XMM-Newton*, ältere Missionen wie *ROSAT* und *Einstein*, und mit *Ariel V* und *Uhuru* und damit bis hin zu den Anfängen der Weltraum-basierten Röntgenwissenschaft. Der Aufbau der Software, die Datenbanken, sowie Katalogaufrufe für neun Satelliten, welche ich implementiert habe, werden beschrieben. Des Weiteren werden Details zu Punktspreizfunktion, der Berechnung des Fußabdrucks des Bildes und Vignettierung gegeben. Unter der Annahme eines Potenzgesetzes oder Schwarzkörperstrahlung wird die Zählrate zu einem Fluss approximiert. Um die wissenschaftlichen Anwendungsmöglichkeiten dieser Software, wie beispielsweise Transient Detektion, oder Ausbruchstudien, darzustellen, werden vier Lichtkurven interpretiert.

Im zweiten Teil wird eine Spektralanalyse des Röntgendoppelsternsystems GRO J1744−28 präsentiert. Die Daten wurden mit dem Weltraum-basierten Teleskop *NuSTAR* im Februar 2017 aufgenommen, wobei die Daten den vierten aufgezeichneten Ausbruch dieser Quelle beinhalten. Es wurde in dieser Arbeit festgestellt, dass sich die Quelle mit einer Luminosität von $3.2 \times 10^{36}\ (D/8\,\mathrm{kpc})^2\,\mathrm{erg\,s^{-1}}$ (3–50 keV) in sub-kritischem Regime befindet. Die fehlenden Typ II Ausbrüche in der Lichtkurve können mit der resultierenden niedrigen Akkretionsrate erklärt werden. Das Kontinuum wird mit einem absorbiertem Potenzgesetz mit exponentiellem Abbruch und zusätzlicher Gaußförmiger Eisenlinie modelliert. Es wird gezeigt, dass keine signifikante Zylotronlinie im Spektrum vorhanden ist. Die obere Grenze einer solchen Linie ist nicht konsistent mit früheren Beobachtungen, jedoch kann eine genauere, statistische Aussage aufgrund des niedrigen Signal-Rausch-Verhältnisses nicht angegeben werden.

Contents

Chapter 1

Introduction

Earth's atmosphere shields Earth and mankind from cosmic radiation. So, unlike optical astronomy – being thousands of years old – X-ray astronomy is a relatively new science. It is bound to experiments, which facilitate operation in space or in the upper atmosphere. In 1929, Edward Hulburt proposed a theory on how to mount an X-ray detector on a rocket. However, it took 20 years until 1949 when the United States launched a German V2 rocket. The first and brightest celestial X-ray source was detected (Friedman et al., 1951): The Sun. In 1962, sounding rocket experiments under the lead of Riccardo Giacconi – the father of X-ray astronomy and later honored with the Nobel price – detected Scorpius X-1, the brightest extra-solar source (Giacconi et al., 1962). Two years later, Cygnus X-1 was discovered and widely accepted as first Black Hole candidate (Bleeker et al., 1967). Eventually scientists realized that rocket experiments (Fig. 1.1) are impractical due to their short observation time. They were subsequently followed first by balloons and then by space-based observatories (Pounds, 2002):

Vela 5B was part of the Vela satellite series by the U.S. Air Force. They were primarily designed to observe whether the Soviet Union fulfills the 1963 *Partial Nuclear Test Ban Treaty*. In 1967, Vela 4 and Vela 3 discovered a flash of gamma radiation. The researchers could pinpoint the origin of the event to outer space, which lead to the discovery of the first gamma-ray burst (Conner et al., 1969) – the most energetic phenomena in the universe. *Vela 5B* flew from 1969 May 23 until 1979 June 19, incredible 10 years for such an old mission. Due to its long lifetime, *Vela 5B* enabled the unique studies of early long-term variability of X-ray binaries and transients (e.g. Priedhorsky et al., 1983).

Today's X-ray astronomy kick-started in 1970 with the launch of *Uhuru*, also lead by Giacconi. *Uhuru* was the first satellite entirely dedicated to X-ray astronomy. It was launched on 1970 December 12 from the San Marco platform in Kenya and flew until 1973 March. The start date was the seventh anniversary of the Kenyan independence. NASA named the satellite *Uhuru*, the Swahili word for *freedom*. Assembled were two sets of proportional counters with an energy range 2–20 keV. The *Uhuru* mission was the first to perform a comprehensive and uniform all-sky survey which resulted in the discovery of 339 X-ray sources, famously dubbed the "4U sources". Among it are objects like supernova remnants and active galactic nuclei (Forman et al., 1978), but *Uhuru* also

discovered the diffuse X-ray emission from galaxy clusters (Turner & Geller, 1980). The pointing capability was a few arcmin^2 for bright sources with a spatial resolution of $\sim 30'$ (Giacconi et al., 1971).

Scientific and public interest in these highly energetic and violent objects was high and new satellites were build at an astonishing pace. After *Uhuru*, *Ariel V* was the next big X-ray satellite. From 1974 October 15 until 1980 March 14 it continuously monitored the sky and exploited new fields, like X-ray pulsars (Rosenberg et al., 1975) and AGN variability (Marshall et al., 1981). The satellite was spinning and constantly integrating over a period of $5\frac{1}{2}$ years – with a telemetry rate of only 1 bit/s (Whitlock et al., 1992).

The High Energy Astronomy Observatory was the first of a series of large NASA X-ray missions. *HEAO-1* surveyed the entire X-ray sky in the 0.2 keV to 10 MeV band for almost three times from 1977 August 12 until 1979 January 9, especially near the ecliptic poles. Approximately at the same time, the team of German astrophysicist Joachim Trümper surprised scientists by the straight-forward measurement of the magnetic field of the neutron star Hercules X-1 (Trümper et al., 1978) – universes strongest dynamos. The second mission of this series, and again, Giacconi was one of the pushing figures, was *Einstein* (HEAO-2). The *Einstein* observatory flew from 1978 November 12 until 1981 April and was the first fully imaging X-ray telescope in space (Giacconi et al., 1979). With a resolution of only a few arcseconds and a 100× better sensitivity – unprecedented at the times – it revolutionized X-ray science. The *Einstein* satellite was the first to study the spectra of supernova remnants with high spectral resolution (Mathewson et al., 1983), studied the coronal emissions of stars (Ayres et al., 1981) and detected the X-ray jets in Cen A (Feigelson et al., 1981) and M87 (Schreier et al., 1982). Before *Einstein*, X-ray instruments used pin-hole cameras with proportional counters and had very poor spatial resolution. The introduction of grazing incidence telescope (Fig. 1.3) and the ability to focus X-rays, resulted in the first detailed images with arcsecond resolution (one 3600$^{\text{th}}$ of a degree).

The subsequent European *EXOSAT* mission lead to major studies of X-ray bursts, and the discovery of Quasi-Periodic Oscillations (Angelini et al., 1989). It operated from 1983 May 26 to 1986 April 9 and made 1780 observations of a variety of astronomical objects. A vast amount of other discoveries were made in the early 1980s, such as microquasars, relativistic jets, and superluminal motion (see e.g. Mirabel & Rodríguez, 1994).

Also the Japan Aerospace Exploration Agency (JAXA) develops X-ray satellites. *GINGA* ("galaxy") was Japan's third X-ray mission and flew from 1987 February 5 until 1991 November 1. *GINGA* discovered, for instance, intense iron line emission from our Galactic center region (Koyama et al., 1989), and gave evidence for iron features in Seyfert galaxies probing reprocessing by cold matter (Pounds et al., 1990).

Joachim Trümper also led the development of the German satellite *ROSAT* (Trümper, 1982), which monitored the entire X-ray sky between 1990 June and 1999 February with a $\sim$ 100 times better resolution compared to *Uhuru*. Six months of the mission were dedicated to an all-sky survey (RASS) and yielded the 2RXS catalog, increasing the number of known sources from 840 to 135 000. The X-ray telescope utilized four nested Wolter mirrors – the largest and with a roughness of $<$0.3 nm smoothest mirrors at the

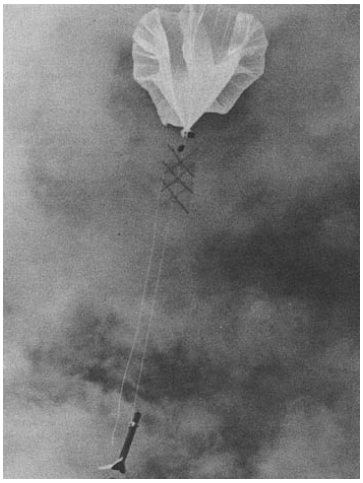

Figure 1.1: A "rockoon" – a balloon with a rocket in 1956 (Corliss, 1971)

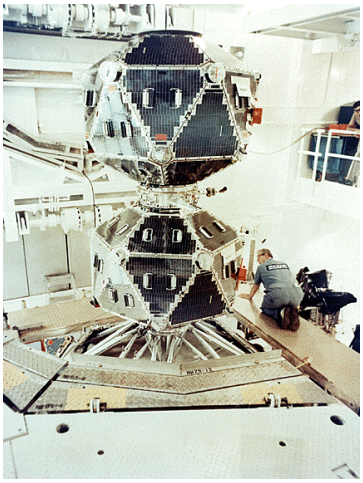

Figure 1.2: *Vela 5B* in the clean room (NASA)

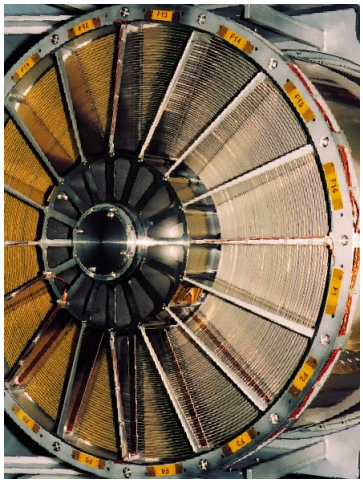

Figure 1.3: The nested mirrors on *XMM-Newton* (ESA)

time – and operated in the soft energy band from 0.1–2.5 keV (Aschenbach, 1988). In 1996, during the passage of comet Hyakutake, *ROSAT* found that also comets exhibit X-ray radiation (Lisse et al., 1996).

Further improvement came with Japanese Advanced Satellite for Cosmology and Astrophysics (*ASCA*), which used CCD detectors far more efficiently than the old read-out procedure (Tanaka et al., 1994; Serlemitsos et al., 1995). As Japan's fourth X-ray mission, it performed scientific measurements from 1993 February 20 until 2000 July 14 and was a pioneer by having imaging capability with a broad energy range, at the same time good spectral resolution and large effective area. In fact, *ASCA* was the first imaging satellite covering the hard energy band above 2 keV with flux limits $\sim 10^{-13}$erg cm^{-2}s^{-1}. This enabled *ASCA* to do, for instance, sophisticated studies on the Fe Kα line in AGN or stars (Doschek et al., 1980; Kormendy & Richstone, 1995), and study galaxy clusters (Reiprich & Böhringer, 2002).

Noteworthy is also the Rossi X-ray Timing Explorer (RXTE), which operated from 1995 until 2012, and discovered kilo-hertz quasi periodic oscillations (e.g. Miller et al., 1998). Also some planets of our solar system emit X-rays in aurorae, and most of them reflect Sun's X-ray radiation (Bhardwaj et al., 2007). *Chandra* made discoveries of Venus (Dennerl et al., 2002) and monitored the polar aurora of Jupiter (Gladstone et al., 2002).

Nowadays, we live in the "Golden Age" of X-ray astronomy. New discoveries, like the electromagnetic counterpart in gravitational wave events (Troja et al., 2017), or the relativistic wind behavior of AGN (King & Pounds, 2003) keep on challenging the field. With numerous missions such as *Chandra* and *Swift* by the NASA, the X-ray Multiple Mirror Mission (*XMM-Newton*) and the International Gamma-Ray Laboratory (*INTEGRAL*) by ESA, as well as the recently launched *Spectrum X-Gamma*, researchers are now capable to study sources with unprecedented precision.

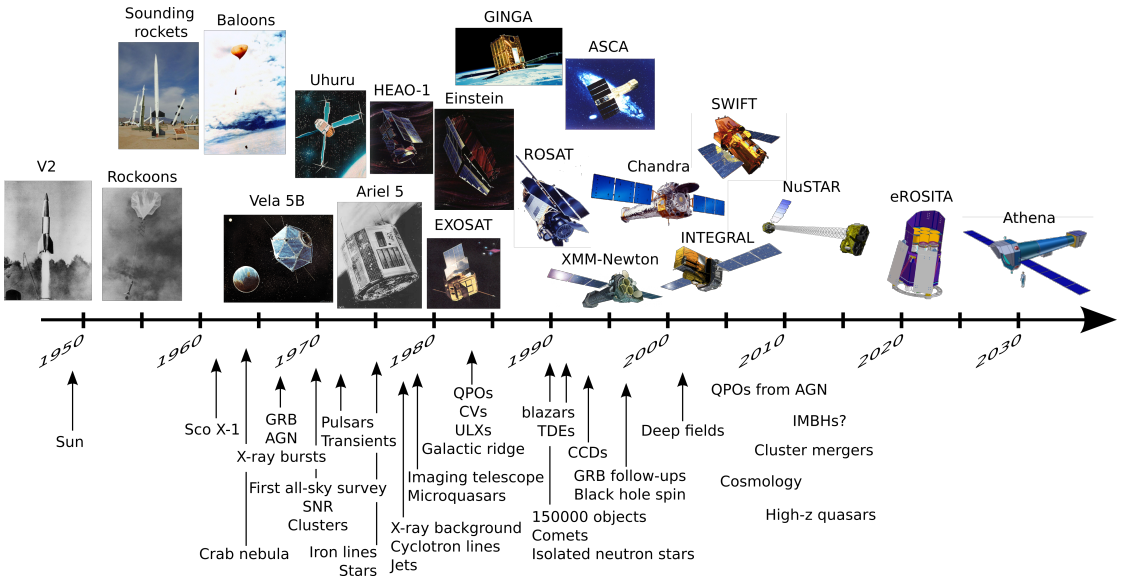

Figure 1.4: A brief history of X-ray discoveries

NASA's Nuclear Spectroscopic Telescope Array (*NuSTAR*), for instance, was launched on 2012 June 13 and is the first focusing high-energy telescope. Its outstanding capability is a focusing ability in an energy range from 3–79 keV under the use of a deployable mast which increases the focal length to 10 m. *Chandra* and *XMM-Newton*, for instance, both launched in 1999, have a much more narrow energy band of 0.1–10 keV and 0.1–12 keV, respectively. The inherited low background rate and use of focusing optics increases *NuSTAR*'s sensitivity by orders of magnitude[1] compared to old coded mask techniques (e.g. *INTEGRAL*/IBIS, Ubertini et al. 2003). The technical documentation of *NuSTAR* can be found in Harrison et al. (2013). The 350 kg satellite consists of two co-aligned grazing-incidence X-ray telescopes with two focal plane modules (FPM A and FPM B). It is deployed into a 600 km, near-circular orbit with 5° inclination. The Wolter-I type telescopes comprise of 133 nested multilayer-coated shells each, which focus the incoming light onto the the focal plane modules. Except for a small detector calibration constant, which is in the order of a few percent, the data of the two telescopes can be added and analyzed simultaneously. *NuSTAR* has a temporal resolution of 2 μs which allows to do phase-resolved spectroscopy of rapidly rotating neutron stars. The angular resolution is 18″ (FWHM) with a 10′ FOV at 10 keV. Is has a moderate energy resolution of 400 eV (FWHM) at 10 keV which does not allow analyzing detailed spectroscopic line abundances (e.g. resolving Fe Kα from Fe Kβ). *NuSTAR*'s energy calibration can have uncertainties of up to 40 eV (one bin) with a gain drop of 0.2%/year (Miyasaka, 2019). Therefore, for detailed spectroscopic line fitting one needs to introduce a "gain shift" which accounts for the calibration uncertainty.

[1] Sensitivity (6–10 kev) (10^6 s, 3σ, $\Delta E/E = 0.5$) $= 2 \times 10^{-15}$ erg cm^{-2}s^{-1}, Background in HPD (10–30 keV)=1.1×10^{-3} cts sec^{-1} (Harrison et al., 2013)

It is obvious that a large amount of data has accumulated in the past decades. This enormous data set is still not fully exploited and it proves essential to study the data of all successive X-ray missions to reveal long-term variability patterns. Part I of this thesis describes a tool which enables combining the data of most of these satellites.
Among many others, one class of celestial objects – neutron stars – remain a yet unsolved puzzle. The main proxy to reveal their properties are spectral analyses through space-based observatories. Part II covers the data analysis of the X-ray binary system GRO J1744−28. This low-mass X-ray binary underwent a weak outburst in 2017 February, which was observed with *NuSTAR*. In Ch. 2, I give a general introduction into the physics of X-ray binaries. Chapter 3 describes the spectral analysis of the 2017 *NuSTAR* data. I conclude my thesis in Ch. 4. The glossary contains a description of relevant terms used in astrophysics and appendix A recapitulates the relevant statistics.

Part I

Upper Limit Servers

1.1 Motivation

X-ray sources can be extremely variable on times scales of seconds to decades or even longer, and with the flux sometimes ranging over several orders of magnitude. Some transient sources exhibit regular outbursts, others – like tidal disruption events – are highly irregular. Nowadays, with X-ray science being over half a century old, it becomes exceedingly more interesting to study the long-term behavior of any X-ray source. The lifetime of a space-based observatory is, however, short compared to astronomical scales, and usually in the order of 5–10 years. Therefore, it is inevitable to combine data of several instruments in order to resolve variability patterns which are decades long. To study this variability, infer source type and its properties, the lightcurve has proven to give valuable information. With the fast increase in the amount of X-ray missions, it becomes, however, difficult to get a comprehensive overview of all available data. Furthermore, due to old data formats, missing pipelines, coordinate system changes, and incomplete documentation, extracting data from old satellites can be sometimes cumbersome and time-consuming.
As an illustration of the diagnostic capability of lightcurves, Fig. 1.5 shows the brightest and first detected quasar on the sky: 3C 273. Due to its brightness, this sources serves

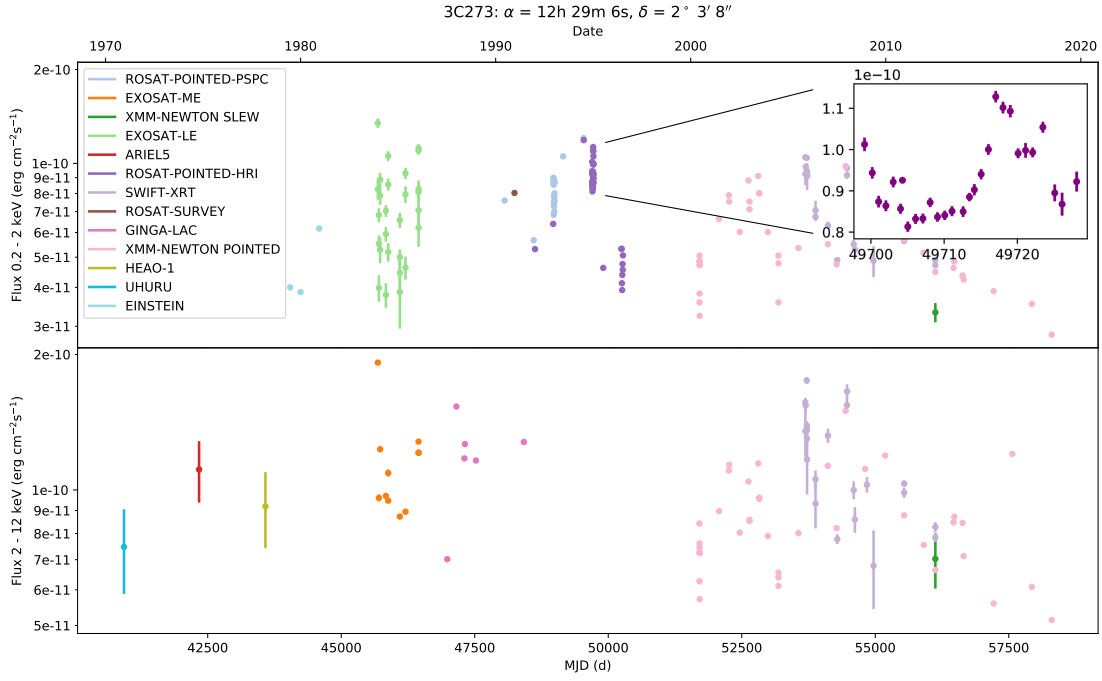

Figure 1.5: Lightcurve of the quasar 3C 273 ranging over 48 years. The inset shows flux variation in *ROSAT* HRI data from 1994 December until 1995 January. In order to tranform count rates to flux a power-law spectral model of slope 1.7 and galactic absorption of 3×10^{20} cm^{-2} is assumed (Madsen et al. 2015 find $\Gamma = 1.646(6)$, $N_{\rm H} = 1.79\times10^{20}$ cm^{-2}).

as calibration source for many missions and thus exhibits numerous data points. Only by combining these data, one can make statements about the long-term behavior. The lightcurve of 3C 273 shows, for instance, that this source is roughly stable between $(5–12)\times10^{-11}\,\mathrm{erg\,cm^{-2}s^{-1}}$ over the past 48 years. However, within this flux range, the source can indeed show variability patterns (see inset of Fig. 1.5), which can lead to more sophisticated studies (e.g. Soldi et al., 2008).

So far, no generalized tool is available which automatically queries the data of the past X-ray missions. For this reason, the *Upper Limit Servers* (ULS) were developed. They are a new web-based tool which enables a quick access to the data of twelve past and current X-ray missions, without the issue of browsing through several catalogs in person, or installing software. The algorithm filters the catalogs of the available X-ray missions, so the tool can be used to give a general overview of existing archival data. However, it can be the case that the image counts were not sufficient to identify a source, and the catalog therefore does not list a detection. In fact, there is much more data publicly available than listed in the catalogs. In order to fully exploit the available data, the ULS provide a framework which calculates flux upper limits at these positions. Adding upper limits to the lightcurve provides large diagnostic capability, for instance, studying the long-term flux variation of a source. In quiescence states, sources are generally not observed, and upper limits provide the only possibility to estimate their fluxes in these periods. A further major application is the study of outbursts in transient sources, whereby upper limits can help constraining the flux before an outburst.

Section 1.2 describes the design of the ULS. A mathematical description of the upper limit calculation is given in Sect. 1.2.1. Section 1.2.2 shows how the ULS perform the count rate to flux conversion. The catalog calls are described in Sect. 1.2.3, followed by the footprint computation (Sect. 1.2.4), and database implementation (Sect. 1.2.6). Section 1.3 shows the front-end of the ULS. Furthermore, this chapter describes each individual mission server in Sect. 1.4. An overview of the mission parameters can be seen in Table 1.1 and a scientific application of the tool is given in Sect. 1.5. In Appendix A.3, I describe the mathematical formalism of upper limits. The work here presented has been conducted during a six month traineeship at the European Space Astronomy Centre (ESAC) in Madrid under the supervision of Richard Saxton and Peter Kretschmar.

1.2 Design

The user specifies the input coordinates or a name of a chosen source. Auxiliary, a spectral model, absorption column and the output energy bands are selected. This is necessary to convert the count rate values to a flux. For each selected mission, a database query finds all available images in which the coordinates match the footprint. In other words, the query finds all images, which contain data at the input position, and returns a list with the corresponding observation IDs. This list of observation IDs is reconciled with the existing catalogs: If the ID already exists in a catalog, the count rate is adopted. Otherwise, the image is used to compute an upper limit (taking exposure, background,

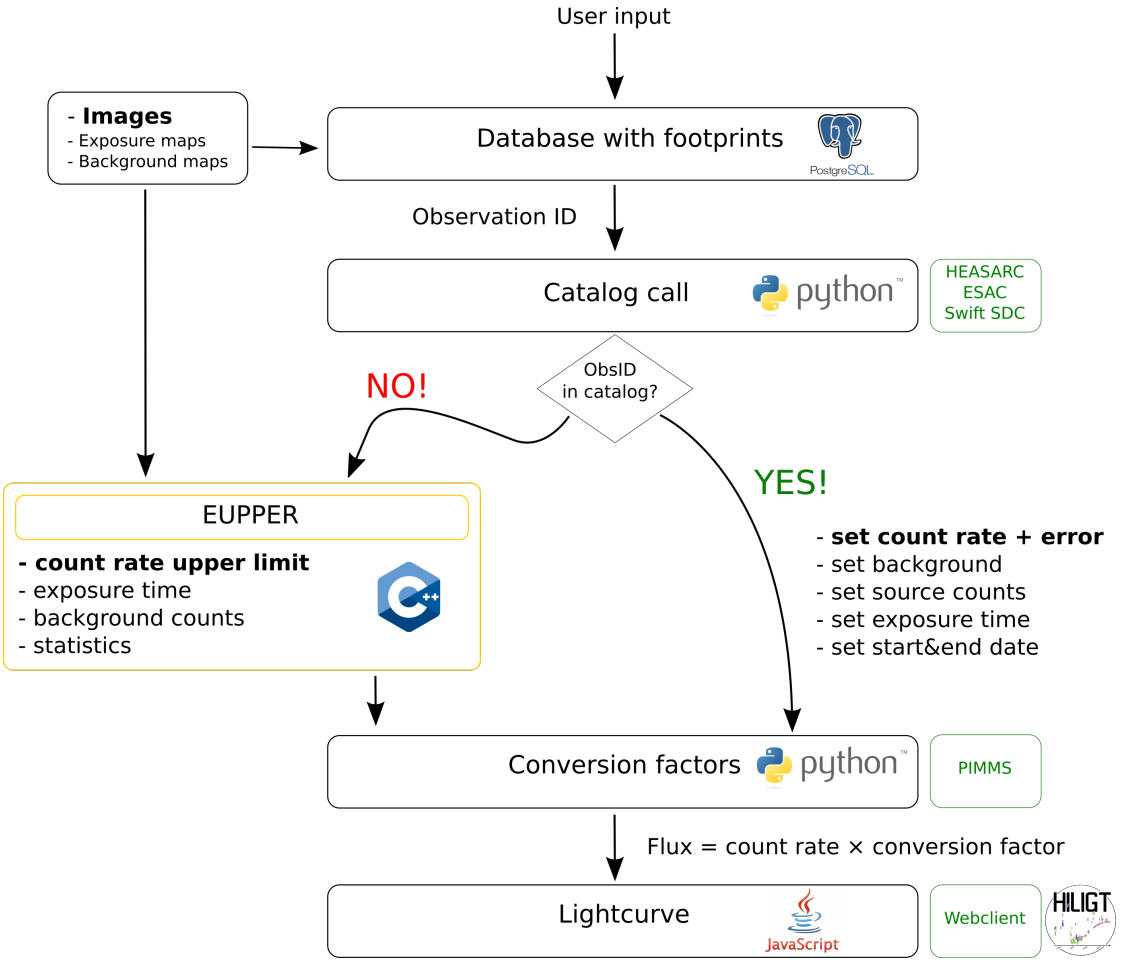

Figure 1.6: A basic scheme of the ULS: The lightcurves exhibit data from catalogs in combination with upper limits, which are computed from the images.

vignetting effects and the point spread function into account). Finally, a conversion factor converts the count rate into a flux, which is displayed in the lightcurve. These data can be either queried from a web-interface in the browser, or with a terminal-client from the command line. A scheme of the ULS can be seen in Fig. 1.6.

1.2.1 Calculation of upper limits

The upper limits are calculated with the EUPPER task, which is available within the *XMM-Newton* SAS (Gabriel et al., 2004, since SAS 16).
Let N be the total number of counts in the source region A_S. A_S is assumed to be radially symmetric and depends on the point spread function (PSF) and angular resolution of the mission. The source radius r of each mission is hard-coded into the ULS code. It typically takes a value of about 80% of the encircled energy fraction (see below). The

total counts N are the sum of source and background counts in the source area πr^2.
In order to obtain the source counts $S = N - B$, the background counts B in background area A_B of a given position on the sky is needed. Ideally, this is done by analyzing a background map, whereby the counts of the background map in the source area ($A_B = A_S$) are summed up. If no background map is available, two circles of radius $2.5r$ and $3r$ are laid around the source. The counts within this annulus are then taken as background counts. One has to ensure that source and background counts originate from the same area. Therefore, the background is normalized by multiplying it with the area ratio A_S/A_B.
To calculate the count **rate**, one has to divide the background subtracted counts by the exposure time. The exposure is taken from the exposure map at the specified position. If no exposure map is available, the exposure is taken from the header of the FITS image and multiplied by the vignetting factor. This vignetting effect is due to the geometry of the telescope, which induces a degrading illumination of the detector at the rims of the image. The vignetting reduces the effective area (and hereby the exposure time) as a function of off-axis angle. It takes values from zero to one and can often be assumed to be linear (see example for *Einstein* IPC in Fig. 1.11a). In order to correct the count rate for the PSF, one has to divide the source counts by the encircled energy fraction (EEF). The EEF gives the percentage of energy which is encircled in a given radius. It depends entirely on the point spread function of the instrument. The ULS take into account that the EEF changes as a function of source radius and off-axis angle, but assume that it does not change between images of the same instrument. Furthermore, they do not account for the energy dependence of the PSF. This is impossible from the image because it does not exhibit information about the energy of the impacting photons. One would need an event list to reconstruct the energy of each photon.
The background subtracted count rate ($\mathrm{cts\,sec^{-1}}$) is then computed by correcting the source counts $S = N - B$ for the EEF and dividing it by the (vignetting corrected) exposure time:

$$CR = \frac{S}{\mathrm{EEF} \cdot \mathrm{exposure} \cdot \mathrm{vign}} \tag{1.1}$$

The error propagation and thus the final upper limit depends on the number of counts. Kraft et al. (1991) showed that the application of classical Gaussian statistics is unsuitable in the case of low counts. The threshold to divide the two regimes is set to 80 counts in the EUPPER code.

For high counts above $N = 80$ classical statistics are applied. The error is computed by

$$\text{Upper limit } (\mathrm{cts\,sec^{-1}}) \;=\; \frac{max(S,\,0) + f \cdot \sqrt{N+B}}{\mathrm{EEF} \cdot \mathrm{exposure}} \tag{1.2}$$

with $\sigma_S = \sqrt{N+B}$ being the error on the background subtracted counts ($S = N - B$). These are obtained by linear Gaussian error propagation under the assumption of a Poissonian error on N and B. The factor f can be 1,2 or 3 depending on the desired 1,2 or 3-σ confidence level (68.2%, 95.5% or 99.7%).

In the case of low counts, Bayesian statistics are applied. Let S be again the desired number of counts which originate from the source and B the known number of background counts (Attention: S also comes from a Poisson distribution and does not necessarily equal the **real** number of source counts). The (posterior) probability function is given by Bayes's theorem:

$$f_{N,B}(S) = p(S) \cdot P_S(N) \tag{1.3}$$

$P_S(N)$ is called the *conditional distribution function* and is given by a Poisson distribution for $S + B$ (according to the central limit theorem the Poisson distribution becomes Gaussian for $N \to \infty$ and one can apply Eq. 1.2). $p(S)$ is called the *prior function*. It can be shown that the posterior probability function $f_{N,B}(S)$ does not heavily depend on $p(S)$. Therefore, one can assume a uniform, positive distribution, described by a Heaviside function. Using the knowledge that $P_S(N)$ is Poisson-distributed and evaluating the Heaviside function, one obtains

$$f_{N,B}(S) = \underbrace{C}_{\text{Normalization}} \cdot \underbrace{\frac{e^{-(S+B)}(S+B)^N}{N!}}_{\text{Poisson distribution}} \tag{1.4}$$

with the normalization constant

$$C = \left[\int_0^\infty \frac{e^{-(S+B)}(S+B)^N}{N!} dS \right]^{-1} = \left(\sum_{n=0}^{N} \frac{e^{-B} B^n}{n!} \right)^{-1} \quad . \tag{1.5}$$

The integral borders are shifted from $(-\infty, +\infty)$ to $[0, +\infty)$ due to the Heaviside function from $p(S)$. For a given confidence level (CL) the confidence interval (see Appendix A.3) can then be computed by

$$CL = \int_{S_{min}}^{S_{max}} f_{N,B}(S) dS \tag{1.6}$$

and the appropriate upper limit can be obtained by solving numerically for S_{max}. The count rate upper limit ($\mathrm{cts\,sec^{-1}}$) is then converted into flux ($\mathrm{erg\,cm^{-2}s^{-1}}$) by applying the mission specific conversion factor.

1.2.2 Count rate to flux conversion

Photon counting detectors, such as CCDs, have counts as fundamental measurement property. The number of source counts C in detector channel h within exposure T is given by

$$S(h) = T \int_0^\infty \mathrm{RMF}(h, E) \cdot \mathrm{ARF}(E) \cdot F(E)\, dE \quad . \tag{1.7}$$

$\mathrm{ARF}(E)$ describes the effective area of the optics, including the detector efficiency. The detector response $\mathrm{RMF}(h, E)$, often called the response matrix, gives the probability of detecting a photon of energy E in channel c. More details can be found, for instance, in Arnaud et al. (2011). The physically important parameter in Eq. 1.7 is the flux density

$F(E)$ of the observed source. This quantity is, however, difficult to obtain because generally Eq. 1.7 cannot be inverted. In spectral analyses, like Sect. 3.3.1, one therefore uses χ^2-minimization (see Appendix A.1) in order to find the model best suited to fit the data.[2]

Extracting spectra and doing fits for each image is beyond the scope of the ULS. Therefore, the user selects a spectral model and the ULS produce the flux *under the assumption* of this model[3]. The ULS use the PIMMS software (Mukai, 1993) which solves Eq. 1.7 and calculates the count rate to flux conversion factors. I extract conversion factors for each filter, spectral model and spectral index/temperature configuration (for efficiency reasons the conversion factors are hard-coded into the ULS code). They can be found in Table B.3 in the appendix.

The data of the different satellites can only be compared if they are given for the same flux range. Therefore, the ULS interpolate (sometimes extrapolate) the energy bands of the different satellites onto three pre-defined energy bands with the use of the conversion factors: The *soft* band equals 0.2–2.0 keV, *hard* band equals 2.0–12.0 keV, and *total* band equals 0.2–12.0 keV. The missions *Vela 5B*, *Uhuru*, *Ariel V* and *HEAO-1* are not included in PIMMS. The literature only provides a conversion factor for a Crab-like power-law spectrum ($\Gamma = 2$) in the missions energy band. Generally, this range is different from the ULS bands. However, all missions have energy ranges inside the 2–12 keV *hard* band of the ULS and are thus approximated by

$$CF_{2\text{–}12\,\mathrm{keV}} = CF_{\text{Mission band}} \cdot \frac{\mathrm{Flux}_{2\text{–}12\,\mathrm{keV}}}{\mathrm{Flux}_{\text{Mission band}}} \tag{1.8}$$

The quantity $\mathrm{Flux}_{2\text{–}12\,\mathrm{keV}}$ is computed with the Interactive Spectral Interpretation System (Houck, 2002, ISIS version 1.6.2-43)[4]. Since I only have knowledge of this particular power-law model conversion factor, the output spectral model will always be a power-law with slope two, indifferent of the user's choice on the website. I take the small N_H dependence into account (via `tbabs`) and include, unless stated otherwise, a systematic error of ∼20% on the conversion factors of these missions.

1.2.3 Catalog calls

If the observation ID, which is obtained from the database query, already exists within an existing catalog, the ULS server adopts this count rate. NASA's *Goddard Space Flight Center* provides the most abundant amount of catalogs and for all missions implemented within this work, the ULS use the High Energy Astrophysics Science Archive Research

[2] A further problem is the background contamination in every real physical measurement due to e.g. thermal noise and cosmic radiation. The number of **observed** counts does not equal $S(h)$ but is given by $N(h) = S(h) + B(h)$, where $N(h)$ are the observed counts in channel h, and $B(h)$ are the background counts. Therefore, the estimated number of source counts is $\tilde{S}(h) = N(h) - B(h)$ with Poissonian error $\sigma_{\tilde{S}} = \sqrt{N(h) + B(h)}$

[3] The parameter choices are: Bands = 0.2–2 keV, 2–12 keV, 0.2–12 keV, upper limit significance = 1,2, or 3σ, spectral model = power-law or black body with $\Gamma = 0.5, 1.0, 1.5, 1.7, 2, 2.5, 3, 3.5$, $k_B T = 60, 100, 300, 1000$ eV, respectively, and $N_\mathrm{H} = (1, 3, 10) \times 10^{20}\,\mathrm{cm}^{-2}$.

[4] $\mathrm{Flux}_{2\text{–}12\,\mathrm{keV}}$=`energyflux(2,12;cgs)` with model `tbabs*powerlaw`

Center (HEASARC) to access the data. The back-end calls the HEASARC servers on-the-fly, which implies issues with the ULS in case of malfunction at the HEASARC. In order to receive the count rates from the catalogs, a cone search around the input coordinates is performed. It is important to choose the catalog search radius such that no sources are missed. However, also not too many sources should be identified with the same position on the sky. The corresponding catalog search radii of the HEASARC serve as orientation for the cone search radii of the ULS. All search radii can be found in Table 1.1 and an example catalog call is given in Appendix B.1.

1.2.4 Footprint calculations

The so-called footprint encircles the sky region where the image exhibits reasonable data and for which the ULS are able to compute upper limits. It is important to distinguish the rectangular image from the actual illuminated part (i.e. the data): The footprint constrains the border of the illuminated part within the image. The ULS query the SQL database with the given world coordinates (right-ascension, declination in J2000) and look for all images, for which the coordinate matches the footprint shape. These are parsed to EUPPER (Sect. 1.2.1).

Stoehr (2008) provides a sophisticated footprint finder, however, it does not work reliable with low-counts images. Therefore, I wrote an algorithm in order to calculate footprints of the illuminated region of FITS images. This algorithm follows a relatively simple approach which turns out to work very well with old mission images like *Einstein*, but also with newer missions like *XMM-Newton* slew data. The output is the calculated footprint as DS9 region file or SQL readable table. For the missions *EXOSAT* and *Einstein* it transforms the sky positions of epoch B1950 to J2000 (see Sect. 1.2.5). The basic steps of the algorithm are following:

① The algorithm starts in the lower left image corner and walks from the edge into the image. As soon as it hits an illuminated (non-zero) pixel, it puts a box (box size `b`) around the pixel and computes the average. If the value surpasses a threshold `t`, the pixel is accepted as footprint point. If not, the algorithms steps further into the image until it hits the opposite border.

② Walk the bottom x-axis to the right (with increment `i`) and repeat ①.

③ Walk the upper x-axis in the reversed direction (repeating ①&②) to ensure a closed shape of the footprint.

④ When all footprints are calculated it reads the `RADECSYS` keyword and transforms the coordinates to epoch J2000 (FK5), in case they are in B1950 (FK4).

The code assumes a relatively simple geometrical shape without holes or chips. As the algorithm walks from the edges **into** the image, it cannot handle "inner structures", e.g. an annulus will be reduced to a circular footprint. Examples of calculated footprints are given in the mission descriptions (Sect. 1.4).

1.2.5 B1950–J2000 coordinate transformation

The Earth is a spinning top. As a result of the 26 000 year cycle precession and 18.6 year cycle nutation, Earth's equinox and therefore the apparent position of an astronomical object changes with time. Additionally, the proper motion of celestial objects results in changes of the position. Reasonably, the position of an object in its equatorial coordinate system (R.A./Dec.) should be as close as possible to the observed position. Therefore, the International Astronomical Union changed the reference frame from the old epoch and equinox B1950.0 Fundamental Catalog 4 (FK4) to the new epoch J2000.0 FK5 system in 1984 (Aoki et al., 1983; Fricke et al., 1988)[5].
Einstein, launched in 1978, and *EXOSAT*, launched in 1983, used the B1950 epoch (in FK4). Due to consistency reasons all footprints were computed in epoch J2000 (FK5). This means that one has to do a coordinate transformation to analyze the actual B1950 FK4 images with EUPPER. The ULS use the `astropy` (Astropy Collaboration et al., 2013) package to do this transformation before parsing the coordinates to EUPPER. As a result, the EUPPER input coordinates (in epoch B1950) look differently compared to the user's input (in epoch J2000).

1.2.6 Database implementation

The ULS use PostgreSQL[6] to handle the vast amount of image meta data (mostly footprint shapes). In order to determine whether the input coordinates match the footprint, pgSphere[7] is used. It provides a fast search of spherical coordinates in a SQL database. The ULS use SPOLY for the representation of polygons and SCIRCLE for circular footprints. The database has following fields:

- `OBSID`: The observation ID links the images to the catalog entries: If the observation ID is available in the catalog, its count rate value is adopted. Otherwise, EUPPER calculates an count rate upper limit from the image
- `FILENAME`: By using the file name the actual image can be found to parse its location to EUPPER
- `STC_S`: The footprint in FK5 J2000 right ascension and declination
- `FOV`: The polygon or circular information of the footprint in radians (for SPOLY/SCIRCLE)
- `FILT/INSTRUME`: If necessary, a filter or instrument column is appended, to apply the correct conversion factors (e.g. for *Einstein*)

[5] A fundamental catalog consists of a large number of instrumental catalogs in order to define a reference frame for the position and proper motion of celestial objects (Kovalevsky & Kenneth Seidelmann, 2004, p.261f). It depends on the epoch (a moment in time used as reference point) and the equinox of the Earth. The "B" before the epoch stands for Besselian year. Due to its variable length it was changed to the Julian year "J", which has exactly 365.25 days. The epoch J2000.0 equals 2000 January 1.5=JD 2451554.0 TDB (Kenneth Seidelmann, 1992, p.8)

[6] https://www.postgresql.org/

[7] https://pgsphere.github.io/

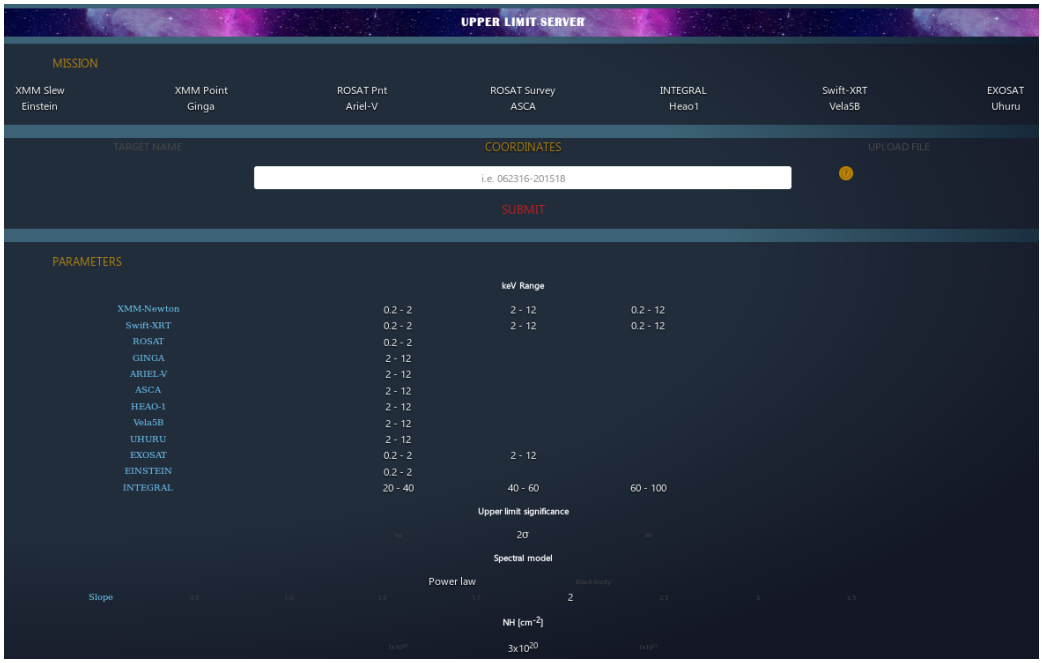

Figure 1.7: The HILIGT web interface.

1.3 Front-end

Currently, the ULS provide two clients in order to query the data. The first possibility is to use a script, which enables querying the data directly from the terminal and which may become useful to automatize queries.
On `xmmuls.esac.esa.int/upperlimitserver` one can find the web client of the ULS, called the **HI**gh-energy **LI**ghtcurve Genera**T**or (HILIGT). The interface consists of several panels: In the *Mission* panel one can choose which satellites should be queried. In order to search for data, one can give either the coordinates (in right ascension/declination, either sexagesimal, or decimal degree), or a target name (in SIMBAD convention[8]), or an input file list to query several sources. In the *Parameters* panel one can choose the output energy range, upper limit significance, spectral model, and absorption column. submitting the query starts the software. Waiting times are in the order of 30 seconds to one minute until a pop-up window opens, which contains the data. In the top panel (*Advanced Settings*) one can enable the displayed columns. Information about background and source counts, start and end date, exposure time, count rate, flux, encircled energy fraction and observation ID are available. Clicking on the download icon at the bottom ( ) will ask for the desired file format in order to download the data. Currently available data formats are ASCII, CSV or LaTeX. When clicking on the time-series icon ( ) one can choose the data columns to plot. Re-clicking this button invokes a plot displaying the lightcurve. The data can be plotted as scatter, line or spline plot and downloaded.

[8] `http://simbad.u-strasbg.fr/simbad/`

1.4 Description of the mission servers

Each mission has its own wrapper which is accessed by the web interface. In the following, I outline each mission server which I have set up.

1.4.1 *Vela 5B*

Vela 5B's instruments had an energy range of 3–750 keV, however, I concentrate on the scintillation X-ray detector (XC). This instrument was an all-sky monitor and had an energy range of 3–12 keV. The electric thresholds of the XC provided two energy channels: 3–12 keV and 6–12 keV. The detector had very high gain variation due to ∼60 °C temperature changes during its orbit. Information about this mission can be found in Whitlock et al. (1992). The VELA5B catalog contains data from the all-sky XC detector. I use only the 3–12 keV entries which were also corrected for the temperature change mentioned above. I implement the conversion factor $6.0 \pm 1.5 \times 10^{-12}\,\mathrm{erg\,cm^{-2}s^{-1}}$ given by Whitlock et al. (1992) and extrapolate the flux to 2–12 keV according to Eq. 1.8. I compute the error on the count rate, $(\mathrm{CR} \cdot \mathrm{exptime})^{0.5}/\mathrm{exptime}$, by assuming Poissonian error on the counts. Information about exposure time is not provided. Therefore, I set it to the difference between start and end date (typically in the order of years). *Vela 5B* had a very high background rate of $36\,\mathrm{cts\,sec^{-1}}$ which yields large background counts considering the long exposure time. I use a catalog search radius of 6°.

1.4.2 *Uhuru*

The Fourth Uhuru (4U) catalog UHURU4 consists of 339 sources with count rate and error information. I transform the count rate to a 2–6 keV flux using the conversion factor $1.7 \pm 0.34 \times 10^{-11}\,\mathrm{erg\,cm^{-2}s^{-1}}$, given by Forman et al. (1978). I extrapolate it further to the 2–12 keV band using Eq. 1.8. If the count rate error field is not populated, I set the error to zero. The resulting error on the flux will then solely originate from the conversion factor uncertainty (20%). Since there is no exposure, I use start date 1970-12-12 00:00:00 and end date 1973-03-18 00:00:00 with the difference as total exposure time. I set the background to zero (no information) and use a catalog search radius of 1°.

1.4.3 *Ariel V*

I focus on the catalog of the Sky Survey Instrument (SSI) which were two pairs of proportional counters (LE and HE system). One LE detector failed shortly after launch. Every spin period (6 s) *Ariel V* scanned a $20 \times 360\,\mathrm{deg^2}$ wide band on the sky at Galactic latitudes $|b| < 10°$. Information about the instrument is given in Whitlock et al. (1992) and about the catalog in Warwick et al. (1981) and McHardy et al. (1981). The ARIEL3A catalog contains 109 X-ray sources at low galactic latitudes ($|b| < 10°$) from the SSI instrument. I interpolate the 2–18 keV energy range to the *hard* band (2–12 keV). PIMMS does not include *Ariel V*. I therefore assume a constant count rate to flux conversion factor of $5.3 \pm 0.8 \times 10^{-11}\,\mathrm{erg\,cm^{-2}s^{-1}} = 1\,\mathrm{SSI\,cts\,sec^{-1}}$, as outlined in Warwick et al. (1981,

p.880). This conversion factor assumes a Crab-like spectrum, and has an uncertainty of 15%. Since the catalog does not provide information about start, end and exposure time, I set the start time to 1974-10-18 00:00:00, end time to 1980-03-19 00:00:00 and exposure time to the difference. Furthermore, I use a catalog search radius of 0.5°.

1.4.4 *HEAO-1*

The payload of *HEAO-1* consisted of four major instruments (A1–A4). I concentrate on the Cosmic X-ray experiment A2 which was divided into six proportional counters: two low energy detectors (LED, 0.15–3 keV), the medium energy detector (MED, 1.5–20 keV) and three high energy detectors (HED, 2.5–60 keV). Information is given in Rothschild et al. (1979) and Jahoda et al. (1994). I include the Piccinotti et al. (1982) catalog A2PIC which consists of 68 extra-galactic sources. The data origins from two six month long scans and is confined to galactic latitudes $|b| > 20°$, totaling 65.5% of the entire sky. PIMMS does not include the A2 mission on *HEAO-1*. Thus, I use the average conversion factor of $2.17 \pm 0.4 \times 10^{-11}\,\mathrm{erg\,cm^{-2}s^{-1}}$ in the 2–10 keV band, calculated by Piccinotti et al. (1982). I extrapolate this to the 2–12 keV *hard* band. The catalog provides two count rates (derived from a FOV of $1.5° \times 3°$) from the first and second scan, which I treat as two individual data points. Since no date is given in the catalog, I set the scan experiment starting date as observation date[9]. I use 1° as catalog search radius.

1.4.5 *Einstein* (HEAO-2)

A mission overview of *Einstein* is given by Giacconi et al. (1979) and the user manual can be found in D.E. Harris (1984). I concentrate on the Wolter Type I telescope with the Imaging Proportional Counter (IPC, Gorenstein et al. 1981; Harnden et al. 1984) and the High Resolution Imager (HRI, Henry et al. 1977). The data of both instruments is interpolated to the ULS *soft* band (0.2–2.0 keV).

High Resolution Imager (HRI)

The HRI was the first high-resolution X-ray camera on-board a spacecraft. It had a high spatial resolution of 3″ over the central 25′ focal plane and even 2″ within 5′ on-axis. Two catalog can be found on the HEASARC: HRIIMAGE and HRICFA. I merge the two catalogs by the sequence number to get the date of the observation, exposure time and count rate. The sequence number is further used as key to link the catalog entries to the images of the database. Since there is no information about the background in the catalogs, I set the background rate to `bkg_rate` $= 5 \times 10^{-3}\,\mathrm{cts\,sec^{-1}arcmin^{-2}}$ (Giacconi et al., 1979). I use an extraction radius of 3.98″ (HEW) for the computation of the background counts (D.E. Harris, 1984, Ch.4,p.10). The column `Net_Time`[10] in

[9] First scan: Start date = 1977-08-12 00:00:00, second scan: Start date = 1978-03-14 00:00:00, Exposure = time difference.

[10] `Net_Time` is the total number of seconds during which the detectors were able to gather data, corrected for Earth occultation, SAA, and detector dead time.

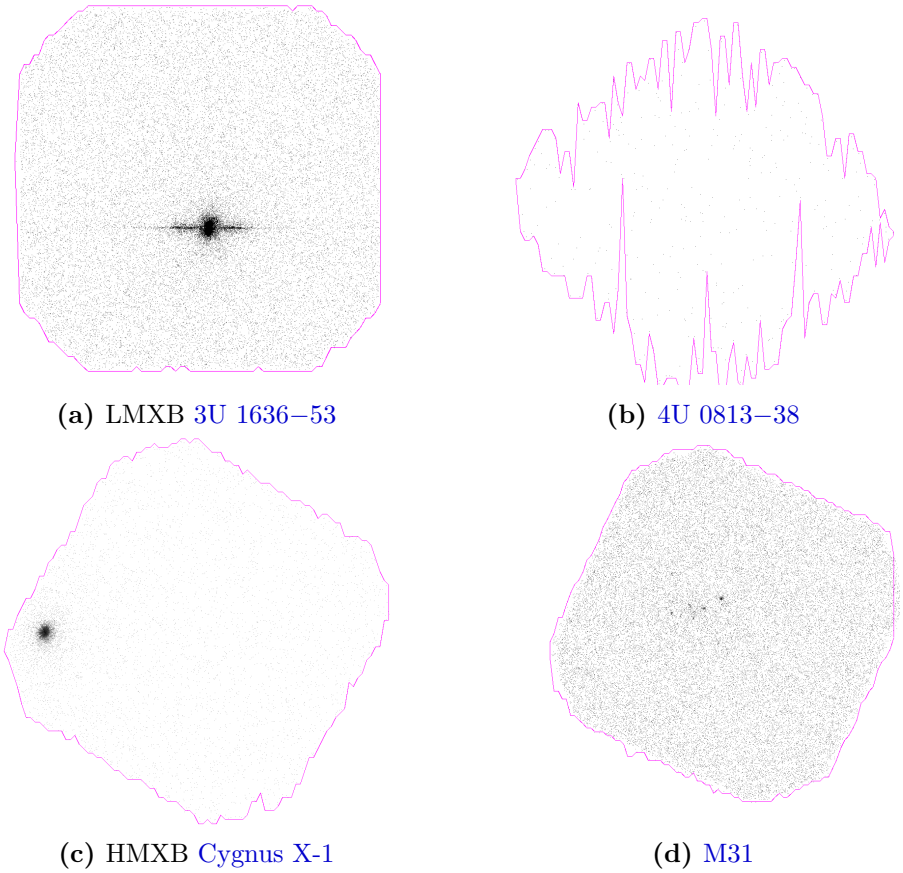

(a) LMXB 3U 1636−53 **(b)** 4U 0813−38

(c) HMXB Cygnus X-1 **(d)** M31

Figure 1.8: Example of the footprints calculated with my footprint finder for the *Einstein* HRI images. Colors are inverted.

HRIIMAGE is used as exposure time. Furthermore, I adopt the catalog search radii of $1'$ for HRICFA, and $15'$ for HRIIMAGE from the HEASARC.

There are 870 High Resolution Imager FITS files produced by the Harvard Center for Astrophysics. The images were taken with a $24'$ FOV in the range 0.15–3.5 keV. The footprints are calculated with my algorithm described in section 1.2.4. An example can be seen in Fig. 1.8. I encounter 22 images where the FITS file is unreadable. Some images exhibit very low count rates, making an exact border distinction difficult and resulting in frayed footprints (e.g. Fig. 1.8b). In total the database contains 836 footprints and images.

The PSF can be approximated by

$$PSF(r) \;=\; 2.885 \cdot 10^{-2} \cdot \exp\left(-\frac{r}{1.96''}\right) + 0.01 \cdot \exp\left(-\frac{r}{12.94''}\right) \text{arcsec}^{-2} \quad . \tag{1.9}$$

This approximation is accurate for a $5'$ circle around the field center (on-axis) at 1.5 keV and $r \leq 1'$ (D.E. Harris, 1984, Ch.4,p.10ff). I cannot find information about the off-axis

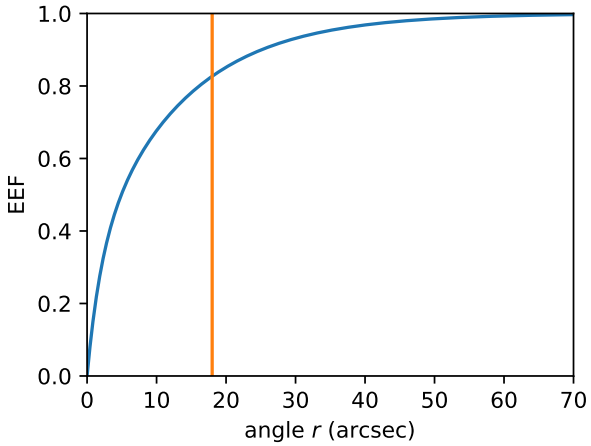

Figure 1.9: *Einstein* HRI encircled energy fraction. Orange line shows the 18″ source radius.

behavior of the PSF outside of 5′. I compute the encircle energy fraction (Fig. 1.9) by integrating the PSF to the given radius and dividing it by the full PSF (integrated up to 5′). The source radius is set to 18″ (*Einstein*'s "standard circle"), which corresponds to an EEF of 0.83 for this empirical model. Currently, no vignetting correction is implemented (no information found).

Imaging Proportional Counter (IPC)

The IPC had lower spatial (1 arcmin) and spectral resolution than the HRI but good efficiency and full focal plane coverage. Two identical IPC detectors (except for the entrance material) with an an energy range of 0.4–4.0 keV were mounted on *Einstein*. The background count rate was $\sim 10^{-2}$ cts sec^{-1} and the instruments sensitivity 1 cts sec^{-1} per 4×10^{-11} erg cm^{-2}s^{-1} (Giacconi et al., 1979).

There are two catalogs for the IPC containing 4132 FITS images in the 0.2–3.5 keV range: IPCIMAGE and IPC. I use catalog search radii of 2′ for the IPC catalog and 15′ for IPCIMAGE, respectively. To infer all necessary information, I merge these two catalogs by the sequence number in IPC and the object column in IPCIMAGE. I also use this sequence number as key to link the catalog entries to the images in the *Einstein* database. Following fields are queried from the IPCIMAGE catalog:

- `Object`: Same as sequence number in IPC (excluding the first letter); links the entries to the IPC catalog and to the images in the *Einstein* database
- `Live_Time`: Exposure time, equaling the keyword `TIME_LIV` in the images
- `Time` and `End_Time`: Start and end time of the observation

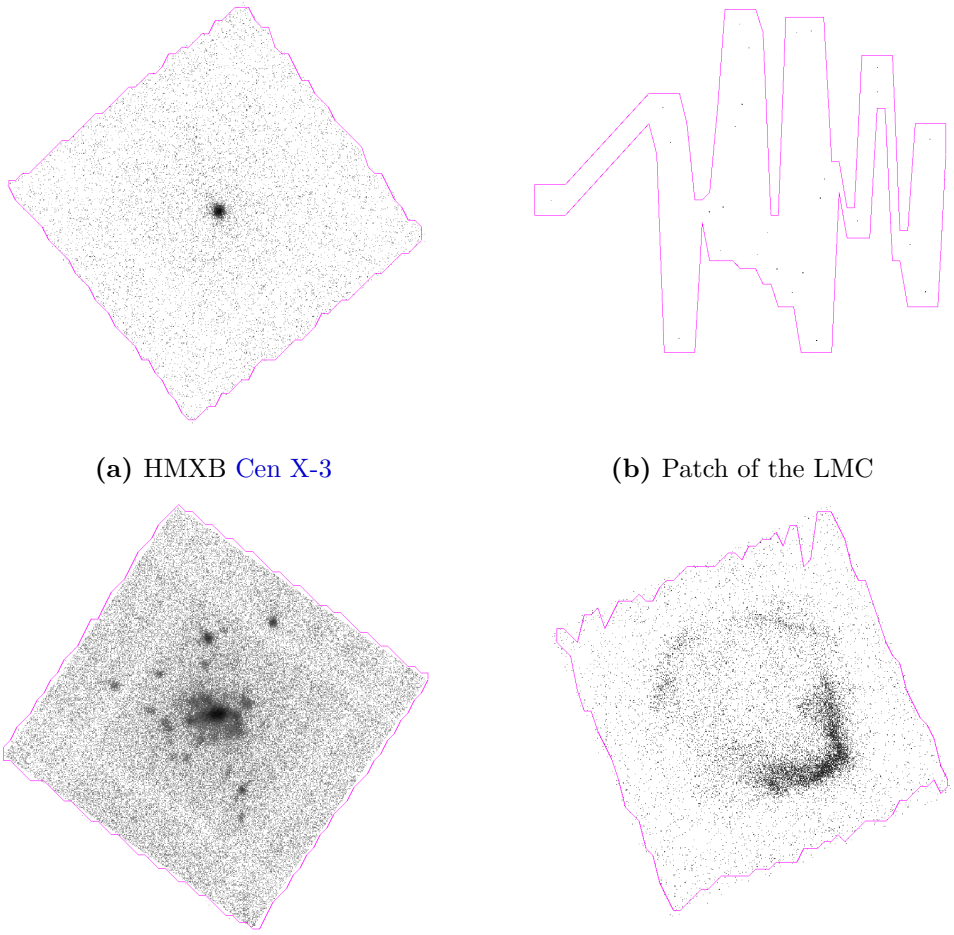

(a) HMXB Cen X-3

(b) Patch of the LMC

(c) M31

(d) SNR MSH 14−63

Figure 1.10: Example of *Einstein* IPC footprints with inverted colors. Note the extremely low count rate in (b). My footprint finder (Sect. 1.2.4) is not able to reconstruct the rectangular image shape based on only 27 counts.

The IPC catalog gives the source and background count rates of the observations (Harris, 1990):

- `Sequence_Num`: A two to five digit number which uniquely identifies an *Einstein* observation, and which I use as key to the IPCIMAGE entry
- `Count_Rate` and `Count_Rate_Error`: Corrected count rate in the 0.2–3.5 keV band
- `Background_Count`: The total number of background counts in the $2.4' \times 2.4'$ detection cell

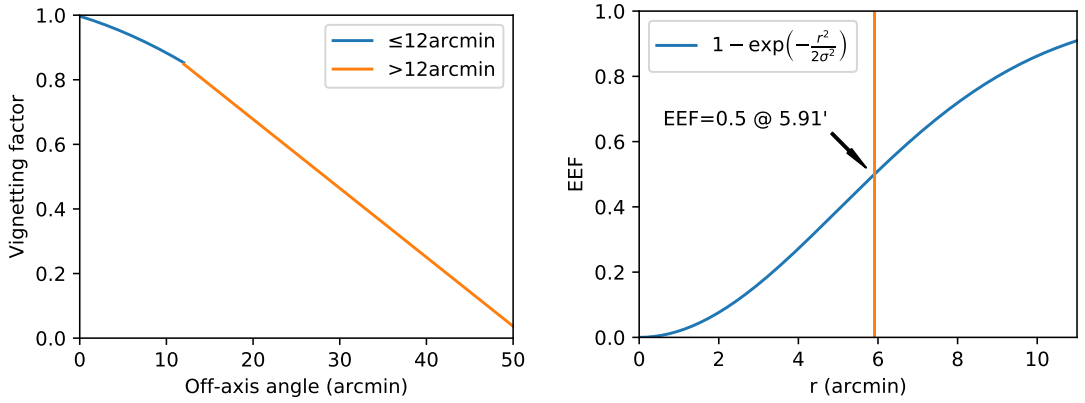

(a) **(b)**

Figure 1.11: (a) *Einstein* IPC vignetting function (Eq. 1.10–1.11). (b) *Einstein* IPC EEF function (Eq. 1.12) with $5.91'$ source radius.

The images available on the HEASARC have been smoothed with a $\sigma = 32''$ Gaussian and were background-subtracted. The resulting pixel unit of the images is counts arcmin^2 and not counts, as required by EUPPER. Additionally, negative count rates emerge due to the background subtraction. To bypass this problem, I use the raw event files and create images with the SAOImageDS9 software (Joye & Mandel, 2003, Beta version 8.0rc4). Finally, I use the algorithm described in Sect. 1.2.4 in order to calculate the *Einstein* IPC footprints. Examples can be found in Fig. 1.10. In total the *Einstein* database contains 3923 footprints with the corresponding images.

The formula for the vignetting (D.E. Harris, 1984, Ch.5, p.18) as a function of angle r (arcmin) of the IPC is

$$\mathrm{Vign}(r \leq 12') = (-0.0003125 \cdot r - 0.00825) \cdot r + 0.997 \tag{1.10}$$

$$\mathrm{Vign}(r > 12') = 1.1049 - 0.02136 \cdot r \quad . \tag{1.11}$$

The resulting vignetting function, as implemented into EUPPER, can be see in Fig. 1.11a.

Under the assumption of a circular Gaussian response with width σ, Harnden et al. (1984, p.24) give Eq. 1.12 for the fraction of total power enclosed within radius r (see Fig. 1.11b).

$$EEF(r) = 1 - \exp\left(-\frac{1}{2}\frac{r^2}{\sigma^2}\right) \tag{1.12}$$

The ULS use a source radius of $5.911'$ which equals an EEF of 0.5. This is a very large source radius, originating in the low spatial resolution (1 arcmin) of the IPC.

1.4.6 *EXOSAT*

The payload of *EXOSAT* consisted of two low energy imaging telescopes (LE, de Korte et al. 1981), a medium energy proportional counter (ME, Turner et al. 1981) and a gas scintillation proportional counter (Peacock et al., 1981). A full mission overview is given by White & Peacock (1988). The *EXOSAT* LE instrument is of great importance for the ULS software, since it produced 3677 images which provide the possibility of upper limit estimates. Additionally, I implemented the *EXOSAT* ME catalog access.

EXOSAT LE

The **L**ow **E**nergy setup consisted of two identical Wolter I telescopes with a focal length of 1.1 m. Each instrument had a *channel multiplier array* (CMA1 and CMA2, 0.05–2.0 keV) assembled in the focal plane. The CMA2 instrument failed on 1983 October 28, only five months into the three year lasting mission. Therefore, most images were detected by CMA1. The conversion factors interpolate the 0.05–2 keV band to the ULS *soft* band (0.2–2 keV).
The ULS access the HEASARC LE catalog with a catalog search radius of $1'$. The catalog gives the background in the field `background_per_sqpix` in units of cts pixel^{-2}. One pixel equals $4''$ and the on-axis HEW of the PSF is $24''$ (White & Peacock, 1988). Thus, I use a circular background region of area $\pi(12\,\mathrm{arcsec})^2$ and determine the background counts by `bkg_counts` = `background_per_sqpix` $\cdot\, \pi(12\,\mathrm{arcsec})^2/(4\,\mathrm{arcsec})^2$. The CMA detectors were sensitive to UV radiation. Bright O and B stars could contaminate the image quality. *EXOSAT* therefore used filters to determine the degree of contamination. From the nine filters on the filter wheel (FW), four are attendant to the *EXOSAT* LE images: Thick 400 nm Lexan (`4Lx` at FW Pos. 3), Aluminium-parylene (`Al/P` at FW Pos. 6), Thin 300 nm Lexan (`3Lx` at FW Pos. 7) and a Boron (`Bor` at FW Pos. 8) filter. Usually, `3Lx`, `Bor` and `Al/P` were used. To differentiate the different filters I add a filter field to each catalog entry which links the entry to the corresponding conversion factor. I download 3677 *EXOSAT* LE images from the HEASARC and identify four different image shapes in the data set: The images have a rectangular (∼8%) or octagonal (∼92%) shape, whereby the rectangular shape is smaller. Using this information, I classify the shapes by checking the area in an 80 pixel large box (using ftstat[11]) around the octagonal corner points. If the maximum value is zero, I can rule out the octagonal shape. The octagonal CMA1 and CMA2 images tend to have illuminated edges – likely due to stray light – with noise outside of the main shape. Some also exhibit extremely low count rates in the whole image. The latter makes an automatized footprint calculation with my footprint finder difficult. The footprint position on the detector plane, however, is constant for all octagonal images. Therefore, I define nine (eight for CMA2) fixed footprint points, specified in Table B.2. An example can be seen in Fig. 1.12a,b. The remaining rectangular images do not exhibit noise outside of the shape, which makes it ideally suited for my footprint algorithm (Fig. 1.12c,d). In total, the *EXOSAT* database contains 3677 footprints.

[11] `https://heasarc.gsfc.nasa.gov/ftools/caldb/help/ftstat.html`, see also Blackburn (1995)

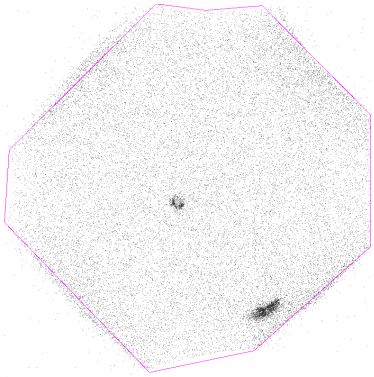

(a) CMA1 observation of SNR Cas A (∼81%).

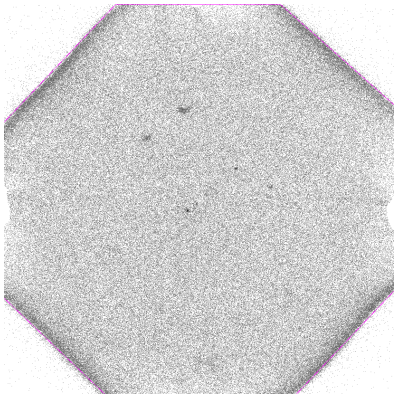

(b) CMA2 observation of HMXB Cyg X-3 (∼11%).

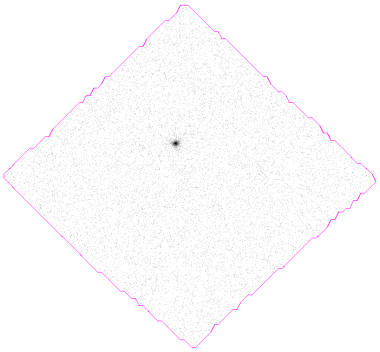

(c) CMA1 observation of the pulsar Her X-1.

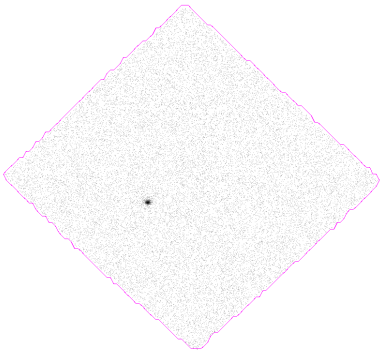

(d) CMA1 observation of the cataclysmic variable VV Pup.

Figure 1.12: An example of *EXOSAT* LE images with the calculated footprints. Fig. (a) shows the most abundant octagonal footprint shape with nine defined footprint points. In Fig. (b) one can see an example of the CMA2 octagonal footprint shape with eight defined points (see Table B.2). The illuminated edges are most likely stray light effects. Fig. (c–d) show the two remaining rectangular and smaller shapes, which were computed with the algorithm described in Sect. 1.2.4.

The observation ID is five letters long and occurs as `ORIGFILE` keyword in the FITS images. It is also contained in the filename (letter 5-9) and in the catalog as `File_Image` with an additional letter in front. Removing the letter allows generating the key in order to link the image to the corresponding catalog entry.

The point spread function of *EXOSAT* has 50% enclosed power (HEW) at 24″ (on-axis), degrading to 4′ at 1° off-axis. Vignetting effects of the telescopes reduced the off-axis effective area to 45% of its peak value at 1° off-axis (White & Peacock, 1988, p.11). In case the image is analyzed with EUPPER (i.e. no catalog entry), the ULS use a source radius of 1′.

EXOSAT ME

The **M**edium **E**nergy instrument consisted of an array of eight proportional counters. The instrument collected lightcurves in the energy range 1.3–15 keV (Argon filled-gas cell) and 5–55 keV (Xenon filled) which are interpolated to the ULS *hard* band (2–12 keV). More information can be found in Turner et al. (1981).
The ULS access the ME catalog for the pointed mission phase with a search radius of 45′. This catalog provides 2291 entries with start and end time, count rate, error, and exposure. The background is set to zero due to missing information. Furthermore, the EXMS catalog with 1210 entries from the slew phase is accessed with a search radius of 60′ (Reynolds et al., 1999). Next to count rate, error, and detection time, this catalog provides no processable information for the ULS.

1.4.7 *GINGA* (ASTRO-C)

GINGA had a very large energy range from 1–500 keV, however, only the Large Area Proportional Counter (LAC, 1.5–37 keV) matches the ULS bands. Information about *GINGA* can be found in Makino & ASTRO-C Team (1987) and Turner et al. (1989). The HEASARC does not provide images of *GINGA*. However, I include the catalog GINGALAC. The 1.5–37 keV range is interpolated to the *hard* band (2–12 keV) of the ULS. *GINGA* was in a low-earth orbit and regularly crossed Earth's radiation belts. A further background source is the diffuse cosmic X-ray background. The background subtraction can be found in Hayashida et al. (1989). Because the count rates of the catalog have already been background subtracted and there is no alternative background field, I set the background counts to zero. *GINGA*'s pointing stability was about 6′ (Turner et al., 1989). I therefore use a catalog search radius of 6′. The HEASARC uses 60′ which, however, might result in wrong identications with sources nearby.

1.4.8 *ASCA*

Four X-ray telescopes (Serlemitsos et al., 1995) with two detectors were assembled on *ASCA* (Tanaka et al., 1994): a Gas Imaging Spectrometer (GIS, 0.8–12 keV, Ohashi et al. 1996; Makishima et al. 1996) and a Solid-state Imaging Spectrometer (SIS, 0.4–12 keV, Gendreau 1995). Further information can be found in Tsusaka et al. (1995) and Arida (1998).

ASCA GIS

The GIS consisted of two imaging gas scintillation proportional counters with a circular FOV of 50′ and a spatial resolution of ∼0.5′ at 5.9 keV. A major problem for the upper limit calculation is the intrinsic PSF of the GIS detector. Usually, the PSF is only constrained by the optics, however, the GIS detector induces additional image distortion which is heavily dependent on off-axis angle. Modeling this PSF and extracting the EEF is not trivial and (for now) beyond the scope of the ULS. I therefore only include the catalog calls.

The *ASCA* Medium Sensitivity Survey (AMSS) is a serendipitous source survey for the extra-galactic sky $|b| > 10°$ and described by Ueda et al. (2001, 2005). The catalog lists a total of 2533 detected sources (5σ) from an area of 278 deg^2 in the bands 0.7–7 keV (*total*), 2–10 keV (*hard*) and 0.7–2 keV (*soft* band). The ASCAGIS catalog consists of two sub-catalogs: AMSS-I with 1343 sources detected between 1993 May and 1996 December and AMSS-II with 1190 sources detected between 1997 January and 2000 May. The catalog gives the count rate in the three bands mentioned above. I compute the count rate error (Ueda et al., 2001, p.13) as

$$\sigma_{\mathrm{CR}} = \frac{\mathrm{CR}}{\sigma_{\mathrm{D}}} \quad , \tag{1.13}$$

where CR is the count rate and σ_{D} the signal-to-noise ratio in units of sigma, given in column `SNR_Total/Hard/Soft` of the HEASARC catalog. The catalog does not provide any background and exposure information. I therefore set these values to zero and the total elapsed time, respectively. Furthermore, I use a catalog search radius of $3'$ for the *ASCA* GIS catalog cone search. This value is adopted from the HEASARC.

ASCA SIS

The Solid-state Imaging Spectrometer consisted of two cameras with 420×422 pixel^2 front-side illuminated CCD chips. It had an energy range of 0.4–10 keV and a FOV of $22' \times 22'$ with a spatial resolution of $30''$ (Gendreau, 1995). The ASCASIS catalog is populated with target and serendipitous sources in the SIS field of view. The catalog was published in Gotthelf & White (1997), resulting from a search for point-like sources in the public *ASCA* data archive. No background information is given in the catalog. I therefore set it to zero. The `Count_Rate` column in the catalog is in the 0.5–12 keV range, which is extrapolated to the *total* band (0.2–12 keV). I use a catalog search radius of $5'$ for the *ASCA* SIS catalog cone search.

1.4.9 *ROSAT*

A position sensitive proportional counter (PSPC) and an High Resolution Imager (HRI) were located in the focal plane (Pfeffermann et al., 1987) of *ROSAT*. A second telescope with a wide-field camera (Pounds et al., 1993), operating in the hard UV range (0.06–0.2 keV), is not included into the ULS. Due to its long operational period, large sky coverage and high exposure times, *ROSAT* is a very essential mission for the ULS. For a mission overview I refer also to the ROSAT User's Handbook by Briel et al. (1996).

Position Sensitive Proportional Counter (PSPC)

The PSPC consisted of multi-wire proportional counters and had modest energy and high spatial resolution ($25''$ at 1 keV) with a circular $2°$ diameter FOV. Two redundant units were assembled on a carousel: PSPC-B was used for the pointed phase while detector PSPC-C was used for the survey. Shadows of the wires in the detector could be suppressed

by dithering, however, shadows originating from the mirror mount ("spider") remain in the images (see Fig. 1.13). I use a source radius of 100″ for the PSPC instrument and interpolate its 0.1–2.5 keV to the ULS *soft* band (0.2–2 keV).

PSPC Pointed

The ULS access the ROSPSPC catalog by the HEASARC with a search radius of 30″. This catalog provides all relevant data. Furthermore, I download the images from the HEASARC and analyze the files ending on `im1`, which represent the total energy range 0.1–2.5 keV. Because EUPPER is mainly a tool to analyze point sources and because sources at large off-axis angles smear out due to the PSF, I choose a circle of radius 20.65′ as footprint around the center (FITS keywords `RA_NOM`, `DEC_NOM`). This represents the inner circle of the image without the spider diffraction spikes. Examples of the resulting footprint can be seen in Fig. 1.13. In total, the *ROSAT* database contains 5490 footprints.
The HEASARC provides exposure maps (ending `mex`) and background images (ending `bk1`). The exposure maps are included into the EUPPER calculation. The background maps are currently not included due to compatibility issues with the SAS[12].

I implement the radius and off-axis angle dependent encircled energy fraction according to Eq. B.11 in the appendix (Zimmermann et al., 1998). The 1 keV representation can be seen in Fig. 1.14. Note that the formula is energy dependent. This energy dependence is impossible to include into the ULS code because the information about photon energy is irretrievably lost in the image unless one has access to the corresponding event lists. Therefore, I assume[13] a constant energy of 1 keV.
I cannot get access to the tabulated values as outlined in Zimmermann et al. (1998, p.246). Therefore, I infer the vignetting correction factor from Fig. 1.15a. Due to the reasons outlined above, I only use the 1 keV values and obtain the vignetting correction factor as cross subsection through Fig. 1.15a at 1 keV. A read-off error of 2% is assumed. I interpolate the points below 20.65′ with a linear regression to determine radius dependent values. This yields the vignetting function 1.14 as function of off-axis angle ϵ (Fig. 1.15b). The fit produces unphysical vignetting values > 1 for off-axis angles $< 1.65'$. At these angles I set it to constant one.

$$Vig(\epsilon) = -0.0072 \cdot \epsilon + 1.012, \qquad \text{for } \epsilon < 20.65' \tag{1.14}$$

PSPC Survey

The Second *ROSAT* All-Sky Survey (RASS) Point Source Catalog (RASS2RXS) origins from the survey phase of the mission between 1990 June and 1991 August and contains over 135 000 sources at a likelihood threshold of 6.5 (Boller et al., 2016). The RASS is

[12] The pixel values are represented as 2-byte integers and rounded to zero by the *XMM-Newton* SAS
[13] This approximation has a large uncertainty of about 50% at low off-axis angles (Zimmermann et al., 1998, Fig. 5.17). The energy variation decreases at larger off-axis angles and is in the order of 5% at 30′ off-axis (Zimmermann et al., 1998, Fig. 5.18).

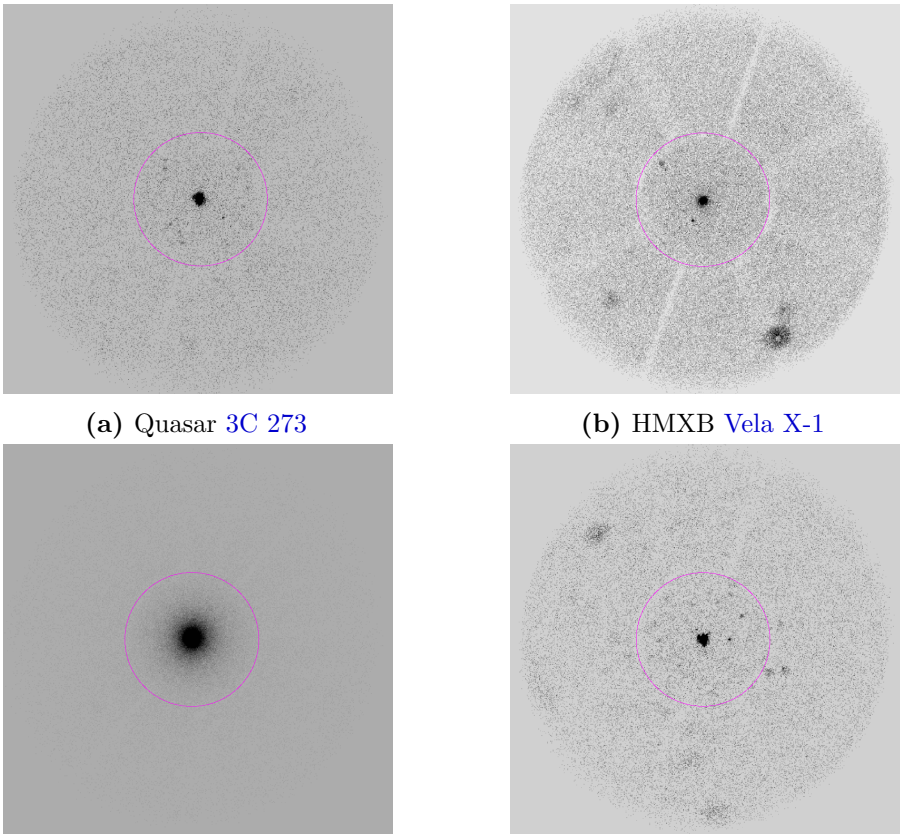

(a) Quasar 3C 273 **(b)** HMXB Vela X-1

(c) M1 (over-exposed) **(d)** Pulsar Her X-1

Figure 1.13: An example of *ROSAT* PSPC pointed images with the circular footprints and inverted colors. The purple circle has a radius of 20.65′. The radial spires are shadows of the so-called spider (the mount of the nested shells). Point sources become extended and smeared out at large off-axis angles due to the PSF.

still the most accurate and complete all-sky survey (before *eROSITA*). The ULS use a catalog search radius of 2′. Since the downloaded survey images are rectangular and represent the full FOV, the footprint is a simple rectangle. See Fig. 1.16 for two example images. The *ROSAT* PSPC survey database contains 1378 footprints.

High Resolution Imager

ROSAT's High Resolution Imager (HRI) was build up of two micro-channel plates with a crossed grid position readout system, similar to *Einstein*'s HRI. The field of view was $38' \times 38'$ with a spatial resolution of 1.7″ (FWHM). Information can be found in Pfeffermann et al. (1987), Briel et al. (1996), and Zimmermann et al. (1998).

The HEASARC ROSHRI catalog contains arcsecond positions and count rates for 56 401 detected sources from 5393 *ROSAT* HRI observations. In total, 1.94% of the sky

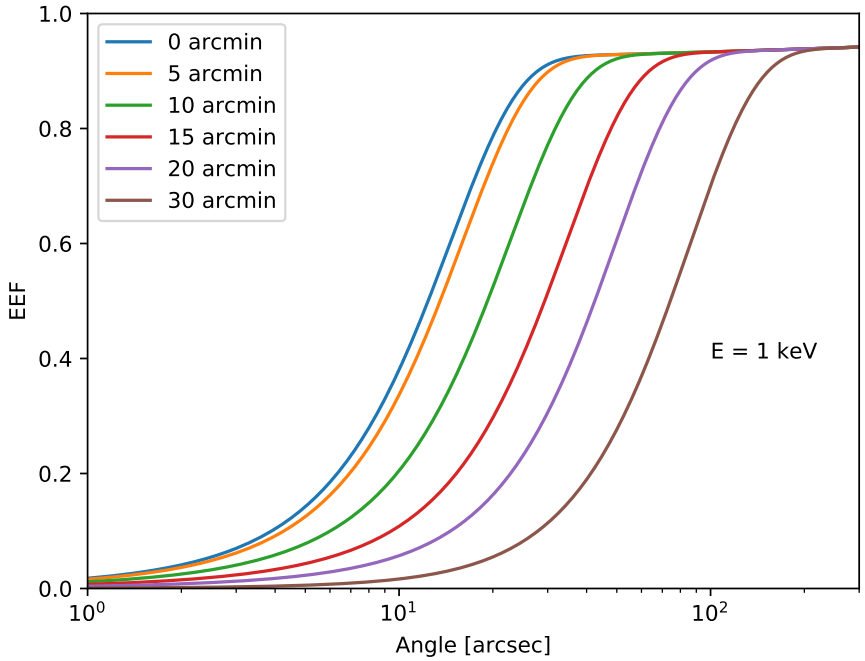

Figure 1.14: *ROSAT* PSPC cumulative point spread function (≡ EEF) as a function of angle with off-axis angle dependence at energy E=1 keV (Zimmermann et al., 1998, Eq. 5.13).

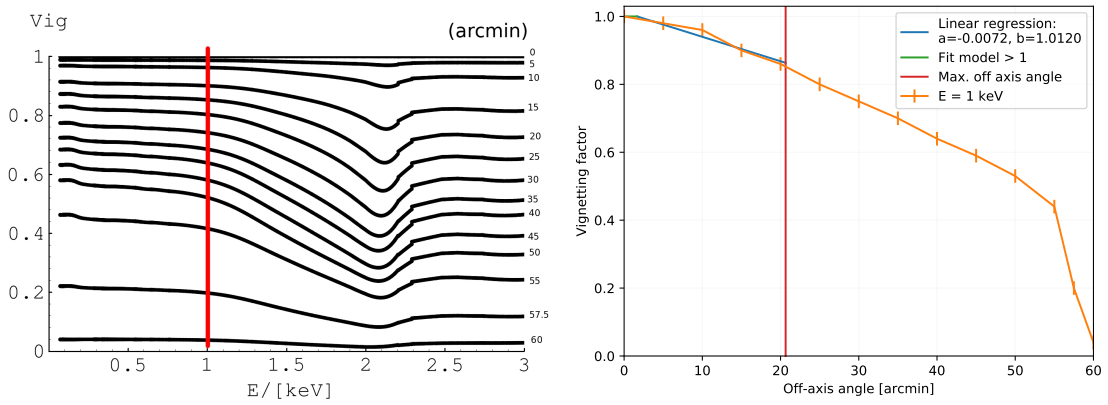

(a) **(b)**

Figure 1.15: *ROSAT* PSPC vignetting factor determination: (a) Vignetting as a function of energy for different off-axis angles modified from Zimmermann et al. (1998, Fig. 5.29). I deduce the radius dependent vignetting function as interpolation between the manually read-off points at 1 keV (red line). (b) Cross section through (a) yields vignetting function 1.14.

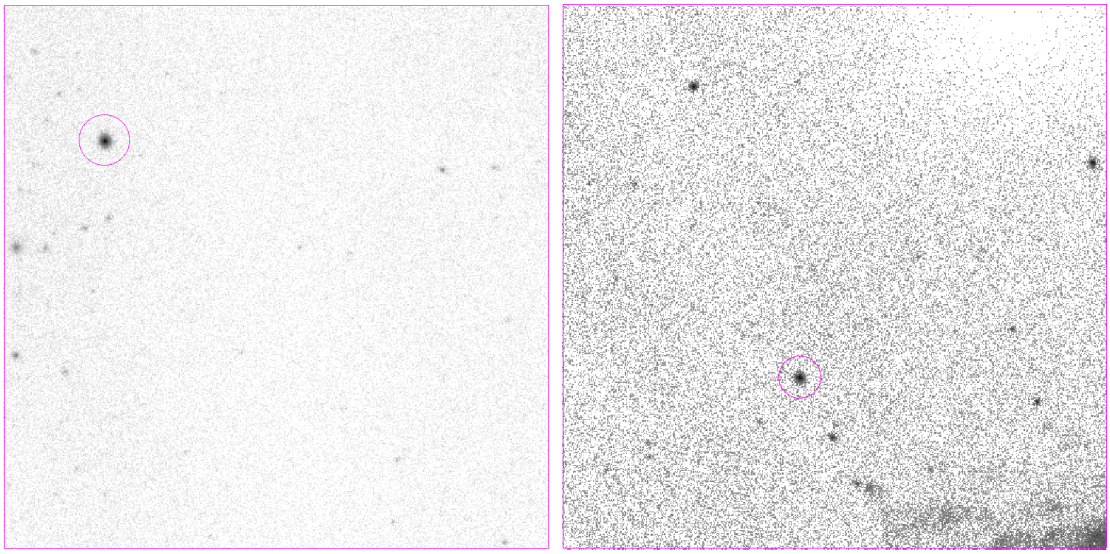

(a) LMXB Her X-1 **(b)** HMXB Vela X-1

Figure 1.16: An example of *ROSAT* PSPC survey images from the RASS catalog with rectangular footprints, target is within in the circle. Colors are inverted.

is covered with 13 452 high confidence detections. The catalog contains all necessary informations (including source and background counts) and is accessed with a search radius of 1′.
I download 5347 images from the HEASARC[14] and use the background images for the footprint extraction with my footprint finder. The background images are smoothed and exhibit a clear, distinct border. I exclude negative background regions occurring in some images from the footprint. An example footprint can be seen in Fig. 1.17. The data set exhibits 245 images with no counts (and therefore no reasonable use for the ULS), which I reject for the database. Overall, the *ROSAT* HRI database covers 5094 footprints. Furthermore, I include the background maps after changing the `CTYPE2` keyword from `DEC---TAN` to the FITS standard `DEC--TAN`. There are no *ROSAT* HRI exposure maps available on HEASARC. Therefore, the exposure is read off the `EXPOSURE` keyword in the image.

The encircled energy fraction is plotted in Fig. 1.18. The ULS use a source radius of 30″ for the upper limit calculation, which corresponds an EEF of 94%. As for *ROSAT* PSPC I fix the energy to 1 keV. This is a much better approximation (scattering $< 10\%$) compared to the PSPC instrument (Zimmermann et al., 1998, Fig. 5.23–24). Tabulated vignetting correction factors should be available as outlined in Zimmermann et al. (1998, p.246). However, I could not get access to this file.

[14] `ftp://heasarc.gsfc.nasa.gov/FTP/rosat/data/hri/processed_data/`, ending on `im1.fits`

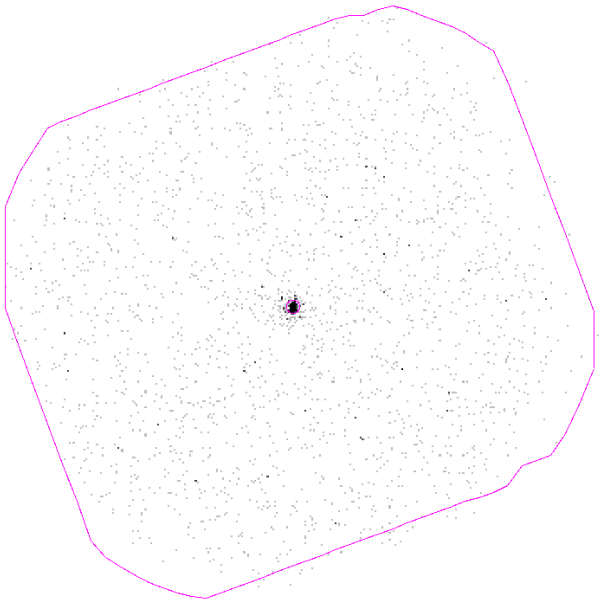

Figure 1.17: *ROSAT* HRI image of the quasar 3C 273 with inverted colors. The footprint is calculated from the background image. The small circle displays the sources radius of 30″.

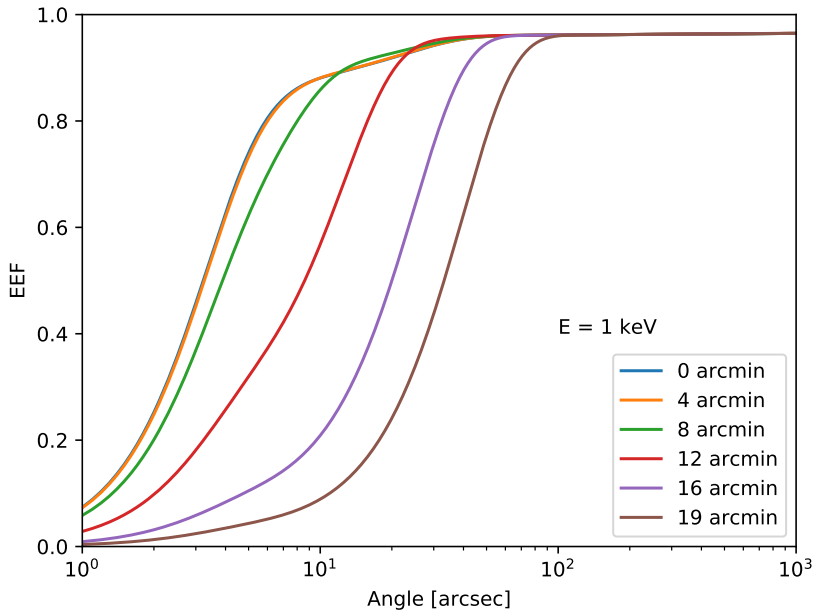

Figure 1.18: *ROSAT* HRI cumulative point spread function (≡ EEF) as a function of angle for various off-axis angles and fixed energy E=1 keV (Zimmermann et al., 1998, Eq. 5.19).

Table 1.1: Overview of parameters for each mission; energy range given in keV

Mission	Energy range	FOV	Spatial res. [″]	Source rad	Cat. name	Cat. search rad. [′]	Background	Filters/Instr	References	Notes
Vela 5B	2–12	6.1° × 6.1°		–	VELA5B	360	$36\,\mathrm{cts\,sec^{-1}} \cdot$ `exptime`	XC	176	No images
Uhuru	2–12	0.52° × 0.52° 5.2° × 5.2°		–	UHURU4	60	N/A		Cat.: 57; 46	No images, exptime missing
Ariel V	2–12	0.75° × 10.6°		–	ARIEL3A	30	N/A	SSI	Instr.: 176 Cat.: 173; 110	No images, exptime missing, $\lvert b\rvert < 10°$
HEAO-1	2–12	1.5° × 3°		–	A2PIC	60	N/A	A2	Instr.: 144 Cat.: 131	No images, $\lvert b\rvert > 20°$
Einstein IPC	0.2–2	75′ × 75′	60	5.911′ @ 0.5 EEF	IPC IPCIMAGE	2 15	from cat. –		Instr.: 55; 61; 66 Cat.: 58; 67	B1950→J2000 transf., 3923 images
Einstein HRI	0.2–2	25′ diam.	3	18″ @ 0.8 EEF	HRICFA HRIIMAGE	1 15	$0.005\frac{\mathrm{cts}}{\mathrm{arcmin^2 s}}$ with 3.98′ extr. rad.		Instr.: 55; 73; 34	B1950→J2000 transf., 836 images
EXOSAT LE	0.2–2	2°	18″	1′	LE	1	`bkg_per_sqpix` $\cdot 9\pi$	3Lx, 4Lx, Al/P, Bor	Instr.: 35; 175	B1950→J2000 transf., 3677 images
EXOSAT ME Pointed	2–12	45′ × 45′	–	–	ME	45	N/A		Instr.: 35; 166; 175	No images
EXOSAT ME Slew					EXMS	60			Cat.: 142	No images
GINGA LAC	2–12	0.8° × 1.7°		–	GINGALAC	10	N/A		Instr.: 104; 167; 70	No images
ASCA GIS	0.2–2 2–12 0.2–12	50′	0.5′ @ 5.9 keV	(5′)	ASCAGIS	3	N/A		Instr.: 159; 124; 152; 106 164; 6 Cat.: 169; 170	No images Add. intrinsic PSF by GIS exptime missing
ASCA SIS	0.2–12	22′ × 22′	30″	(3.3′ @ 0.5 EEF)	ASCASIS	5	N/A		Instr.: 159; 52; 152; 164 Cat.: 62	No images
ROSAT PSPC Pointed	0.2–2	2° circ.		100″	ROSPSPC	0.5	from cat.	None	Instr.: 161; 130; 9; 184; 25	5490 images
ROSAT PSPC Survey					RASS2RXS	2	from cat.	Open	Instr.: 161; 130; 9; 184; 25 Cat.: 24	1378 images
ROSAT HRI Pointed		38′ square	2″ FWHM	30″ @ 0.94 EEF	ROSHRI	1	from cat.		Instr.: 161; 130; 9; 184; 25	5094 images

References: 6:Arida (1998), 9:Aschenbach (1988), 24:Boller et al. (2016) 25:Briel et al. (1996), 34:D.E. Harris (1984), 35:de Korte et al. (1981), 46:Forman et al. (1978), 52:Gendreau (1995), 55:Giacconi et al. (1979), 57:Giacconi et al. (1971), 58:Gioia et al. (1990), 61:Gorenstein et al. (1981), 62:Gotthelf & White (1997), 66:Harnden et al. (1984), 67:Harris (1990), 70:Hayashida et al. (1989), 73:Henry et al. (1977), 104:Makino & ASTRO-C Team (1987), 106:Makishima et al. (1996), 110:McHardy et al. (1981), 124:Ohashi et al. (1996), 130:Pfeffermann et al. (1987), 131:Piccinotti et al. (1982), 142:Reynolds et al. (1999), 144:Rothschild et al. (1979), 152:Serlemitsos et al. (1995), 159:Tanaka et al. (1994), 161:Trümper (1982), 164:Tsusaka et al. (1995), 166:Turner et al. (1981), 167:Turner et al. (1989), 169:Ueda et al. (2001), 170:Ueda et al. (2005), 173:Warwick et al. (1981), 175:White & Peacock (1988), 176:Whitlock et al. (1992), 184:Zimmermann et al. (1998)

1.5 Scientific Application

The main purpose of the *Upper Limit Servers* is to provide an overview of the existing data in the form of a long-term lightcurve. The archived catalog data, in combination with upper limits, at essentially any celestial position gives the genuine opportunity to detect interesting patterns in the lightcurves. It may serve as inspiration for proposals and more sophisticated scientific analyses. Active Galactic Nuclei, for instance, often exhibit variability patterns which range over decades. Due to the limited lifetime of satellites, a single X-ray mission is thus not able to detect these patterns and only inter-mission lightcurves reveal them. Also transient sources like X-ray binaries can show repeated outbursts, which may not be covered by only one instrument. Now, with *eROSITA* launched, and in the advent of numerous new source discoveries, the upper limit calculations can provide helpful constrains on the past behavior of transients. Furthermore, the ULS may help classifying new celestial objects. Lightcurves of supernovas remnants, for instance, look fundamentally different than lightcurves of transient X-ray binaries or tidal disruption events. The lightcurves generally gives valuable information about the source type.

Obviously, lightcurves do not replace spectral analyses. The current model choices (power-law and black body) of the ULS are limited, and usually the spectral shape of the source has to be approximated. The lightcurves do, however, give a quantitative impression of the variability and outburst behavior of the sources. In the following section lightcurves of three astrophysical sources are shown.

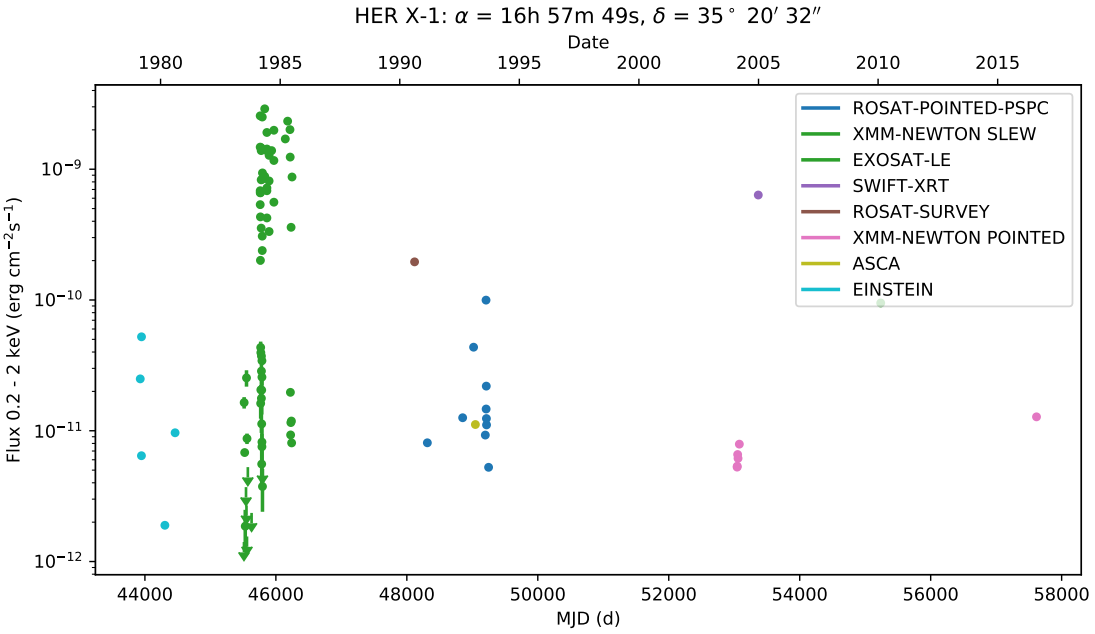

Figure 1.19: Lightcurve of the LMXB Her X-1.

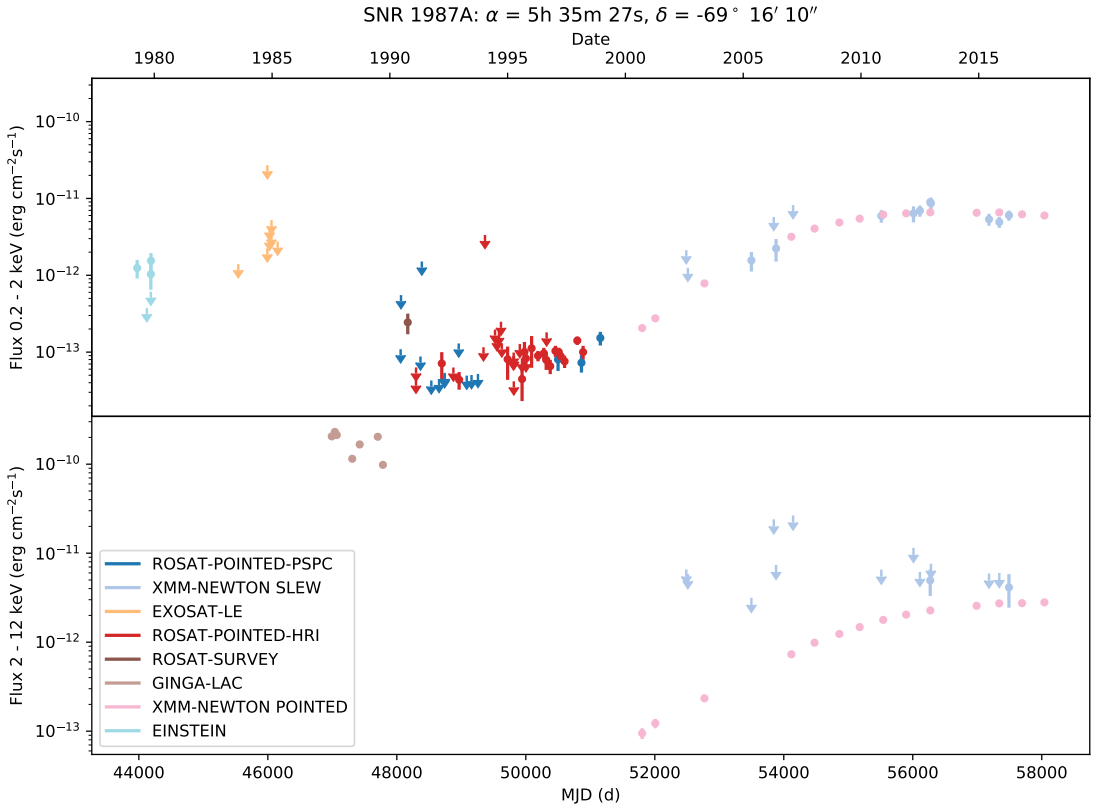

Figure 1.20: Lightcurve of the SNR 1987A.

The low-mass X-ray binary Her X-1 is likely the best observed accreting pulsar. The spectral shape is approximated as power-law with $\Gamma = 1.0$ and $N_{\mathrm{H}} = 3 \times 10^{20}\,\mathrm{cm}^{-2}$.[15] Figure 1.19 shows a strong outburst in the 1984 *EXOSAT* data. This observation gave evidence of a 35 day accretion disk precession cycle (Trümper et al., 1986).

In Fig. 1.20, one can see the lightcurve of the supernova remnant SNR 1987A in the Large Magellanic Cloud. Supernova remnants have softer spectra than LMXBs or AGN and typically more advanced models (e.g. APEC) than a power-law are necessary to describe the spectral shape. This functionality is, however, currently not included in the ULS. Therefore, I approximate the spectral shape as power-law with the maximal photon index of 3.5 and absorption of $1 \times 10^{21}\,\mathrm{cm}^{-2}$.[16] The large flux increase observed with *GINGA* in 1987–1989 is due to the supernova explosion. This is followed by an X-ray flux decrease until the ejecta reach the interstellar medium where it produces X-rays from shocks. Since then the flux increases again (see e.g. Maggi et al., 2012).

[15] Fürst et al. 2013 find $\Gamma \approx 0.9$, $N_{\mathrm{H}} \approx 1.7 \times 10^{20}\,\mathrm{cm}^{-2}$ with `highecut`

[16] Heng et al. 2008 find $N_{\mathrm{H,Gal.}} = 6 \times 10^{20}\,\mathrm{cm}^{-2}$, $N_{\mathrm{H,LMC}} \approx (2\text{–}3) \times 10^{21}\,\mathrm{cm}^{-2}$

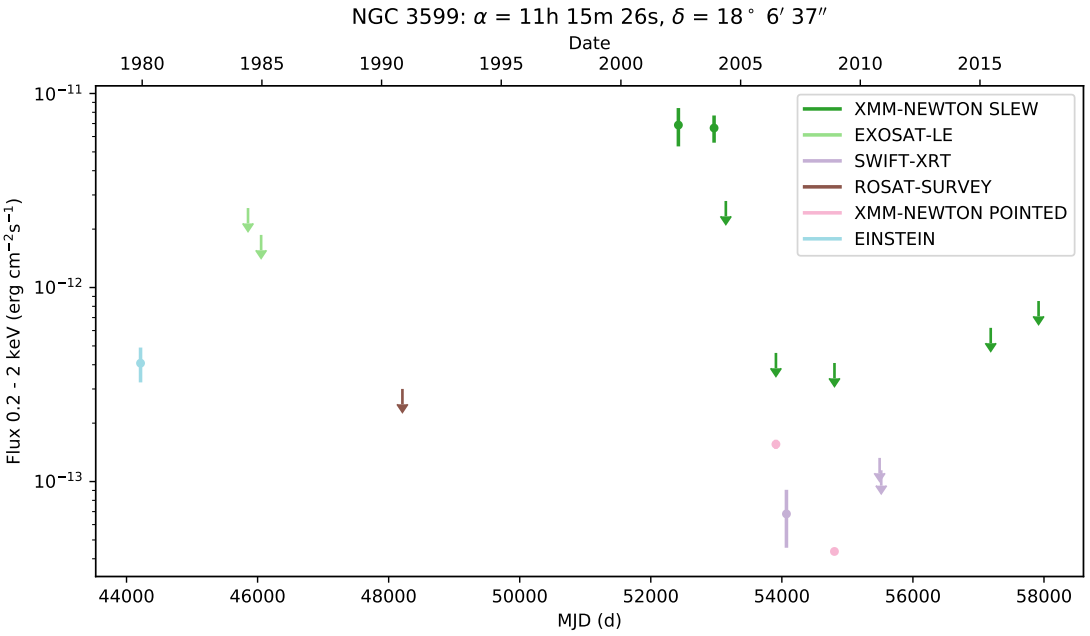

Figure 1.21: Lightcurve of the AGN NGC 3599.

Finally, one sees the lightcurve of the AGN NGC 3599 in Fig. 1.21. A power-law of spectral index 2.0 and Galactic absorption ($3 \times 10^{20}\,\mathrm{cm}^{-2}$) is assumed. This lightcurves shows the utility of upper limits, where the *ROSAT* and *XMM-Newton* Slew upper limits constrain the flux to low values right before and after the big outburst. This strong outburst could be an accretion disk instability or a delayed tidal disruption event as reported in Saxton et al. (2015).

Part II

Data analysis of GRO J1744−28

Chapter 2

Theory of X-ray binaries

2.1 X-ray binaries

2.1.1 Neutron stars

Neutron stars (NSs) are compact objects which form during core-collapse supernovae. A theoretical description goes back to Baade & Zwicky (1934), in fact this is only two years after the discovery of the neutron itself (Chadwick, 1932). Over 30 years later Hewish et al. (1968) experimentally confirmed neutron stars by detecting repeated ratio pulsations.

Neutron stars form at the end of a massive star's life time, when it depleted all of its fuel. The star's radiation pressure cannot withstand the gravitational attraction any more and the core collapses. The pressure becomes high enough that electron and protons fuse and form neutrons (inverse β-decay, see Pacini, 1967). This ejects a neutrino flash, radiating away the outer shells of the star into the interstellar medium. The core-collapse is halted by neutron degeneracy pressure which restores equilibrium. A neutron star is formed. Typical parameters are radii of $\sim$10 km, masses of 1–2 $M_\odot$, and extreme densities, comparable to atomic nuclei (e.g. Bhattacharya & van den Heuvel, 1991; Lattimer, 2012; Steiner et al., 2013).

Because the original star rotates and shrinks to a fraction of its radius – while conserving angular momentum – neutron stars can spin with periods on the sub-second scale. An extreme example is PSR J1748−2446ad which spins with 714 Hz, resulting in surface speeds in the order of $\frac{1}{4}$c which is close to the break-up speed of the NS (Hessels et al., 2006). The radio pulsations observed by Hewish et al. (1968) can be explained by the fact that the magnetic poles are not aligned with the rotation axis. The emission from the poles induce a "lighthouse" beam which passes over the Earth in every rotation (Gold, 1968). The strong gravitational field curves the space time around the neutron star. The resulting red-shift of escaping light rays is described in the framework of general relativity (Einstein, 1916). Furthermore, neutron stars exhibit extremely strong magnetic fields in the order of 10^8–10^{14} G, making them the most powerful dynamos in the universe.

2.1.2 Low-mass X-ray binaries

Neutron stars can appear in a wide range of the electromagnetic spectrum – from radio pulsations to γ-ray emissions – and can display themselves very differently (Harding, 2013). Here, I will concentrate on the class of low-mass X-ray binaries (LMXBs) with a neutron star as compact object. This is also the system encountered in the data analysis of Ch. 3.

LMXBs consist of a compact object and a less-massive, Roche-lobe filling donor star. These systems accumulate on the Galactic plane, indicating that they are located within our Milky Way at typical distances of around 8.5 kpc. However, some LMXBs have also been seen in globular clusters, which suggests that these systems are relatively old. Strong X-ray emission is observed which yields a spherical luminosity in the order of 10^{34}–$10^{38}\,\mathrm{erg\,s^{-1}}$. This is about 2.5–2.5 $\times$ 10^4 times the energy output of the Sun, but only concentrated on the X-ray part of the spectrum (Zwicky, 1939; Bhattacharya & van den Heuvel, 1991). The compact object is formed in a supernova and can be either a neutron star (NS), or a black hole.

The late-type companion star and NS orbit around the center of mass. In LMXBs, the NS and companion star are so close that the orbit is approximately circular. Mass transfer occurs because the expanded companion star fills its Roche-lobe. Thus, matter can be continuously transferred to the NS and forms an accretion disk due to conservation of angular momentum. Hawley et al. (1995) found magneto-rotational instabilities (MRIs) to be responsible for the turbulence and angular momentum transport in accretion disks. They visualize this process by springs between particles on two separate orbits. The "spring" drags the matter on outer orbits forward and slows down the particles on inner radii. The resulting (magnetic) torque leads to a loss of angular momentum of the inner particle, moving it onto an orbit closer to the NS, while the outer particle moves outwards. As the matter propagates inwards it becomes exceedingly more turbulent and heats up to temperatures of 10^6–10^9 K due to friction. At such temperatures the matter is highly ionized and forms a plasma. The strong gravitation accelerates the particles up to 0.7 c before the particles are stopped close to the NS surface. This releases enormous amounts of energy as Bremsstrahlung and black body radiation in the soft X-ray regime. LMXBs have typical magnetic fields in the order of 10^8–10^9 G. Often, this is not strong enough to force the plasma onto the NS poles but it disposes on the equator. See Sect. 2.1.4 for a description how the hard X-ray radiation is produced.

2.1.3 Outbursts and bursts

In the context of X-ray binaries, outbursts are defined as large flux increases ("on-state") with respect to the normal flux level ("off-state/quiescence state"). Because matter overflow is continuous in LMXBs, outbursts can have durations of months (compared to HMXBs which transfer mass typically only in periastron passages, and where outbursts usually last shorter times). Whether the source goes into an outburst highly depends on the properties of the neutron star. If, for instance, the magnetic field pressure exceeds the ram pressure, the propeller effect sets on and mass is prevented from falling onto

the NS (e.g. Cui, 1997). Other effects like rotation and mass of the NS can have further effects on the outburst behavior.

If a source is always detectable, it is called *persistent* (e.g. 3A 0114+650, see Grundstrom et al. 2007; Vela X-1, see Kreykenbohm et al. 2008; Her X-1, see Katz 1973 and lightcurve in Fig. 1.19). Note that this does not mean that the source does not exhibit outbursts. On the contrary – if the source is only visible in its outbursts – it is called *transient* (e.g. 4U 0115+634, see Müller et al. 2013; V 0332+53, see Stella et al. 1985). Some transient sources exhibit outbursts in a regular and periodic way (e.g. GRO J1008−57, see Kuehnel et al. 2012; EXO 2030+375, see Wilson et al. 2008) whereas others are highly irregular and are entirely "off" and non-detectable at times (e.g. GRO J1744−28, see analysis in Ch. 3 and lightcurve in Fig. 3.1; Swift J1626.6−5156, see Reig et al. 2008). As soon as a space-based monitoring instrument (e.g. *Swift*-BAT or MAXI) detects a significant flux increase, other instruments (like *Chandra*, *XMM-Newton*, *INTEGRAL* or *NuSTAR*) may observe the source to obtain detailed spectra.

Some low B-field accreting neutron stars are seen to exhibit short spikes in their lightcurves. These rapid luminosity changes are in the order of seconds, followed by an exponential decay (fast raise, exponential decay – FRED) and are referred to as X-ray bursts. They were first observed by Belian et al. (1972) in Cen X-4 (see also Kuulkers et al., 2009). Type I bursts are due to a thermonuclear explosion on the neutron star surface (Grindlay et al., 1976; Lewin & Joss, 1983). Burst sources typically exhibit a relatively small magnetic field $< 10^{11}$ G such that matter is not funneled onto the poles but disposes on the NS equator. Hydrogen accumulates on the whole surface until thermonuclear fusion is induced. The localized explosion quickly expands around the neutron star surface: The atmosphere "explodes". For observers, this is visible as short flare in the lightcurve. Type II bursts are likely due to spasmodic accretion of matter and thus a gravitationally induces effect of accretion. Only a few sources have been observed showing Type II bursts in their lightcurve (e.g. the Rapid Burster in Lewin et al., 1993) and the exact formation procedure remains yet to be solved.
Burst sources typically do not exhibit pulsations. A peculiar exception is GRO J1744−28, also known as the "Bursting Pulsar", which is a LMXB with relatively high magnetic field, displaying X-ray bursts and pulsations (see Sect. 3.1, Kouveliotou et al. 1996; Younes et al. 2015).

2.1.4 Cyclotron resonant scattering features

Cyclotron resonant scattering features (CRSFs) or "cyclotron lines" are absorption line-like features visible in the X-ray band and mostly observed in high-mass X-ray binaries with large magnetic fields $> 10^{12}$ G. They were discovered by Trümper et al. (1978) in the persistent X-ray binary Her X-1. A prime example is 4U 0115+634 where the fundamental cyclotron line and four higher harmonics were detected (Santangelo et al., 1999; Heindl et al., 2004). A comprehensive review of CRSF sources and their observation was recently presented by Staubert et al. (2019) as well as Schwarm et al. (2017a,b) describing their theoretical modeling.

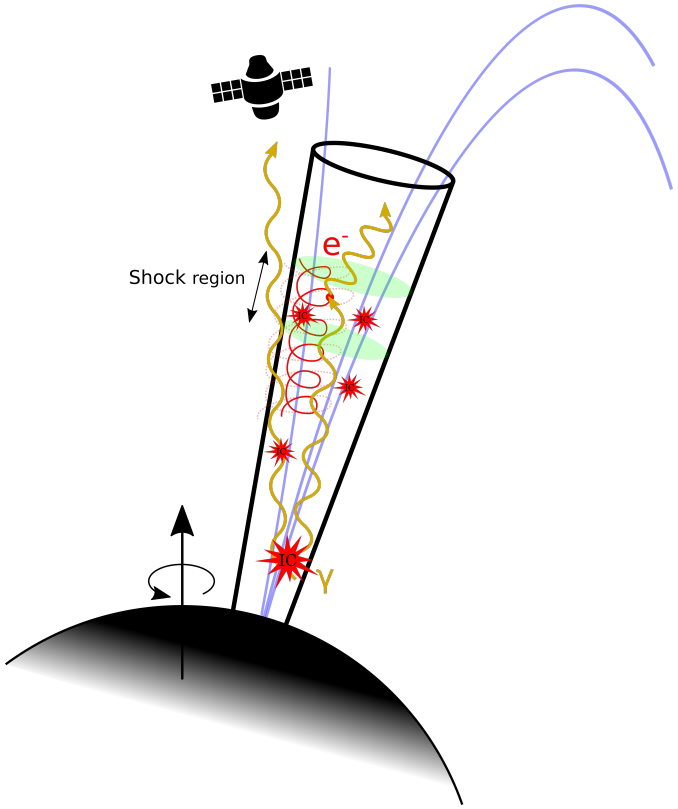

Figure 2.1: A scheme illustrating the accretion mechanism and CRSF formation in sub-critical regime as modeled in Becker et al. (2012). Blue lines sketch the magnetic field which guides the plasma onto the neutron star poles. Rotational axis and magnetic poles are misaligned which causes pulsations. The satellite icon represents Earth's line-of-sight. Green patches confine the radiation-dominated shock region which is likely also the cyclotron line forming region in this regime. Red spirals indicate that the electron spirals around the B-field lines on quantized orbits. Inverse Comptonization occurs in the whole accretion column.

When ionized matter approaches the Alfvén radius, it couples to the B-field lines of the NS. The accreted plasma is guided towards the NS pole and is thought to form a cone-like accretion column which is likely the origin of the continuum radiation. In the presence of strong magnetic fields, the motion of charged particles is quantized perpendicular to the magnetic field onto discrete Landau levels (Landau & Lifshitz, 1965; Langer, 1981). One can think of the electrons in-spiraling around the B-field lines on quantized "orbits". When the plasma is stopped in the shock region, the hot ($T \sim 10^8$ K) plasma emits thermal black-body radiation in the soft X-ray band. These seed photons gain energy by scattering off hot plasma electrons (thermal Comptonization). Additionally, the photons scatter off the fast (up to 0.7 c) matter flow (bulk motion Comptonization). Because the photons **gain** energy the process is also called **inverse** Compton scattering.

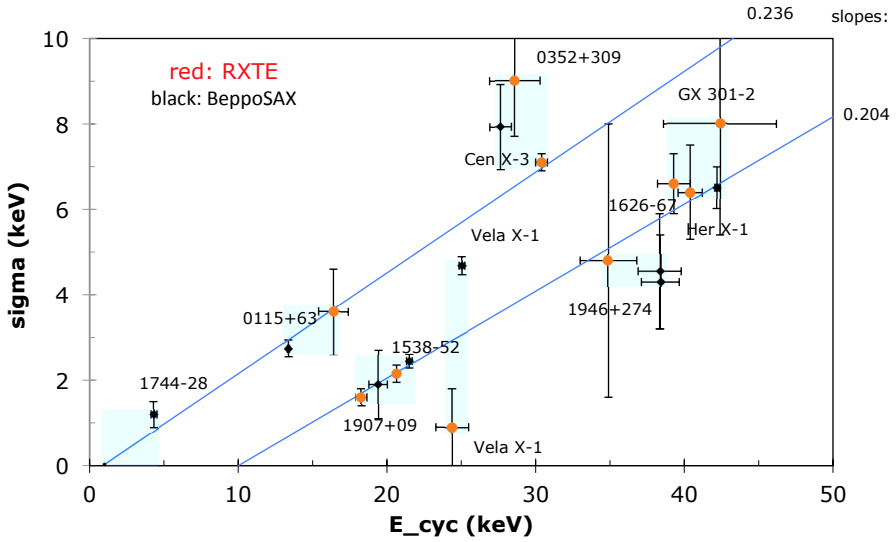

Figure 2.2: CRSF correlation between width σ and centroid energy E_c (Staubert et al., 2019, Fig. 12).

This inverse Compton scattering is responsible for the hard X-ray radiation in the continuum. At the spacing energies of the Landau levels, however, it becomes a resonant process and the cross-section strongly increases. The transition of the electrons between different Landau levels gives rise to absorption line-like features in the spectrum which are referred to as CRSFs. If the electron is excited by one level the fundamental cyclotron line emerges. When an electron gets excited to higher levels, one speaks of higher harmonics. Note that the literature is not consistent whether the next-higher line after the fundamental is called *first* or *second* harmonic. Cyclotron lines are very broad which makes them sometimes difficult to detect. A correlation of CRSF width and centroid energy can be found in Fig. 2.2.

The most powerful diagnostic capability of CRSFs is their linear proportionality to the B-field strength. This is the most useful method to estimate the magnetic field of a neutron star (Ghosh & Lamb 1979a,b give an alternative approach based on accretion torques). The energy spacing between the Landau levels can be calculated according to

$$E_c = \frac{\hbar e B}{m_e c} \approx 11.6\,\mathrm{keV} \cdot B_{12} \quad , \text{with } B_{12} = \frac{B}{10^{12}\,\mathrm{G}} \tag{2.1}$$

Including the red shift $1+z \sim 1.2$–1.4 this leads to the so-called 12-B-12 rule which gives the magnetic field strength in the line-forming region:

$$B_{12} = (1+z)\frac{E_c}{11.6\,\mathrm{keV}} \tag{2.2}$$

Most lines have been observed in the range $> 25\,\mathrm{keV}$ and are generally not detected in the low B-field LMXBs. Few examples are CRSFs in Her X-1 (Trümper et al., 1978), 4U 1626−67 (Orlandini et al., 1998) and 4U 1822−371 (Sasano et al., 2014).

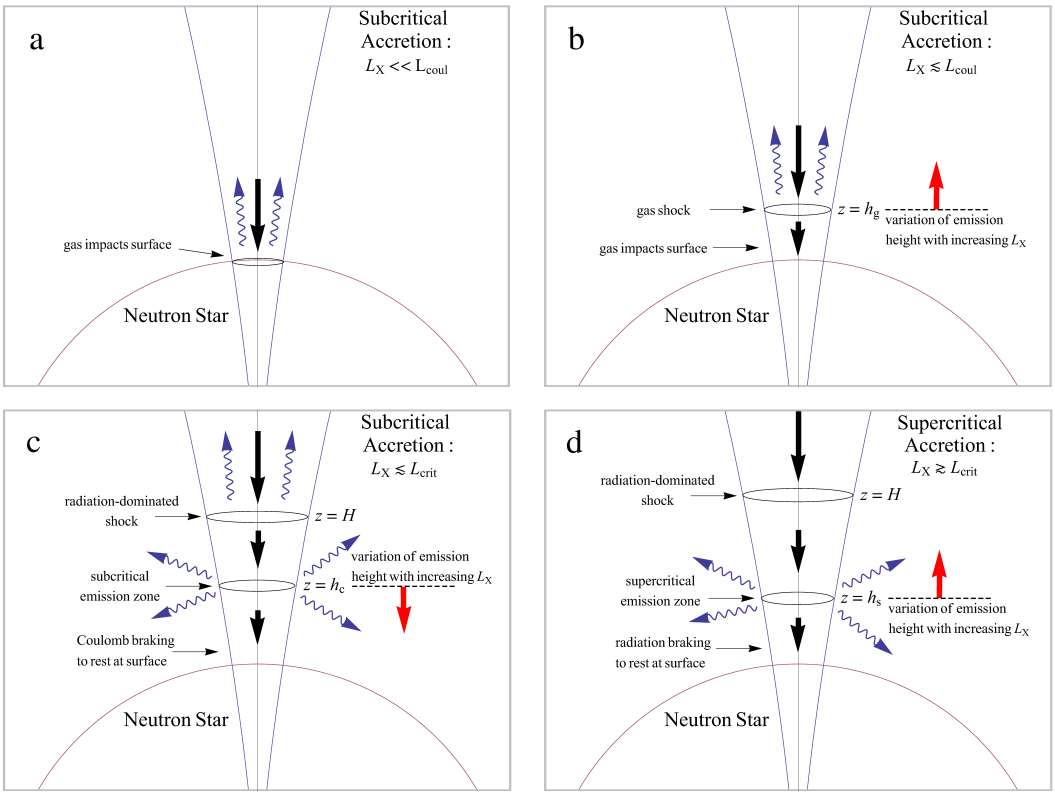

Figure 2.3: Sub- and super-critical accretion regimes (Becker et al., 2012, Fig. 1).

2.1.5 Sub- and super-critical regime

In accreting neutron star systems the accretion column geometry highly depends on the accretion rate. Becker & Wolff (2007) and later Becker et al. (2012) developed a model for these systems, assuming a cone-like geometry of the accretion column. Figure 2.3 gives a schematic overview of the different accretion regimes.

As first proposed in Basko & Sunyaev (1976), Becker et al. (2012) used a separation into two different regimes, based on the luminosity L_X of the system. The two regimes are roughly separated by the critical luminosity of $L_{\rm crit} \sim 10^{37}\,{\rm erg\,s^{-1}}$. This critical luminosity is related to the Eddington luminosity but takes the accretion geometry and magnetic field into account (see e.g. Kühnel et al., 2017). Further calculations of the critical luminosity were done by Mushtukov et al. (2015) and Postnov et al. (2015).

The system accretes "super-critical" if the luminosity exceed the critical value. The matter is decelerated by a radiation dominated shock until the neutron star's surface. Illustratively, one may think of a torch being held upstream with the photons stopping the impacting matter. In this regime the CRSF line-forming region is likely to be located as sheath around the accretion walls.

A system is said to accrete "sub-critically" if $L_X \lesssim L_{\rm crit}$. In this case the final deceleration happens due to Coulomb interactions or – at very low accretion rates – by a gas-mediated

shock. Note that in the Coulomb-dominated regime, the accretion column still exhibits a radiation-dominated shock region, though closer to the NS surface. Only the final deceleration is due to Coulomb interactions. In this case the CRSF forming region is thought to be a localized region within the accretion column as adumbrated in Fig. 2.1. The cyclotron line energy may dependent on the X-ray luminosity in some systems (e.g. in V 0332+53, see Doroshenko et al. 2017, or A 0535+26, see Caballero et al. 2007). In super-critical regime an increase in accretion rate ($\propto L_X$) will lead to an increase of the radiation dominated shock height. (Fig. 2.3d). Since the NS's magnetic field can be approximated by a dipole, an increase in height results in a decrease in magnetic field strength and therefore a decrease in CRSF centroid energy (12-B-12-rule in Eq. 2.2). On the contrary, if the system is in sub-critical regime with Coulomb breaking, an increase in accretion rate leads to a shift of the final stopping region closer to the surface and therefore to an increase in CRSF centroid energy.
I note that there are also reflection models which propose a CRSF formed at the NS's surface (Poutanen et al., 2013).

2.2 Spectral modeling of accreting X-ray binaries

2.2.1 Empirical and physical models

Lyubarskii & Syunyaev (1982) calculated that the resulting spectrum looks like a power-law[1] with an exponential cut-off at energies $\gtrsim k_B T_E$ where $6 \lesssim T_E \lesssim 30\,\mathrm{keV}$ denotes the electron temperature in the plasma. The cut-off power-law is additionally affected by interstellar absorption at low energies (Anders & Grevesse, 1989; Wilms et al., 2000; Asplund et al., 2009).
Starting with Zel'dovich & Shakura (1969), Basko & Sunyaev (1976), and Wang & Frank (1981) many attempts have been made to physically model the spectrum by numerically solving the radiative transfer equations (see also Meszaros & Nagel, 1985a,b; Becker & Wolff, 2007; Farinelli et al., 2016). While these models correctly reproduce the observed shape, the parameters often do not have a unique physical meaning.
Therefore, the spectra of X-ray pulsars have been mostly modeled empirically over the last decades (see also Müller et al. 2013). Nowadays, the standard packages in order to do spectral analyses are the *X-Ray Spectral Fitting Package* (Arnaud, 1996, XSPEC), the *Interactive Spectral Interpretation System* (Houck, 2002, ISIS) and *Sherpa* (Freeman et al., 2001). In the following I outline the models used in this thesis.

Cut-off power-law (`cutoffpl`)

The most simple realization is the so-called `cutoffpl`

$$I_E = K \cdot E^{-\Gamma} \exp(-E/E_{\mathrm{fold}}) \quad . \tag{2.3}$$

[1] $PL(E) = K \cdot E^{-\Gamma}$ with $0 < \Gamma \leq 2$ (Becker & Wolff, 2007)

I_E is the flux (or count) distribution as a function of energy, K the normalization constant, Γ the photon index – determining the slope – and E_{fold} the exponential folding energy[2]. This fit model represents a continuously steepening spectrum, however, often does not have enough parameters to describe the continuum sufficiently.

Fermi-Dirac Cut-off power-law (`FDcut`)

Tanaka (1986) introduced a model which describes the cut-off as Fermi-Dirac function:

$$I_E = K \cdot E^{-\Gamma} \left[1 + \exp\left(\frac{E - E_{\mathrm{cut}}}{E_{\mathrm{fold}}}\right)\right]^{-1} \tag{2.4}$$

This introduces one more degree of freedom which gives the fit better convergence behavior. However, some sources show a soft excess at low energies which cannot be modeled with the `cutoffpl` or `FDcut` alone but requires the addition of a black body component (e.g. Kühnel et al., 2013) or a "10 keV-feature", a very broad Gaussian emission line (Coburn et al., 2002).

Negative-positive power-law with exponential cut-off (`NPEX`)

The NPEX model (Mihara, 1995) intends to account for the soft excess and describes the continuum as a sum of two power-laws with positive and negative photon index:

$$I_E = K_1(E^{-\Gamma_1} + K_2 E^{+\Gamma_2}) \exp(-E/E_{\mathrm{fold}}) \tag{2.5}$$

Mostly, Γ_2 is set to the value of two to depict the Wien proportion of the thermal distribution.

Accretion disk and thermal continuum (`diskbb+nthcomp`)

The last model used in this thesis is a combination of a black body radiating accretion disk (Mitsuda et al., 1984; Makishima et al., 1986, `diskbb`) with a thermally Comptonized continuum (Zdziarski et al., 1996; Życki et al., 1999, `nthcomp`). The latter assumes a relatively simple accretion column geometry and does not take the magnetic field into account. However, some of the resulting parameters give direct input about the physics of the system[3].

Is has to be mentioned that all of these models exhibit drawbacks. This becomes relevant if one wants to models a CRSF. The model parameters have correlations to the CRSF, which is modeled by the `gabs` function in this thesis (see Sect. 3.3.1), and constrain its parameters differently. This can have drastic effects on the physical outcome of the analysis (e.g. disproof of $E_c - L_X$-dependence in 4U 0115+63, see Müller et al., 2013).

[2] E_{fold} is sometimes called E_{cut} and often interpreted as electron temperature

[3] The high energy roll-over $k_B T_e$ in the `nthcomp` model gives, for instance, the electron temperature in the plasma, whereas $k_B T_{bb}$ ought to give the seed photon temperature.

2.2.2 Fluorescence lines

Spectra of accreting X-ray pulsars often exhibit additional atomic features. As the hard X-ray radiation propagates through the walls of the accretion column, it illuminates the surrounding material. Some radiation is reflected on the accretion disk. The radiation is re-processed in the disk and imprints fluorescence lines onto the spectrum. Spectroscopy with sufficient resolution can therefore constrain the abundances within the accretion disk.

Iron is usually the best observable element in accretion disks. The disk reflection of neutral iron can be seen as Fe Kα emission line at 6.40 keV. Theory predicts an additional Fe Kβ line at 7.06 keV which has 12–13% of the $K\alpha$ flux (see Palmeri et al. 2003, Barragán et al. 2009 and references therein). Additionally, the accretion disk is often ionized and higher ionized species are also present (e.g. Fe XXV at 6.70 keV).
Most satellites, including *NuSTAR*, do not have sufficient energy resolution in order to resolve the individual ionization states and atomic transitions. Therefore, the iron complex is often modeled as one broad emission line.
A more sophisticated approach is to model all relevant atomic transitions. The atomic database *AtomDB*[4] can be used to infer the relevant element transitions. In the following section I outline the process of finding the relevant transitions on the example of highly ionized iron Fe XXV. More details can be found in Sect. 3.3.1.
Fe XXV exhibits two remaining electrons. These electrons can be excited from the ground state $1s^2$ by impacting X-ray radiation. See the glossary for an explanation of the electron configuration notation. Many different levels of excitation are possible, the most likely being the Kα transitions, where the electron is excited to the L-shell. The *AtomDB* gives the line energies for each transition: $1s^1\ 2p^1 \rightarrow 1s^2$ (6.673 keV), $1s^1\ 2p^1 \rightarrow 1s^2$ (6.677 keV), $1s^1\ 2p^1 \rightarrow 1s^2$ (6.692 keV), and $1s^1\ 2p^1 \rightarrow 1s^2$ (6.711 keV). There is one more possible excitation state in the L-shell: $1s^1\ 2s^1$. Transitions from there to $1s^2$ are, however, forbidden[5] because electrical dipole transitions require $\Delta\ell = 1$. In order to determine the energy at which the line ought to be modeled one has to calculate the mean of these transitions. To be very specific, one has to additionally take the exact branching ratios (the transition probabilities) into account.
If the lines emerge close to the neutron star surface one has to take red-shift into account, which shifts the line to lower energies. However, since the accretion disk is sufficiently distant from the NS, this can usually be neglected.

[4] http://www.atomdb.org/

[5] "Forbidden" transitions do occur, for instance as magnetic dipole transitions, however with much lower branching ratio

Chapter 3

Spectral analysis of *NuSTAR* data of GRO J1744−28 in low-flux state

3.1 The Low-mass X-ray binary GRO J1744−28

A comprehensive overview of the physics in accreting neutron stars has been given in Ch. 2. In the following, I will introduce the source GRO J1744−28.
GRO J1744−28 is a transient LMXB with a G4 III (Miller-Jones et al., 2007; Masetti et al., 2014) companion star. It was discovered on 1995 December 2 with the *Burst And Transient Source Experiment* (BATSE) on-board the *Compton Gamma Ray Observatory* (Kouveliotou et al., 1996) and is associated with a position near the Galactic center at a distance of 7.5–8.5 kpc (Augusteijn et al., 1997; Nishiuchi et al., 1999). GRO J1744−28 is one of the few LMXBs with a magnetic field that is strong enough that X-ray pulsations are observed, but has surface conditions that are still allowing the generation of thermonuclear and Type II X-ray bursts (see Sect. 2.1.3 for details). The source has therefore been often dubbed the "Bursting Pulsar". Finger et al. (1996) determined the pulse frequency to 2.14 Hz. The orbital parameters[1] were approximated to $P_{orb} = 11.836$ days, $T_{\pi/2} = 2456696.19880$ (JED), $a_x \sin(i) = 2.637$ light-sec on the basis of the 2014 outburst with no constrains on the longitude of periastron or eccentricity (Pintore et al., 2014).
About one year after its outburst in 1995, which lead to its discovery, the transient exhibited a similar outburst in 1996 December with the same burst characteristics (Woods et al., 1999; Doroshenko et al., 2015). After 18 years of quiescence the source went into outburst again in early 2014 which triggered *NuSTAR*/*Chandra* (Younes et al., 2015) as well as *XMM-Newton*/*INTEGRAL* (D'Aì et al., 2015) observations. In 2017 February the source underwent its fourth outburst which was observed with *NuSTAR* and analyzed in this thesis. A Swift/BAT monitoring lightcurve is shown in Fig. 3.1.
During the 2014 outburst, D'Aì et al. (2015) reported a fundamental CRSF line at

[1] https://gammaray.msfc.nasa.gov/gbm/science/pulsars/lightcurves/groj1744.html

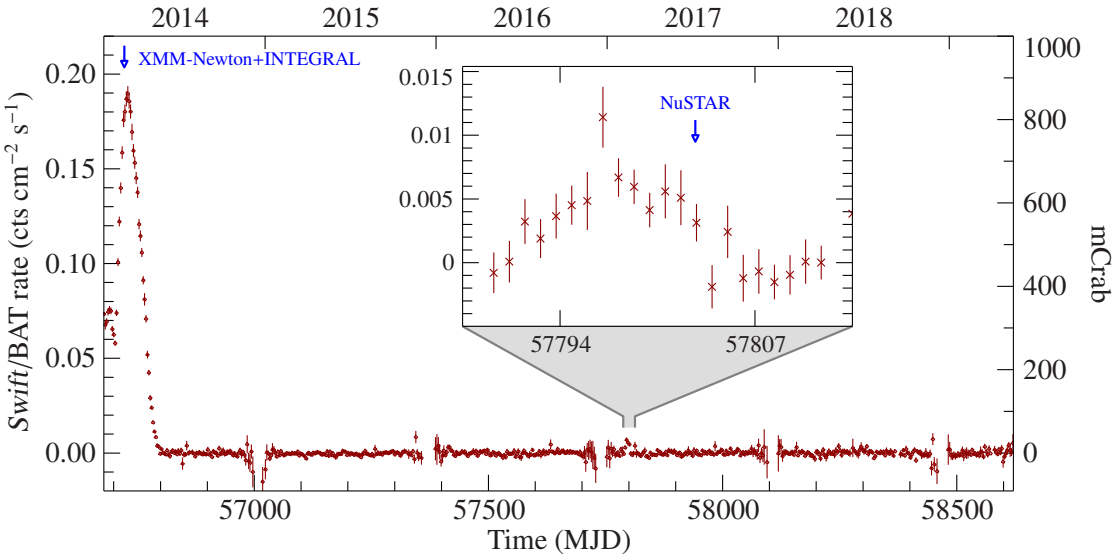

Figure 3.1: Swift/BAT lightcurve of GRO J1744−28. The outburst in 2014 had a luminosity of 2.1×10^{38} erg s^{-1}, slightly above Eddington limit (D'Aì et al., 2015). This outburst in 2017 is at luminosity 3.2×10^{36} $(D/8\,\mathrm{kpc})^2$ erg s^{-1} (3–50 keV). The gaps in the Swift/BAT lightcurve are due to visibility constraints.

4.68 ± 0.05 keV, with the indication of a second and third harmonic at 10.4 ± 0.1 keV and $15.8^{+1.3}_{-0.7}$ keV in *XMM-Newton/INTEGRAL* data (using `gabs`). Shortly later, Doroshenko et al. (2015) claim to have found a fundamental line at ~ 4.5 keV in *BeppoSAX* data taken during the 1997 outburst (also using `gabs`). This makes GRO J1744−28 one of the few LMXBs where a CRSF has been reported below 10 keV. Other candidates are X1822−371 with a claimed cyclotron line energy of 0.7 keV (Iaria et al., 2015) and SWIFT J0051.8−7320 at 5 keV (Maitra et al., 2018).
The polar magnetic field deduced from the CRSF energy, 5×10^{11} G, is low enough that X-ray bursts are not inhibited. The detection of the CRSF, however, is debated. Younes et al. (2015) did not find a significant CRSF in their data, which was taken only three days earlier than the D'Aì et al. (2015) detection. The magnetic field strength deduced from disk reflection models lies in the $2\text{–}6 \times 10^{10}$ G range (Degenaar et al., 2014) which mismatches the values deduced from the CRSF measurements by one order of magnitude.

In this chapter, I present the analysis of *NuSTAR* observations of GRO J1744−28 taken during its most recent outburst. In Sect. 3.2, I discuss the data extraction and calibration. I then present the results of the phase-averaged and phase-resolved spectroscopy in Sect. 3.3.1 and 3.3.2, respectively, and discuss the search for a CRSF. I discuss my results in Sect. 3.4. This analysis has been performed under the supervision of F. Fürst, and P. Kretschmar from ESAC, and J. Wilms from the Dr. Karl Remeis Observatory Bamberg. Furthermore, this collaboration involves R. Ballhausen, E. Sokolova-Lapa, and T. Dauser from the Dr. Karl Remeis Observatory, M. Bissinger (ECAP), P. B. Hemphill (MIT), K. Pottschmidt (NASA GSFC) as well as C. Sánchez-Fernández from ESAC.

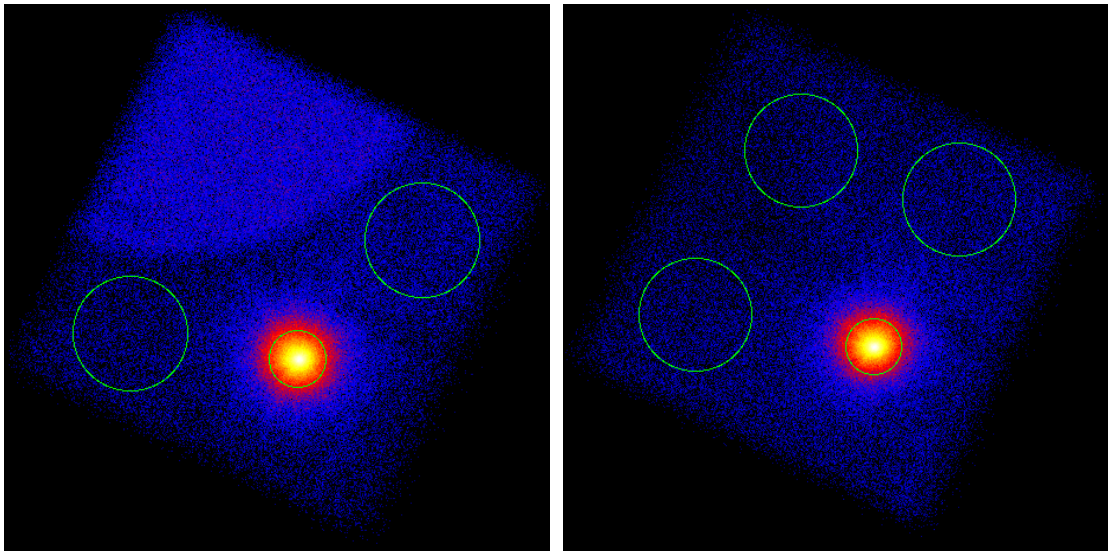

(a) FPM A **(b)** FPM B

Figure 3.2: 60 arcsec source regions and 120 arcsec background regions for data extraction. The illuminated region in the FPM A image is due to stray light contamination from a near source.

3.2 Data extraction & calibration

An introduction of the *NuSTAR* satellite has been given in the introduction. This data consist of a 28825 s (FPM A) and 28919 s (FPM B) *NuSTAR* observations starting on 2017-02-18 14:34:35 UTC (MJD 57802.6073, ObsID: 80202027002). I reduce the data with HEASOFT version 6.26 (corresponding to NuSTARDAS 1.8.0), using *NuSTAR* CalDB version 20190513. I barycenter the data and extract the events from the source region with a circle of 60 arcsec radius. For the background extraction I define three circular regions of 120 arcsec radius for FPM B and two circles of the same size for FPM A due to stray light contamination (Fig. 3.2). The event files were then filtered on the source region with XSELECT version 2.4g.

All further analysis was performed with the *Interactive Spectral Interpretation System* (Houck, 2002, ISIS version 1.6.2-43). Unless stated otherwise, all error bars are at the 90% level single parameter confidence level ($\Delta\chi^2 = 2.71$). I restrict the data to the 3–78 keV range (PI channel 35–1210) and bin it to a minimum signal-to-noise ratio of 5. I use following binning scheme for the phase-averaged and phase-resolved spectra to account for *NuSTAR*'s effective area: In energy range 3–10 keV, I group a minimum number of 2 channels per bin, in range 10–15 keV: 3 channels, 15–20 keV: 5, 20–35 keV: 8, 35–45 keV: 16, 45–55 keV: 18, 55–65 keV: 48, 65–76 keV: 72, and in the range >76 keV, I bin 48 channels per bin.

3.3 Results

3.3.1 Phase-averaged spectrum

In Sect. 2.2.1, I outline the difficulties in modeling the continua of accreting neutron stars with physical models. Therefore, I describe the extracted spectrum with the usually applied phenomenological models. The residua of the `cutoffpl`, `FDcut`, `NPEX` and `diskbb+nthcomp` models are plotted in Fig. 3.3 and the best fit parameters are given in Table 3.1. All tested continuum models describe the data similarly well. Due to its simplicity and comparability with previous work (Doroshenko et al., 2015; Younes et al., 2015), I use the `cutoffpl` model for all subsequent analysis.[2] Multiple Gaussian emission lines are added to describe the iron line complex. Absorption is accounted for with the `tbnew` model. Hereby, photoelectric absorption in the interstellar medium is described with the `vern` cross sections (Verner et al., 1996) and `wilm` abundances (Wilms et al., 2000). This model gives a good description of the overall continuum shape (χ^2/dof=462.2/407=1.14). The observed 3–50 keV flux of 4.15×10^{-10} erg cm^{-2}s^{-1} translates to a luminosity of $3.2 \times 10^{36}\,(D/8\,\mathrm{kpc})^2$ erg s^{-1} (3–50 keV), assuming spherical emission. This is roughly two orders of magnitude lower than what was seen in the 1997 and 2014 outbursts.

The iron complex can formally be described by a slightly broadened ($\sigma = 0.23^{+0.05}_{-0.04}$ keV) Gaussian component at 6.59 ± 0.04 keV. The structure, however, is also consistent with a set of narrow lines from neutral Fe (Fe Kα at 6.404 keV and Kβ at 7.058 keV, with a flux of 13% of the Kα line; Palmeri et al. 2003), as well as Fe Kα lines from Fe XXV and Fe XXVI at 6.700 keV and 6.960 keV, respectively (see Sect. 2.2.2). The motivation behind this more "physical" approach is that modeling all relevant physical line transitions and fixing their rest frame energy in principle allows to constrain the ionization state of the system. However, *NuSTAR* does not provide sufficient energy resolution to resolve the components and thus both approaches are statistically valid.

In the context of the previous CRSF reports at 5 keV I further analyze the spectrum to search for a cyclotron line. The most common phenomenological model is a multiplicative Gaussian absorption line (`gabs`) of the form $e^{-\tau(E)}$ with the optical depth

$$\tau(E) = \tau_0 e^{-\frac{(E-E_c)^2}{2\sigma^2}} \tag{3.1}$$

and τ_0 the central optical depth. This fit model introduces the parameter "strength" (in keV) equalling $\tau_0\sqrt{2\pi}\sigma$ which is widely used in order to determine the significance of cyclotron lines. According to Fig. 2.2 theory predicts a width of ∼1 keV at the reported 5 keV energy. Indeed, Doroshenko et al. (2015) found a width of 1.2 ± 0.3 keV whereas D'Aì et al. (2015) found a width of 0.68 ± 0.08 keV. In order to calculate an upper limit on the strength I fix the width to 1 keV (otherwise the width is fitted to unphysical values). The addition of the cyclotron line, however, does not give improvement in χ^2 and I give an upper limit of 0.07 keV on the strength of this `gabs` component.

[2] `tbnew*const*(enflux(cutoffpl)+4*egauss)` with norm of `cutoffpl` frozen to 0.01 to avoid degeneracy to `enflux`.

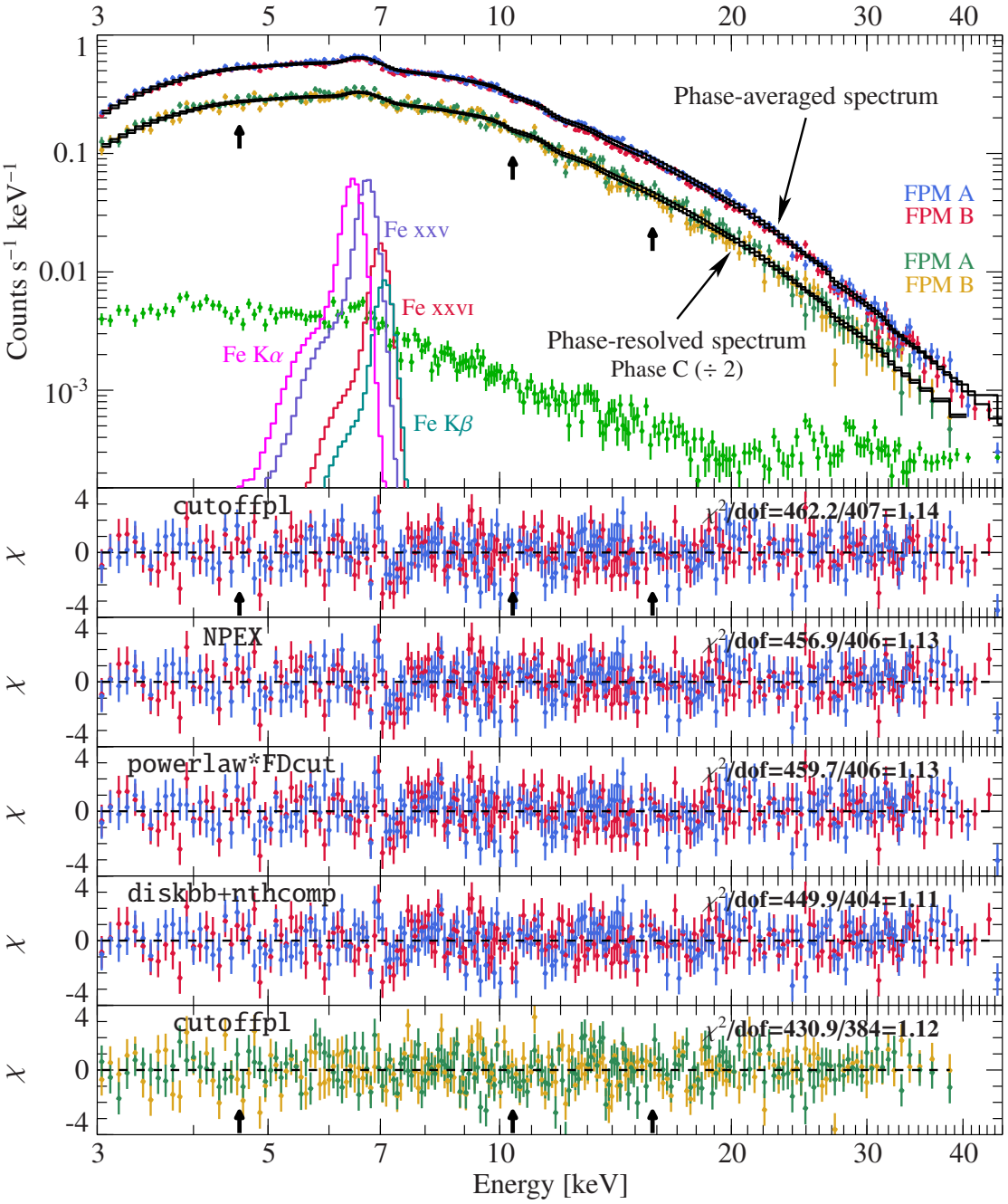

Figure 3.3: Phase-averaged and phase-resolved (phase C, displaced by factor 2 for visualization) spectra. Black histogram gives the best fitting model: an absorbed cut-off power-law with iron component at ∼6.5 keV. Green points show background of FPM A. Arrows indicate the location of the reported CRSFs (Doroshenko et al., 2015; D'Aì et al., 2015). The `NPEX` and `FDcut` residua look very similar, because they are driven to parameters which effectively mimic the `cutoffpl` solution (see Table 3.1). The iron line asymmetry is due to the convolution with the detector response and the logarithmic scale.

Table 3.1: Fit parameters for various models

	phase-resolved	phase-averaged			
Parameter	`cutoffpl*gabs` (phase C)	`cutoffpl`	`NPEX`	`FDcut`	`diskbb+nthcomp`
$N_{\rm H}$ ($10^{22}\,{\rm cm}^{-2}$)[d]	4.9[a]	4.9 ± 0.6	4.5 ± 0.6	5.9 ± 0.6	10 ± 4
Γ	0.46 ± 0.06	0.53 ± 0.05		$0.83^{+0.08}_{-0.04}$	$1.81^{+0.06}_{-0.05}$
$E_{\rm fold}$ (keV)	8.5 ± 0.4	$9.03^{+0.24}_{-0.23}$	$5.56^{+0.24}_{-0.20}$	9.24 ± 0.21	
$E_{\rm cut}$ (keV)				≤ 3.19	
Flux (erg cm^{-2}s^{-1}, 3–50 keV)	0.290 ± 0.004	$0.2711^{+0.0026}_{-0.0025}$			
α_1			0.25 ± 0.04		
α_2[a]			-2		
kT_e (keV)					$5.99^{+0.25}_{-0.22}$
$kT_{\rm BB}$ (keV)					$1.41^{+0.20}_{-0.12}$
$kT_{\rm disk}$ (keV)					$0.71^{+0.29}_{-0.12}$
Norm$_{\texttt{diskbb}}$					30^{+120}_{-40}
$E_{\rm Fe\ K\alpha}$ (keV)[ae]		6.404	6.404	6.404	6.404
Flux (10^{-4} ph s^{-1}cm^{-2})		1.23 ± 0.26	1.20 ± 0.26	1.25 ± 0.26	$1.12^{+0.30}_{-0.31}$
$E_{\rm Fe\ K\beta}$ (keV)[ae]		7.058	7.058	7.058	7.058
Flux (10^{-5} ph s^{-1}cm^{-2})[b]	Scaling constant=$0.79^{+0.24}_{-0.23}$	1.6	1.5	1.6	1.4
$E_{\rm Fe\ XXV}$ (keV)[ae]		6.7	6.7	6.7	6.7
Flux (10^{-4} ph s^{-1}cm^{-2})[c]		1.20 ± 0.28	1.20 ± 0.28	1.19 ± 0.28	$1.11^{+0.29}_{-0.30}$
$E_{\rm Fe\ XXVI}$ (keV)[ae]		6.98	6.98	6.98	6.98
Flux (10^{-5} ph s^{-1}cm^{-2})		3.3 ± 2.3	3.2 ± 2.3	3.8 ± 2.3	$2.8^{+2.5}_{-2.6}$
$E_{\rm gabs}$ (keV)	$8.7^{+0.8}_{-1.0}$	7^{+13}_{-4}			
$\sigma_{\rm gabs}$ (keV)[a]	1.0	1.0			
Strength (keV)	≤ 0.15	≤ 0.07			
Norm	0.01[a]	0.01[a]	$0.0120^{+0.0010}_{-0.0009}$ $\left(1.21^{+0.27}_{-0.28}\right) \times 10^{-3}$	$0.0364^{+0.0025}_{-0.0037}$	$\left(3.3^{+0.8}_{-0.9}\right) \times 10^{-3}$
Displacement constant	0.965[a]	0.965 ± 0.007	0.965 ± 0.007	0.965 ± 0.007	0.965 ± 0.007
χ^2 (dof)	397.9/386	462.2/407	456.9/406	459.7/406	449.9/404
$\chi^2_{\rm red.}$	1.03	1.14	1.13	1.13	1.11

Notes: Uncertainties are at 90% confidence level; `wilm` abundances, `vern` cross-sections.
[a]Parameter frozen; [b]Tied to $0.13 \cdot {\rm Flux}_{\rm Fe\ K\alpha}$, see Palmeri et al. (2003, fig.2); [c]Evaluated between transitions $1s^1\ 2p^1 \rightarrow 1s^2$ (6.673 keV), $1s^1\ 2p^1 \rightarrow 1s^2$ (6.677 keV), $1s^1\ 2p^1 \rightarrow 1s^2$ (6.692 keV), $1s^1\ 2p^1 \rightarrow 1s^2$ (6.711 keV); [d]Iron abundance frozen at solar; [e]Narrow line with frozen width $\sigma = 10^{-6}$ keV

3.3.2 Phase-resolved spectra

Although no significant cyclotron line is found in the phase-averaged spectrum, it is still possible that the phase-resolved spectra exhibit such a line: If the CRSF is produced in a very localized region, it may only be evident at certain phases of the neutron star rotation.

Epoch folding

Lightcurves of neutron stars can exhibit strong oscillations which are due to the NS's rotation. The neutron star is said to *pulse*. In order to find the pulse period a technique called *epoch folding* is used (Leahy et al., 1983; Schwarzenberg-Czerny, 1989). It utilizes a convolution of the lightcurve on a test period and distributes the events into phase bins according to

$$\text{Pulse phase } \phi = \frac{(t - t_0) \mod P}{P} \quad . \tag{3.2}$$

t is the time, t_0 the start time and P the test period. Then, the pulse phases are binned into a histogram. If the test period equals the actual oscillation in the lightcurve – i.e. the pulse period is correct – the outcome of the histogram is called the *pulse profile* (see Fig. 3.5). If the test period does not match any oscillation, the profile will yield a constant mean count rate. Assuming the null hypothesis "there is no oscillation in the resulting profile", one can perform a χ^2-test where large χ^2-values indicate rejection of the null hypothesis. Therefore, when folding the lightcurve on many test periods, the best pulse period can be read off the peak of the χ^2 landscape. The error scales roughly as $P/(NT)$ where P is the best fit period, N the number of phase bins, and T the total duration of the observation.
This technique yields a pulse period of 0.4670444(6) s (Fig. 3.4). I did not do an orbit correction because the orbit is poorly constrained. This is a valid approximation because the total elapsed time is only ∼5% of the orbital period of ∼11.8 days. Therefore, I do not expect large changes of the pulse period during the observation and the small Doppler shift due to the orbital motion can be neglected for the further analysis. The determined period is consistent with those from earlier measurements (Doroshenko et al., 2015; Younes et al., 2015; D'Aì et al., 2015), indicating that little torquing of the neutron star happens during the outbursts, which is consistent with a weak magnetic field.

Pulse profiles

Figure 3.5 (upper panel) shows pulse profiles for a barycentric reference time of $t_0 =$ MJD 57802.6073. Differences between FPM A and FPM B are statistical only, and therefore in the following study of the phase dependency of the X-ray spectrum, I analyze the joint data from both detectors. The pulse profile is single peaked and roughly sinusoidal. The colored histograms plot the pulse profile in different energy bands, showing that it does not show significant energy dependence. Pulse profiles of previous outbursts, e.g. in Younes et al. (2015), are smoother and more sinusoidal.

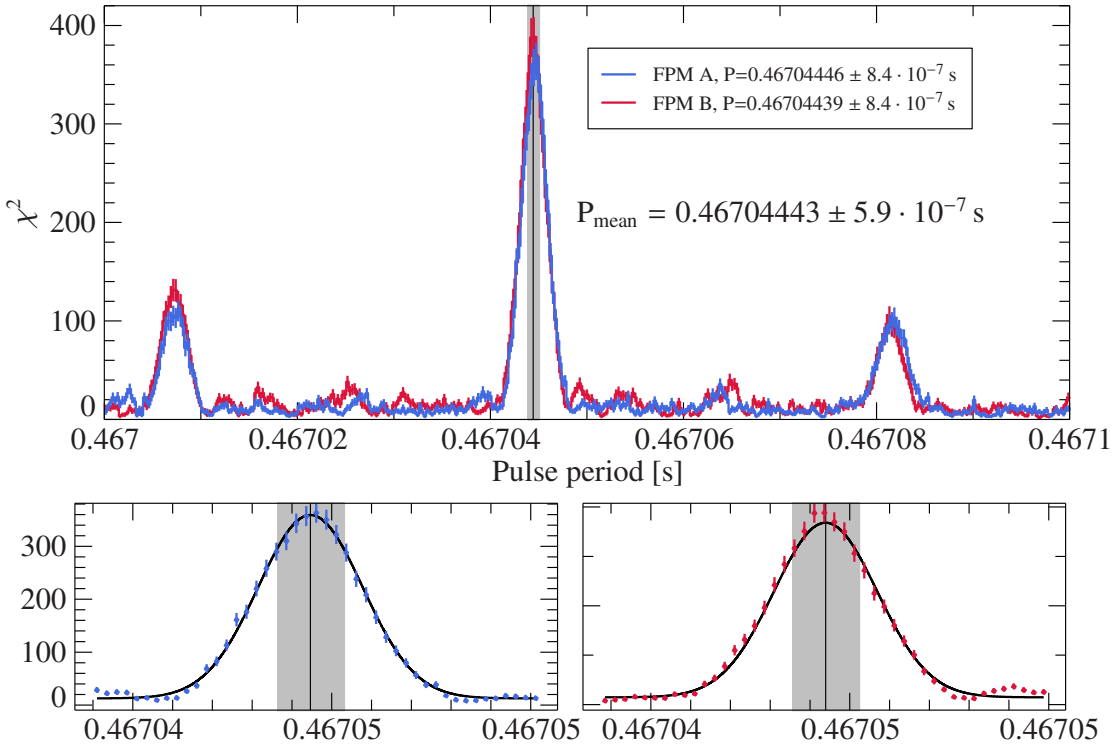

Figure 3.4: χ^2-landscape as a result of lightcurve epoch folding. The best pulse period can be read off the peak of the distribution. The pulse period is the weighted average of the FPM A and FPM B peaks, determined by a Gaussian fit.

The hardness ratios (Fig. 3.5 lower panel) can be obtained by dividing hard and soft band according to $(\mathrm{h}-\mathrm{s})/(\mathrm{h}+\mathrm{s})$. Plotting the phase-resolved hardness ratio generally gives a good hint on how to define the phase bins for the phase-resolved spectra. One chooses the bins such that the variation within the bin is low, while still having enough counts in each bin to apply χ^2-statistics. I use a so-called phase-resolved pulse-profile energy map (Fig. 3.6) to infer the bands of the hardness ratios. In this map one plots the count rates as function of energy and phase which gives a good overview of pulse profile and the phase-resolved spectra. A large fraction of counts is located at phase C–D (as also visible in the pulse profile) and between 3–20 keV. The energy range above ∼25 keV does not exhibit any clear, distinct features, therefore, I choose the soft band to be 3–8 keV, and hard band as 8–20 keV. Choosing higher energy bands (e.g. 3–8 keV and 20–78 keV) results in noisy hardness ratios which makes it difficult for a clear assessment of the phase bins. In Fig. 3.5, one can see the six defined phase bins. Phase lags at the proposed CRSF energies cannot be identified.

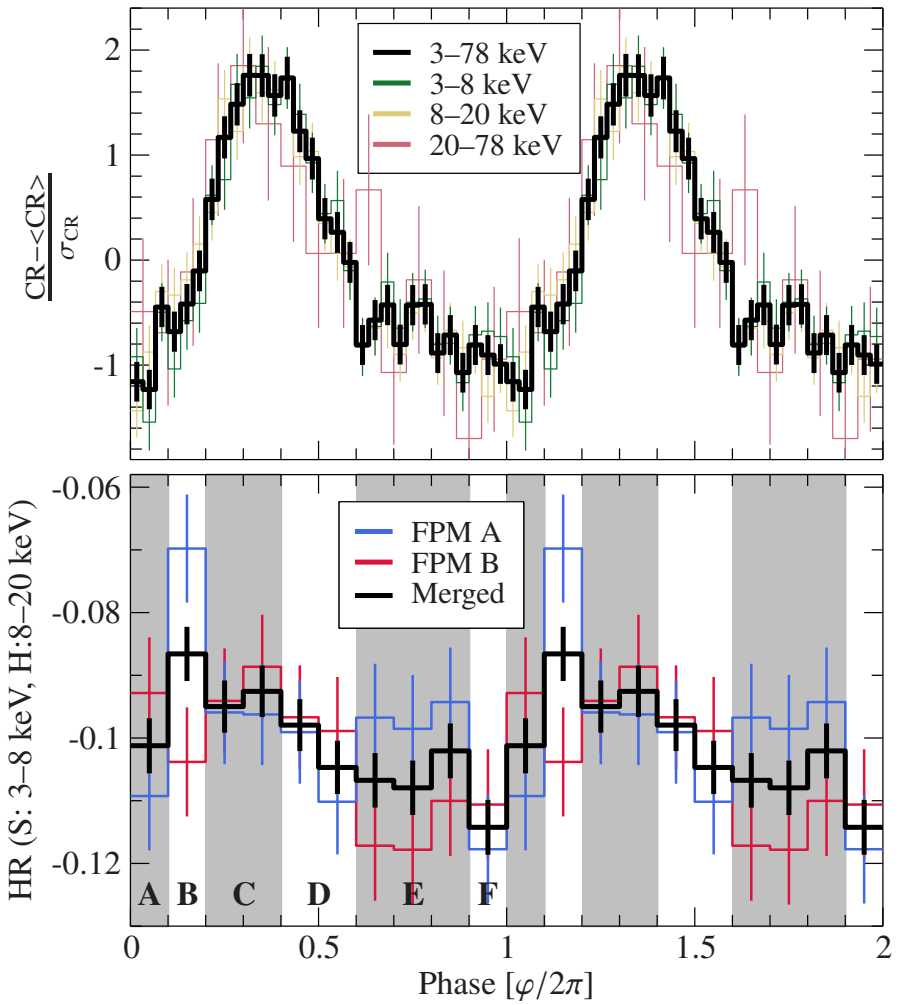

Figure 3.5: *Upper panel:* Standardized pulse profiles of GRO J1744−28 for the whole 3–78 keV band (black) as well as for three narrower energy bands (colored) show that there is no significant energy dependence. *Lower panel:* Variation of the hardness ratio, $(h - s)/(h + s)$, with phase, calculated for a soft band of 3–8 keV and a hard band of 8–20 keV. The gray bands show the phase ranges chosen for pulse phase spectroscopy. Black line gives the hardness ratios for the combined data from FPM A and B.

Continuum variability

Because the count offset between detector FPM A and FPM B is instrument-specific and cannot change over phase, I freeze the detector constant to the phase-averaged fit value of 0.965. I fix the iron line parameters to the phase-averaged values and multiply them by a constant to shift the flux of the iron complex up and down. Absorption is mostly dominant below 2 keV. Experience also shows that there may be some degeneracy between Γ and N_{H}, simply because having a softer power-law and absorbing more soft

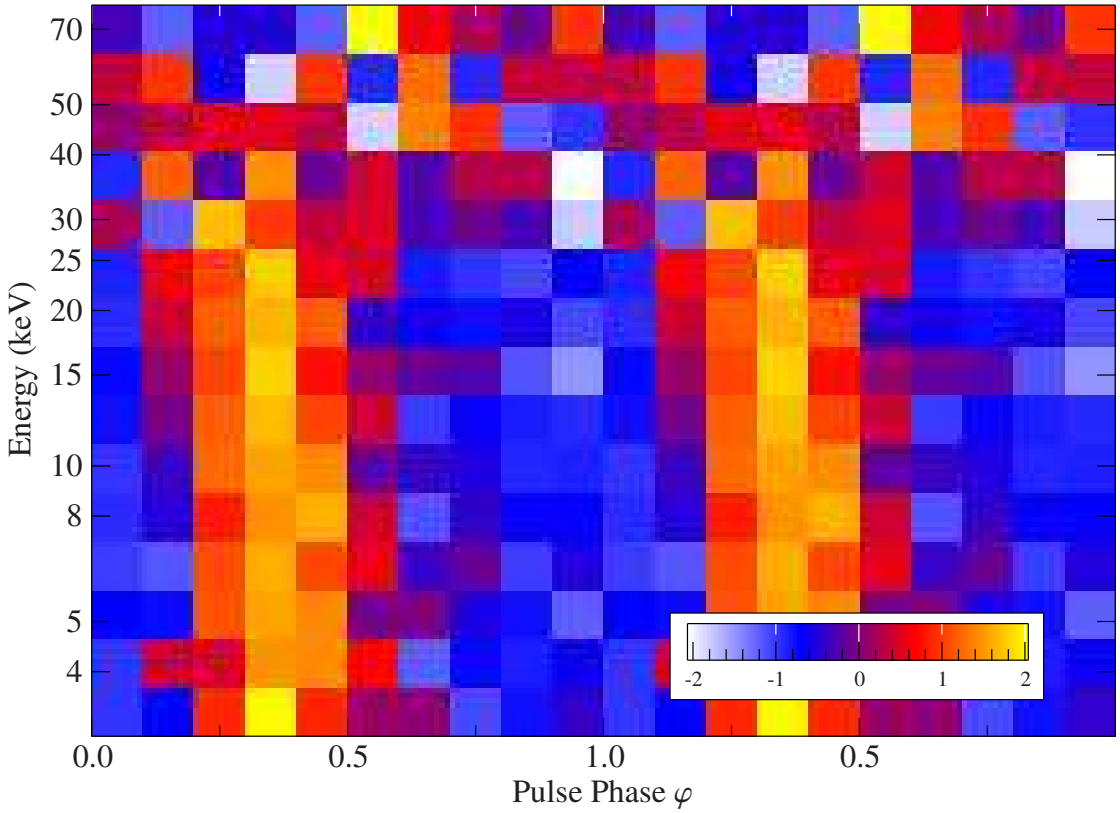

Figure 3.6: Pulse-profile energy-map of merged event files (FPM A+B). The color scale gives the standardized count rate (*standardized* defined as in pulse profile in Fig. 3.5). Reading the map from left to right mirrors the pulse profile. Vertical cuts resemble the spectrum for the selected phase interval. This visible energy dependence helps to define the hardness ratio bands in Fig. 3.5.

photons looks similar to a hard power-law with little absorption. Consequently, the spectral evolution of the column density N_{H} is difficult to determine with *NuSTAR* alone. Therefore, I fix N_{H} to $6.35 \times 10^{22}\,\mathrm{cm}^{-2}$ from the phase-averaged best fit. The remaining free parameters of the fit model are plotted in Fig. 3.7.

Photon index Γ and folding energy E_{fold} are seen to be degenerate in some sources (e.g. Ferrigno et al., 2011). To investigate a possible parameter degeneracy, I plot the confidence contours in Fig. 3.8. The elongated shape indeed shows a parameter degeneracy: An increasing photon index simultaneously increases the folding energy which compensates the softening of the spectrum. The 90% confidence levels of all phases overlap, showing that I can obtain equally well fits with the same pair of $(\Gamma, E_{\mathrm{fold}})$. Note that the phase-average $(\Gamma, E_{\mathrm{fold}})$ lies within all confidence contours.

Overall one can say that the spectral evolution of the model parameters is approximately constant and no significant spectral variability can be seen.

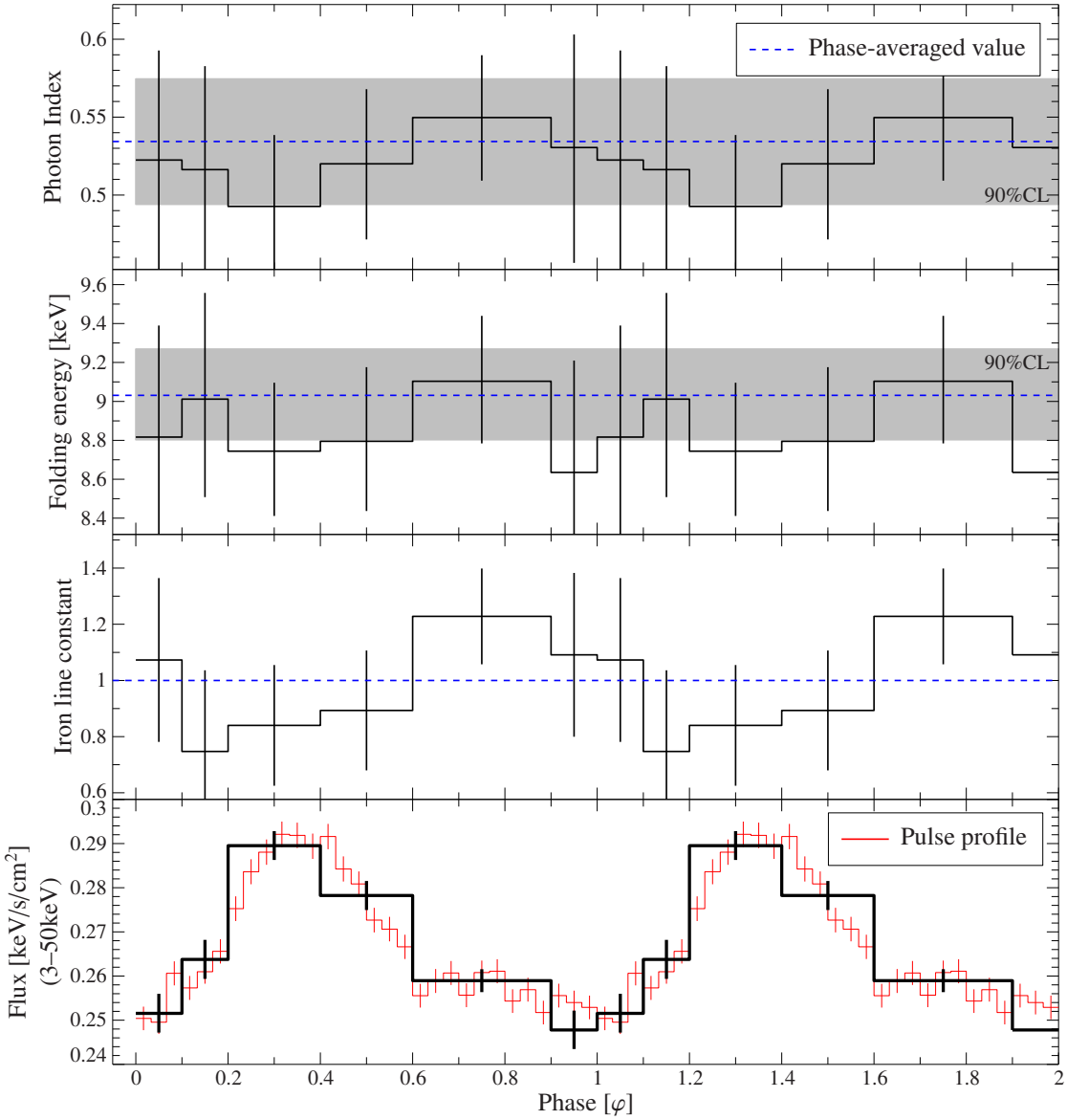

Figure 3.7: Phase-resolved continuum parameters of the fit model. Blue dashed line display the phase-averaged values with 90% confidence level (shaded). Note that the cut-off power-law norm is fixed to 0.01 (to avoid degeneracy with `enflux`), the FPM A and FPM B conversion constant to 0.965 and the column density to $6.35 \times 10^{22}\,\mathrm{cm}^{-2}$ from the phase-averaged best fit. The "iron line constant" shows the variation of the relative strength of the iron line complex, whose parameters have been otherwise fixed to the phase-averaged values. In the lowest panel I plot the (re-scaled) pulse profile. Errors are at the 90% confidence level.

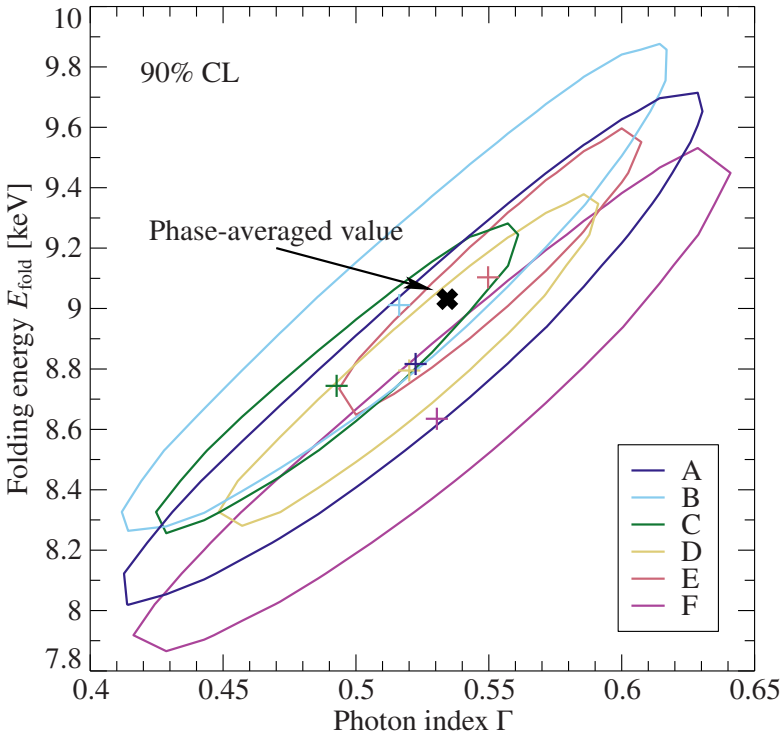

Figure 3.8: Confidence contours for all phases at 90% confidence level. Black cross gives best fitting parameters of the phase-averaged spectrum. The intersection of the contours shows, that it is possible to get a good fit with the same pair of Γ and $E_{\rm fold}$ for all phase-resolved spectra. This is already adumbrated in the single parameter uncertainties in Fig. 3.7.

Cyclotron line search in phase-resolved spectra

I scan the 3–20 keV region where cyclotron lines have been reported at 5 keV, 10 keV and 15 keV using the ISIS function `steppar`. This algorithm steps the Gaussian center position through the given range and performs a fit at each energy. I subtract each χ^2-value from the χ^2-value without absorption line which yields the $\Delta\chi^2$-landscape seen in Fig. 3.9. As before, I fix the width of the cyclotron line to 1 keV such that only the strength is fitted. This is necessary because the width trends to be fitted to very small, unphysical values. A cyclotron line width of 1 keV is a good approximation for 5 keV, but getting worse at larger energies where the width should increase to ∼3 keV at 15 keV (cp. Fig. 2.2). In order to find a significant deviation from the model without absorption line, I use the *Akaike Information Criterion* (Akaike, 1974). This is a statistical test which estimates the improvement of one model with respect to the other. A mathematical description is given in Sect. A.2 of the appendix.

The `gabs` model has three parameters. The centroid energy is frozen by the stepping algorithm and the width is frozen to ensure physically reasonable fits. Thus, the model

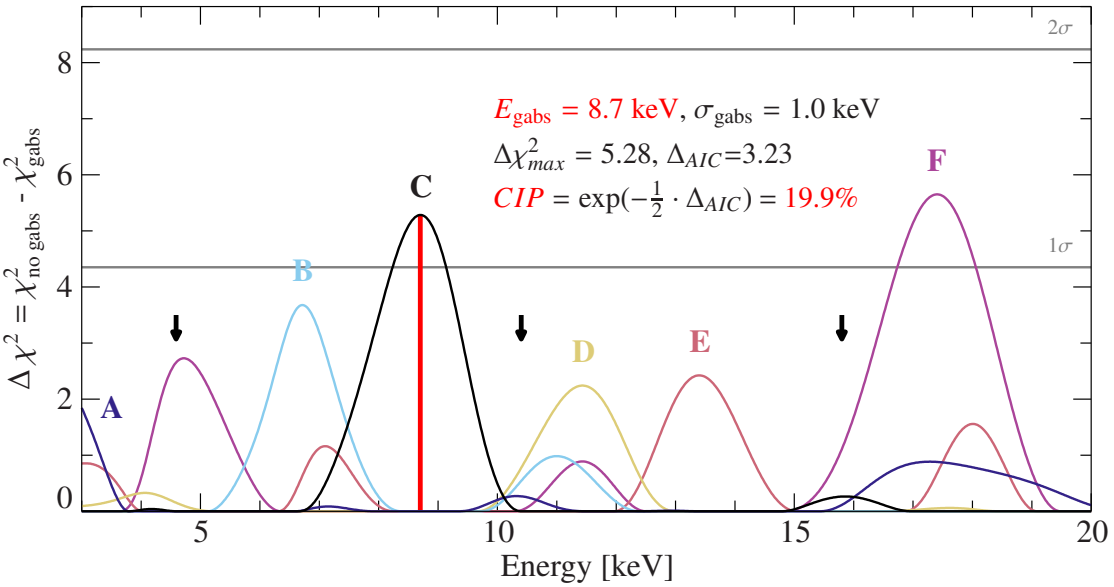

Figure 3.9: $\Delta\chi^2$ plotted as a function of energy to find a significant absorption line in the phase-resolved spectra. The y-axis is given by the difference in χ^2 value with and without absorption line. No phase shows an absorption feature with $> 2\sigma$ significance. Significance levels are calculated from Eq. A.9. Black arrows show the reported CRSF energies (Doroshenko et al., 2015; D'Aì et al., 2015).

with absorption line has one more free parameter, namely the strength of the cyclotron line. I cannot find any significant deviation in the resulting $\Delta\chi^2$-distribution. No phase exhibits a significance larger than 2σ. To be specific, the largest $\Delta\chi^2$ in phase C yields a *Chance Improvement Probability* (CIP, see Eq. A.8) of 20%, meaning that in about one in six cases the line would emerge due to statistical fluctuations[3]. This is clearly not significant and could very well be noise.

3.4 Discussion

3.4.1 Continuum analysis

I detect one broad emission hump at ∼6.6 keV which is likely a disk reflection component: The X-ray radiation hits the highly ionized accretion disk with large iron abundance and is re-emitted at the iron emission line energies. A possible origin from a fast disk wind has been reported, too (Degenaar et al., 2014). The non-existence of Type II burst, which so far have been detected in all three outbursts (Kouveliotou et al., 1996; Woods et al., 1999; Younes et al., 2015), is likely due to the fact that the accretion of the system is not sufficiently high to launch the spasmodic bursting.

[3] 1 in $1/(1 - \mathrm{erf}(\sigma/\sqrt{2}))$

3.4.2 CRSF search and Monte-Carlo simulations

In this section I discuss how deep the cyclotron line strength ought to be, to be significantly detected in these *NuSTAR* data. I simulate 20 000 fake spectra based on the exposure and best fit model of the phase-averaged spectrum (without `gabs`). The data points are drawn from a Poisson-distribution with mean at the model value. The background is approximately two orders of magnitude lower then the source data (see Fig. 3.3). Therefore, it is acceptable to neglect faking the background. By this approach the S/N-ratio of the data will directly affect the amount of absorption features emerging due to statistical fluctuations. By analyzing this number one can put a lower limit on the cyclotron line strength and determine whether one would have been able to see the CRSF as previously reported.

I fit the simulated spectrum with the best phase-averaged fit model plus an additional Gaussian absorption feature[4] and extract the strength and energy of the fitted `gabs` (Fig. 3.10). I constrain the fitted line energy of `gabs` to be above 4 keV in order to avoid the line running into *NuSTAR*'s lower energy limit. The start value of the line energy is 5 keV. Additionally, I freeze the width to 1 keV as before – otherwise the width is almost always fitted to the lowest possible value.

In Sect. 3.3.1, I determine an upper limit of 0.07 keV on the strength of a CRSF. As the `gabs` strength of D'Aì et al. (2015) and Doroshenko et al. (2015) is at 0.087 keV and ∼0.12 keV, respectively, I can rule out a line as strong as claimed in these report. It is likely that I would have seen a trace of the CRSF if it was as strong as previously reported. However, the fake simulations yield many lines above their `gabs` strength.

I conclude that a line detection at the reported strength would not be statistically tenable based on these low S/N data. In other words, it is not possible to confirm or deny a line as reported for the 1997 and 2014 outburst. A further illustration is given if one plots the CRSF properties of previous claims into the residua of these *NuSTAR* data (Fig. 3.11).

In order to obtain how strong a cyclotron line of 4σ confidence level must be in these *NuSTAR* data, I scan the "`gabs` strength" distribution for the value where it exceeds the required false rate of 6.3×10^{-5} (4σ). Thus, I put a 4σ detection limit of 0.15 keV on the strength of the cyclotron line.

The question imposes itself why this 2017 outburst does not yield a CRSF at ∼5 keV like previously reported. The 2014 outburst was extremely bright, placing the source in super-critical accretion regime – with 2.1×10^{38} erg s^{-1} slightly above the Eddington limit (D'Aì et al., 2015). The luminosity of this outburst is about two orders of magnitude below the critical luminosity, placing the source in sub-critical regime, where the final deceleration happens due to Coulomb interactions or a gas-mediated shock. Consequently, the accretion column is smaller and the line forming region closer to the magnetic field which could shift the cyclotron line energy to larger energies. However, I could not detect any significant absorption feature at larger energies, either.

[4] `tbnew*gabs*constant*(enflux(cutoffpl)+4*egauss)`

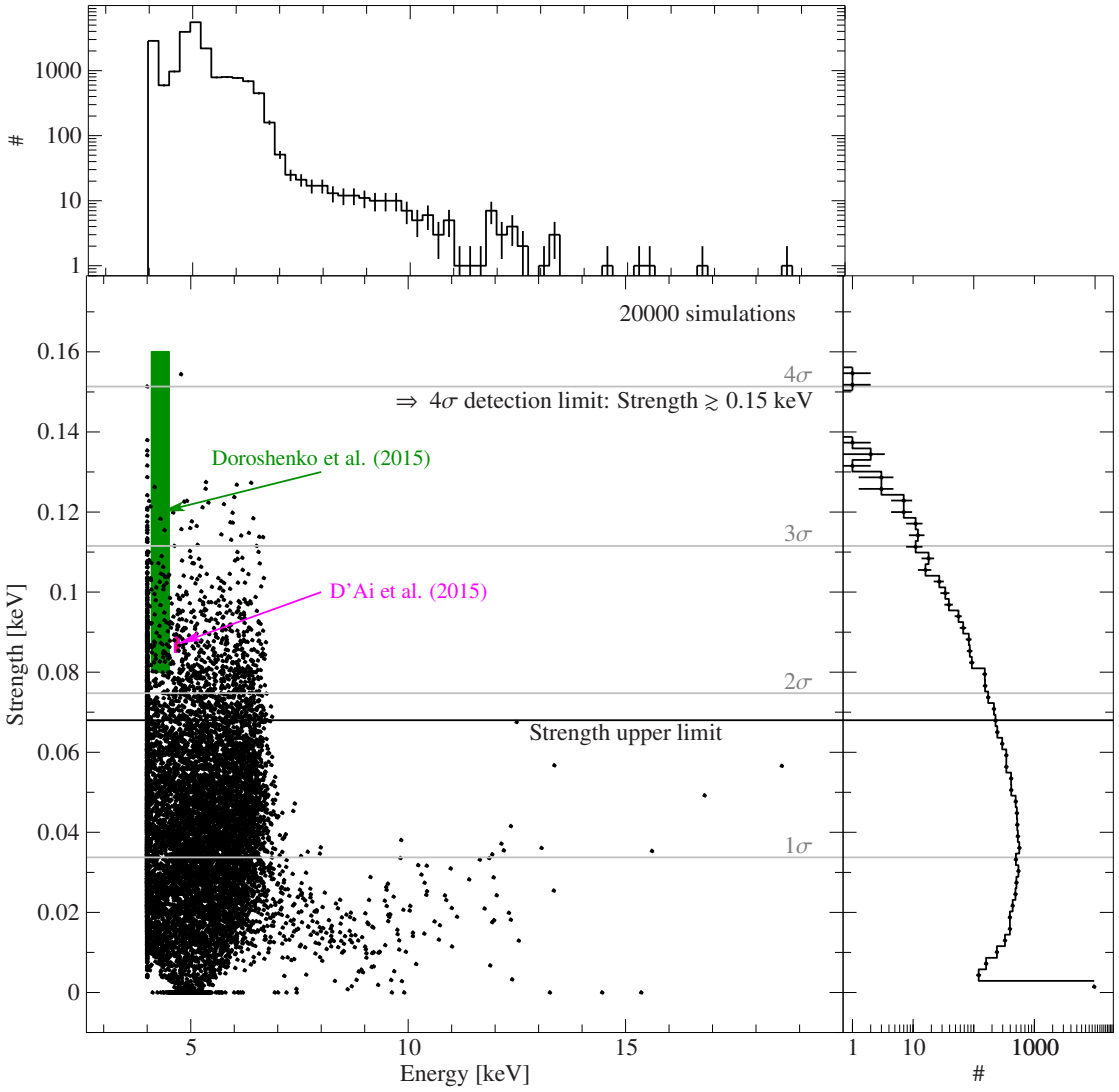

Figure 3.10: Monte Carlo Simulation of 20 000 fake spectra to determine a lower limit on the strength of a significant cyclotron line detection. Statistical fluctuations will lead to artificial absorption features, fitted with a `gabs` model. This plot shows the distribution of the extracted strength and energy. I determine a 4σ detection limit of 0.15 keV on the strength of a significant CRSF detection. 7% of the fits are above the phase-averaged upper limit strength of 0.07 keV.

It is to be noted that Doroshenko et al. (2015) did not observe the line ($\tau = 0$) in the late state of the outburst, where the flux has already decreased to $0.46 \times 10^{37}\,\mathrm{erg\,s^{-1}}$ (2–10 keV). Younes et al. (2015) did not see a CRSF either, whereby they analyzed data three days earlier (in the rising phase of the outburst) than the D'Aì et al. (2015) CRSF line detection.

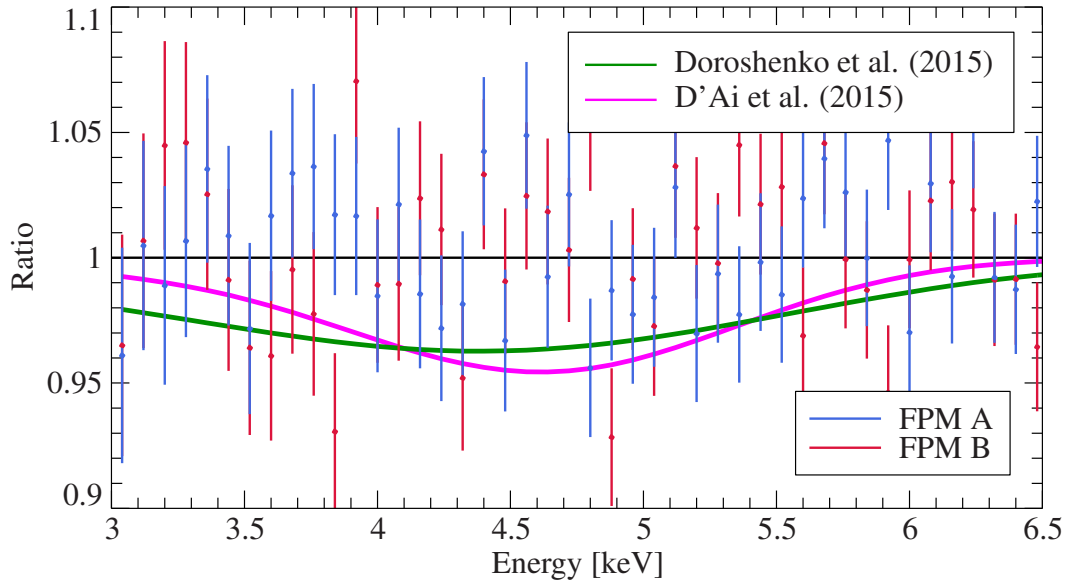

Figure 3.11: Ratio of *NuSTAR* data and fit model without `gabs` as function of energy. Essentially this is a zoom-in into the spectrum as seen in Fig. 3.3. The green and pink lines show the CRSF parameters as claimed in previous reports. Likely a CRSF as claimed would have been seen in these data, however, the S/N-ratio is too low to make a statistically unique statement.

I conclude that the CRSF in the LMXB system GRO J1744−28 is still under debate. It could be possible that the line strength is correlated to the luminosity and that the line vanishes below a certain threshold. My analysis provides an upper limit of 0.07 keV on the strength of a cyclotron line in low-flux state, however, further observations with better S/N-ratio – for instance with the Neutron Star Interior Composition Explorer (*NICER*) – are necessary to solve this puzzle.

Chapter 4

Conclusions

This master's thesis is a synergy of software development and data analysis in the field of X-ray astronomy.

Part I presented the *Upper Limit Servers*. They are a new web-based software tool which enables the production of long-term lightcurves by combining archived data and on-the-fly upper limit estimates. I expanded the software by nine missions in the course of a six month traineeship at ESAC, Madrid. I implemented the footprints, catalog calls, and upper limit calculation for the observatories *Einstein* IPC/HRI, *EXOSAT* LE, *ROSAT* PSPC/HRI as well as the footprints of *XMM-Newton* Slew. The multi-mission approach of the ULS inevitably led to approximations. In order to transform the mission-specific count rate to a flux, the spectral model is approximated with an absorbed power-law or black body by the use of the PIMMS software. Furthermore, I had to account for missing fields in the catalogs, approximate footprint shapes and interpolate vignetting and encircled energy fraction functions. Besides the inclusion of images, I added catalog calls of *Vela 5B*, *Uhuru*, *Ariel V*, *HEAO-1*, *EXOSAT* ME, *GINGA* and *ASCA* GIS/SIS. With the inclusion of these historical catalogs – notably the Fourth Uhuru (4U) and *HEAO-1* Piccinotti Catalog – the ULS are now able to calculate lightcurves as long as 50 years, giving rise to the genuine possibility to detect long-term variability patterns. This becomes especially interesting in the context of the recent launch of *eROSITA*. The inclusion of upper limits to the lightcurve may serve as diagnostic tool to discover new transient X-ray sources. These data can be queried using the HILIGT web interface or a terminal client. Four lightcurves of different astrophysical objects were interpreted to show the scientific possibilities of the ULS. I did not describe the missions *XMM-Newton*, *INTEGRAL*, and *Swift* since their implementation into the ULS is done by the ESAC Science Operation Centre.

Future plans on the ULS are the inclusion of the missions RXTE, *Chandra*, *NuSTAR*, NICER, and *BeppoSAX*. Furthermore, FITS format is planned as download option. Spectral models like APEC and a thermal Bremsstrahlung spectrum are included in PIMMS but so far not in the ULS. On-the-fly computation of the conversion factors would enable the user to specify own output energy ranges.

Part II described the data analysis of the low-mass X-ray binary GRO J1744−28 which went into its fourth outburst in 2017 February (Ch. 3). The ∼29 ks data was taken with the Nuclear Spectroscopic Telescope Array (*NuSTAR*). The source has a luminosity of $3.2 \times 10^{36}\,(D/8\,\mathrm{kpc})^2\,\mathrm{erg\,s^{-1}}$ (3–50 keV) which places the source in sub-critical regime. The low accretion rate is likely the reason for the missing Type II bursts in the lightcurve. I modeled the spectrum with an absorbed cut-off power-law with additional iron line component at ∼6.5 keV. The spectrum is, however, also consistent with a `NPEX`, `FDcut`, or `nthcomp` model. Phase-resolved spectroscopy shows a single peaked pulse profile with no significant energy dependency. Epoch folding yields a pulse period of 0.4670444(6) s, which is consistent with previous measurements. Furthermore, the continuum does not show statistically significant variability. The spectrum does not exhibit a significant cyclotron resonant scattering feature as previously reported (D'Aì et al., 2015; Doroshenko et al., 2015), neither in the phase-averaged nor the phase-resolved spectra. I put a 0.07 keV upper limit on the strength of a CRSF in these data, however, Monte Carlo simulations show that in these low S/N data a 4σ detection limit of 0.15 keV is necessary to make statistically tenable statements about the existence of the line. Because the strengths of previous CRSF reports lie below this limit, I can neither confirm nor deny these claims.

Acknowledgements

Firstly, I would like to thank Thomas Dauser, a dear friend and one of the most inspiring people I've ever met. Without him I wouldn't have changed my research topic to astrophysics. No matter if we do gnarly climbing stuff in the Alps or astrophysics, Tommy always accompanied me with help, knowledge and positiveness. Secondly, I'd like to thank Jörn Wilms for letting me write this master's thesis, for giving advice, helping me with the ESAC trainee application which changed a lot in my research orientation and overall for his relaxed but challenging presence (or non-presence). I'd like to thank each and everyone of the Remeis group for building such a great working atmosphere. In particular, I'd like to thank Ralf Ballhausen who always had an open ear for discussions, my office mates, in particular Basti for sighing every now and then, the pool crew and all cake lovers.

Half a year of this research was done at ESAC in Madrid under the supervision of Richard Saxton, Peter Kretschmar and Felix Fürst. I'd like to thank them for the confidence and time, even if I believe that they felt "traineed-out" every now and then. I'd like to thank Jan-Uwe Ness for inviting me to his garden parties, being a very funny guy and giving best advice and help with future career and PhD possibilities. Furthermore, I'd like to thank Wouter van Reeven for letting me jam with his band and teaching me a lot about observational astronomy. Finally, the ESAC Running club always kept the motivation and sweat production high which I enjoyed a lot.

A main part of my life at ESAC was embossed by the trainees, thank you all for having a great time. In particular I'd like to thank David Otero for numerous analogue photography sessions in Downtown Madrid. Lastly, I thank all the awesome climbers of Madrid who taught me Spanish and included me heart-warmingly into their peer group.

I'd like to thank my mother for accompanying me through all of my life, my brother for being the funniest guy I know, and my dad for teaching me being a carpenter, mechanic, and electrician.

Last, but not least I'd like to thank the ERASMUS+ program and the Remeis Observatory for their financial support. I acknowledge support from the Faculty of the European Space Astronomy Centre (ESAC). This research has made use of ISIS functions (ISISscripts) provided by ECAP/Remeis observatory and MIT (http://www.sternwarte.uni-erlangen.de/isis/).

Bibliography

Abramowitz M., 1965, Handbook of mathematical functions, with formulas, graphs, and mathematical tables, Dover Publications, New York

Akaike H., 1974, IEEE Transactions on Automatic Control 19, 716

Anders E., Grevesse N., 1989, Geochim. Cosmochim. Acta 53, 197

Angelini L., Stella L., Parmar A.N., 1989, ApJ 346, 906

Aoki S., Soma M., Kinoshita H., Inoue K., 1983, A&A 128, 263

Arida M., 1998, ASCA Technical Description, Technical report, Laboratory of High Energy Astrophysics, NASA GSFC, Greenbelt https://heasarc.gsfc.nasa.gov/docs/asca/ao7/appendix_e/ao7_appendix_e.html

Arnaud K., Smith R., Siemiginowska A., 2011, Handbook of X-ray Astronomy, Cambridge University Press

Arnaud K.A., 1996, In: Jacoby G.H., Barnes J. (eds.) Astronomical Data Analysis Software and Systems V, Vol. 101. Astronomical Society of the Pacific Conference Series, p. 17

Aschenbach B., 1988, Appl. Opt. 27, 1404

Asplund M., Grevesse N., Sauval A.J., Scott P., 2009, ARA&A 47, 481

Astropy CollaborationRobitaille T.P., Tollerud E.J., et al., 2013, A&A 558, A33

Augusteijn T., Greiner J., Kouveliotou C., et al., 1997, ApJ 486, 1013

Ayres T.R., Linsky J.L., Vaiana G.S., et al., 1981, ApJ 250, 293

Baade W., Zwicky F., 1934, Proceedings of the National Academy of Science 20, 254

Barragán L., Wilms J., Pottschmidt K., et al., 2009, A&A 508, 1275

Basko M.M., Sunyaev R.A., 1976, MNRAS 175, 395

Becker P.A., Klochkov D., Schönherr G., et al., 2012, A&A 544, A123

Becker P.A., Wolff M.T., 2007, ApJ 654, 435

Belian R.D., Conner J.P., Evans W.D., 1972, ApJL 171, L87

Bhardwaj A., Elsner R.F., Randall Gladstone G., et al., 2007, Planet. Space Sci. 55, 1135

Bhattacharya D., van den Heuvel E.P.J., 1991, Phys. Rep. 203, 1

Blackburn J.K., 1995, In: Shaw R.A., Payne H.E., Hayes J.J.E. (eds.) Astronomical Data Analysis Software and Systems IV, Vol. 77. Astronomical Society of the Pacific Conference Series, p. 367

Bleeker J.A.M., Burger J.J., Deerenberg A.J.M., et al., 1967, ApJ 147, 391

Boller T., Freyberg M.J., Trümper J., et al., 2016, A&A 588, A103

Briel U., Aschenbach B., Hasinger G., et al., (eds.) 1996, ROSAT User's Handbook, Max-Planck-Institut für Extraterrestrische Physik, 85740 Garching bei München, Germany https://heasarc.gsfc.nasa.gov/docs/rosat/ruh/handbook/handbook.html

Caballero I., Kretschmar P., Santangelo A., et al., 2007, A&A 465, L21

Chadwick J., 1932, Nature 129, 312

Coburn W., Heindl W.A., Rothschild R.E., et al., 2002, ApJ 580, 394

Conner J.P., Evans W.D., Belian R.D., 1969, ApJL 157, L157

Corliss W.R., 1971, NASA SOUNDING ROCKETS, 1958-1968, Historical report, National

Aeronautics and Space Administration https://history.nasa.gov/SP-4401.pdf
Cox D., Hinkley D., 1974, Theoretical Statistics, Chapman and Hall
Cui W., 1997, ApJ 482, L163
D'Aì A., Di Salvo T., Iaria R., et al., 2015, MNRAS 449, 4288
D.E. Harris D.I., 1984, Einstein Observatory Revised User's Manual, Technical Report 2, Harvard-Smithonian Center for Astrophysics, https://heasarc.gsfc.nasa.gov/docs/einstein/
de Korte P.A.J., Bleeker J.A.M., den Boggende A.J.F., et al., 1981, SSRv 30, 495
Degenaar N., Miller J.M., Harrison F.A., et al., 2014, ApJL 796, L9
Dennerl K., Burwitz V., Englhauser J., et al., 2002, A&A 386, 319
Doroshenko R., Santangelo A., Doroshenko V., et al., 2015, MNRAS 452, 2490
Doroshenko V., Tsygankov S.S., Mushtukov A.e.A., et al., 2017, MNRAS 466, 2143
Doschek G.A., Feldman U., Kreplin R.W., Cohen L., 1980, ApJ 239, 725
Einstein A., 1916, Annalen der Physik 354, 769
Farinelli R., Ferrigno C., Bozzo E., Becker P.A., 2016, A&A 591, A29
Feigelson E.D., Schreier E.J., Delvaille J.P., et al., 1981, ApJ 251, 31
Ferrigno C., Falanga M., Bozzo E., et al., 2011, A&A 532, A76
Finger M.H., Koh D.T., Nelson R.W., et al., 1996, Nature 381, 291
Forman W., Jones C., Cominsky L., et al., 1978, ApJS 38, 357
Freeman P., Doe S., Siemiginowska A., 2001, In: Starck J.L., Murtagh F.D. (eds.) Astronomical Data Analysis, Vol. 4477. Proc. SPIE., p.76
Fricke W., Schwan H., Lederle T., et al., 1988, Veroeffentlichungen des Astronomischen Rechen-Instituts Heidelberg 32, 1
Friedman H., Lichtman S.W., Byram E.T., 1951, Physical Review 83, 1025
Fürst F., Grefenstette B.W., Staubert R., et al., 2013, ApJ 779, 69
Gabriel C., Denby M., Fyfe D.J., et al., 2004, In: Ochsenbein F., Allen M.G., Egret D. (eds.) Astronomical Data Analysis Software and Systems (ADASS) XIII, Vol. 314. Astronomical Society of the Pacific Conference Series, p. 759
Gendreau K.C., 1995, PhD thesis, MASSACHUSETTS INSTITUTE OF TECHNOLOGY.
Ghosh P., Lamb F.K., 1979a, ApJ 232, 259
Ghosh P., Lamb F.K., 1979b, ApJ 234, 296
Giacconi R., Branduardi G., Briel U., et al., 1979, ApJ 230, 540
Giacconi R., Gursky H., Paolini F.R., Rossi B.B., 1962, Phys. Rev. Lett. 9, 439
Giacconi R., Kellogg E., Gorenstein P., et al., 1971, ApJL 165, L27
Gioia I.M., Maccacaro T., Schild R.E., et al., 1990, ApJS 72, 567
Gladstone G.R., Waite J.H., Grodent D., et al., 2002, Nature 415, 1000
Gold T., 1968, Nature 218, 731
Gorenstein P., Harnden, Jr. F.R., Fabricant D.G., 1981, IEEE Transactions on Nuclear Science 28, 869
Gotthelf E.V., White N.E., 1997, In: Makino F., Mitsuda K. (eds.) X-Ray Imaging and Spectroscopy of Cosmic Hot Plasmas., p. 31
Grindlay J., Gursky H., Schnopper H., et al., 1976, ApJL 205, L127
Grundstrom E.D., Blair J.L., Gies D.R., et al., 2007, ApJ 656, 431
Harding A.K., 2013, Frontiers of Physics 8, 679
Harnden, Jr. F.R., Fabricant D.G., Harris D.E., Schwarz J., 1984, SAO Special Report 393
Harris D.E., 1990, The Einstein Observatory Catalog of IPC X-ray Sources, Smithsonian Institution, Astrophysical Observatory
Harrison F.A., Craig W.W., Christensen F.E., et al., 2013, ApJ 770, 103
Hawley J.F., Gammie C.F., Balbus S.A., 1995, ApJ 440, 742
Hayashida K., Inoue H., Koyama K., et al., 1989, PASJ 41, 373

Heindl W.A., Rothschild R.E., Coburn W., et al., 2004, In: Kaaret P., Lamb F.K., Swank J.H. (eds.) X-ray Timing 2003: Rossi and Beyond, Vol. 714. American Institute of Physics Conference Series, p.323
Heng K., Haberl F., Aschenbach B., Hasinger G., 2008, ApJ 676, 361
Henry J.P., Kellogg E.M., Murray S.S., et al., 1977, In: Chase R.C., Kuswa G.W. (eds.) X-ray imaging, Vol. 106. Society of Photo-Optical Instrumentation Engineers (SPIE) Conference Series, p.196
Hessels J.W.T., Ransom S.M., Stairs I.H., et al., 2006, Science 311, 1901
Hewish A., Bell S.J., Pilkington J.D.H., et al., 1968, Nature 217, 709
Houck J.C., 2002, In: Branduardi-Raymont G. (ed.) High Resolution X-ray Spectroscopy with XMM-Newton and Chandra., p. 17
Iaria R., Di Salvo T., Matranga M., et al., 2015, A&A 577, A63
Jahoda K., Allen J.S., Whitlock L.A., 1994, In: American Astronomical Society Meeting Abstracts, Vol. 26. Bulletin of the American Astronomical Society, p. 1429
Joye W.A., Mandel E., 2003, In: Payne H.E., Jedrzejewski R.I., Hook R.N. (eds.) Astronomical Data Analysis Software and Systems XII, Vol. 295. Astronomical Society of the Pacific Conference Series, p. 489
Katz J.I., 1973, Nature Physical Science 246, 87
Kenneth Seidelmann P., 1992, Explanatory Supplement to the Astronomical Almanac, University Science Books, Mill Valley, California
King A.R., Pounds K.A., 2003, MNRAS 345, 657
Kormendy J., Richstone D., 1995, ARA&A 33, 581
Kouveliotou C., van Paradijs J., Fishman G.J., et al., 1996, Nature 379, 799
Kovalevsky J., Kenneth Seidelmann P., 2004, Fundamentals of Astrometry, Cambridge University Press, Cambridge, UK
Koyama K., Awaki H., Kunieda H., et al., 1989, Nature 339, 603
Kraft R.P., Burrows D.N., Nousek J.A., 1991, ApJ 374, 344
Kreykenbohm I., Wilms J., Kretschmar P., et al., 2008, A&A 492, 511
Kuehnel M., Mueller S., Fuerst F., et al., 2012, In: Proceedings of "An INTEGRAL view of the high-energy sky (the first 10 years)" - 9th INTEGRAL Workshop and celebration of the 10th anniversary of the launch (INTEGRAL 2012). 15-19 October 2012. Bibliotheque Nationale de France., p. 17
Kühnel M., Fürst F., Pottschmidt K., et al., 2017, A&A 607, A88
Kühnel M., Müller S., Kreykenbohm I., et al., 2013, A&A 555, A95
Kuulkers E., in't Zand J.J.M., Lasota J.P., 2009, A&A 503, 889
Landau L.D., Lifshitz E.M., 1965, Quantum mechanics, Oxford: Pergamon Press
Langer S.H., 1981, Phys. Rev. D 23, 328
Lattimer J.M., 2012, Annual Review of Nuclear and Particle Science 62, 485
Leahy D.A., Elsner R.F., Weisskopf M.C., 1983, ApJ 272, 256
Lewin W.H.G., Joss P.C., 1983, In: Lewin W.H.G., van den Heuvel E.P.J. (eds.) Accretion-Driven Stellar X-ray Sources., p. 41
Lewin W.H.G., van Paradijs J., Taam R.E., 1993, SSRv 62, 223
Lisse C.M., Dennerl K., Englhauser J., et al., 1996, Science 274, 205
Lyubarskii Y.E., Syunyaev R.A., 1982, Soviet Astronomy Letters 8, 330
Madsen K.K., Fürst F., Walton D.J., et al., 2015, ApJ 812, 14
Maggi P., Haberl F., Sturm R., Dewey D., 2012, A&A 548, L3
Maitra C., Paul B., Haberl F., Vasilopoulos G., 2018, MNRAS 480, L136
Makino F., ASTRO-C Team 1987, Astro. Lett. and Communications 25, 223
Makishima K., Maejima Y., Mitsuda K., et al., 1986, ApJ 308, 635

Makishima K., Tashiro M., Ebisawa K., et al., 1996, PASJ 48, 171
Marshall N., Warwick R.S., Pounds K.A., 1981, MNRAS 194, 987
Masetti N., D'Avanzo P., Blagorodnova N., Palazzi E., 2014, ATEL 5999
Mathewson D.S., Ford V.L., Dopita M.A., et al., 1983, ApJS 51, 345
McHardy I.M., Lawrence A., Pye J.P., Pounds K.A., 1981, MNRAS 197, 893
Meszaros P., Nagel W., 1985a, ApJ 298, 147
Meszaros P., Nagel W., 1985b, ApJ 299, 138
Mihara T., 1995, PhD thesis, Dept. of Physics, Univ. of Tokyo (M95)
Miller M.C., Lamb F.K., Psaltis D., 1998, ApJ 508, 791
Miller-Jones J.C.A., Bandyopadhyay R.M., Farrell S.A., Gosling A.J., 2007, Monthly Notices of the Royal Astronomical Society 380, 1511
Mirabel I.F., Rodríguez L.F., 1994, Nature 371, 46
Mitsuda K., Inoue H., Koyama K., et al., 1984, PASJ 36, 741
Miyasaka H., 2019, Low energy response calibration and long term gain monitoring of the NuSTAR detectors, Iachec 2019 shonan, Caltech https://indico2.riken.jp/event/2910/contributions/12836/attachments/8527/10368/iachec_miyasaka_2019.pdf
Mukai K., 1993, PIMMS and Viewing: proposal preparation tools, Technical report, NASA GSFC ASCA GOF, Legacy 3, https://heasarc.gsfc.nasa.gov/docs/journal/pimms3.html
Müller S., Ferrigno C., Kühnel M., et al., 2013, A&A 551, A6
Mushtukov A.A., Suleimanov V.F., Tsygankov S.S., Poutanen J., 2015, MNRAS 447, 1847
Neyman J., 1937, Philosophical Transactions of the Royal Society of London Series A 236, 333
Nishiuchi M., Koyama K., Maeda Y., et al., 1999, ApJ 517, 436
Ohashi T., Ebisawa K., Fukazawa Y., et al., 1996, PASJ 48, 157
Orlandini M., Dal Fiume D., Frontera F., et al., 1998, ApJ 500, L163
Pacini F., 1967, Nature 216, 567
Palmeri P., Mendoza C., Kallman T.R., et al., 2003, A&A 410, 359
Peacock A., Andresen R.D., Manzo G., et al., 1981, SSRv 30, 525
Pearson K., 1900, The London, Edinburgh, and Dublin Philosophical Magazine and Journal of Science 50, 157
Pfeffermann E., Briel U.G., Hippmann H., et al., 1987, In: Soft X-ray optics and technology, Vol. 733. Society of Photo-Optical Instrumentation Engineers (SPIE) Conference Series, p. 519
Piccinotti G., Mushotzky R.F., Boldt E.A., et al., 1982, ApJ 253, 485
Pintore F., Sanna A., Riggio A., et al., 2014, ATEL 5901
Postnov K.A., Gornostaev M.I., Klochkov D., et al., 2015, MNRAS 452, 1601
Pounds K., 2002, Philosophical Transactions of the Royal Society of London Series A 360, 1905
Pounds K.A., Allan D.J., Barber C., et al., 1993, MNRAS 260, 77
Pounds K.A., Nandra K., Stewart G.C., et al., 1990, Nature 344, 132
Poutanen J., Mushtukov A.A., Suleimanov V.F., et al., 2013, ApJ 777, 115
Priedhorsky W.C., Terrell J., Holt S.S., 1983, ApJ 270, 233
Protassov R., van Dyk D.A., Connors A., et al., 2002, ApJ 571, 545
Reig P., Belloni T., Israel G.L., et al., 2008, A&A 485, 797
Reiprich T.H., Böhringer H., 2002, ApJ 567, 716
Reynolds A.P., Parmar A.N., Hakala P.J., et al., 1999, A&AS 134, 287
Rosenberg F.D., Eyles C.J., Skinner G.K., Willmore A.P., 1975, Nature 256, 628
Rothschild R., Boldt E., Holt S., et al., 1979, Space Science Instrumentation 4, 269
Santangelo A., Segreto A., Giarrusso S., et al., 1999, ApJ 523, L85
Sasano M., Makishima K., Sakurai S., et al., 2014, Publications of the Astronomical Society of Japan 66, 35
Saxton R.D., Motta S.E., Komossa S., Read A.M., 2015, MNRAS 454, 2798

Schreier E.J., Gorenstein P., Feigelson E.D., 1982, ApJ 261, 42
Schwarm F.W., Ballhausen R., Falkner S., et al., 2017a, A&A 601, A99
Schwarm F.W., Schönherr G., Falkner S., et al., 2017b, A&A 597, A3
Schwarzenberg-Czerny A., 1989, MNRAS 241, 153
Serlemitsos P.J., Jalota L., Soong Y., et al., 1995, PASJ 47, 105
Soldi S., Türler M., Paltani S., et al., 2008, A&A 486, 411
Staubert R., Trümper J., Kendziorra E., et al., 2019, A&A 622, A61
Steiner A.W., Lattimer J.M., Brown E.F., 2013, ApJ 765, L5
Stella L., White N.E., Davelaar J., et al., 1985, ApJ 288, L45
Stoehr F., 2008, Space Telescope European Coordinating Facility Newsletter 45, 7
Tanaka Y., 1986, Observations of Compact X-Ray Sources, Vol. 255, p. 198, LNP Springer-Verlag
Tanaka Y., Inoue H., Holt S.S., 1994, PASJ 46, L37
Troja E., Piro L., van Eerten H., et al., 2017, Nature 551, 71
Trümper J., 1982, Advances in Space Research 2, 241
Trümper J., Kahabka P., Oegelman H., et al., 1986, ApJ 300, L63
Trümper J., Pietsch W., Reppin C., et al., 1978, ApJL 219, L105
Tsusaka Y., Suzuki H., Yamashita K., et al., 1995, Appl. Opt. 34, 4848
Turner E.L., Geller M.J., 1980, ApJ 236, 1
Turner M.J.L., Smith A., Zimmermann H.U., 1981, SSRv 30, 513
Turner M.J.L., Thomas H.D., Patchett B.E., et al., 1989, PASJ 41, 345
Ubertini P., Lebrun F., Di Cocco G., et al., 2003, A&A 411, L131
Ueda Y., Ishisaki Y., Takahashi T., et al., 2001, ApJS 133, 1
Ueda Y., Ishisaki Y., Takahashi T., et al., 2005, ApJS 161, 185
Verner D.A., Ferland G.J., Korista K.T., Yakovlev D.G., 1996, ApJ 465, 487
Wang Y.M., Frank J., 1981, A&A 93, 255
Warwick R.S., Marshall N., Fraser G.W., et al., 1981, MNRAS 197, 865
Wells D.C., Greisen E.W., Harten R.H., 1981, A&AS 44, 363
White N.E., Peacock A., 1988, Mem. S.A.It. 59, 7
Whitlock L., Lochner J., Rhode K., 1992, The Ariel 5 and Vela 5B All-Sky Monitor Databases, Technical report, NASA HEASARC Legacy 2, https://heasarc.gsfc.nasa.gov/docs/journal/ariel2.html
Wilms J., Allen A., McCray R., 2000, ApJ 542, 914
Wilson C.A., Finger M.H., Camero-Arranz A., 2008, ApJ 678, 1263
Winitzki S., 2003, In: Kumar V., Gavrilova M.L., Tan C.J.K., L'Ecuyer P. (eds.) Computational Science and Its Applications — ICCSA 2003., Springer Berlin Heidelberg, Berlin, Heidelberg, p.780
Woods P.M., Kouveliotou C., van Paradijs J., et al., 1999, ApJ 517, 431
Younes G., Kouveliotou C., Grefenstette B.W., et al., 2015, ApJ 804, 43
Zdziarski A.A., Johnson W.N., Magdziarz P., 1996, MNRAS 283, 193
Zel'dovich Y.B., Shakura N.I., 1969, Soviet Astronomy 13, 175
Zimmermann U., Boese G., Becker W., et al., 1998, EXSAS User's Guide, Technical Report 1, Max-Planck-Institut für Extraterrestrische Physik, 85740 Garching bei München, Germany ftp://ftp.xray.mpe.mpg.de/people/mjf/2RXS/exsas_guide-980708.pdf
Zwicky F., 1939, Physical Review 55, 726
Życki P.T., Done C., Smith D.A., 1999, MNRAS 309, 561

Glossary

AGN Active Galactic Nuclei are the cores of galaxies which host a super-massive black hole in their center. They are the most luminous continuously radiating objects in the universe. X-ray spectra of AGN often have a power-law like shape with photon index of about two.

Alfvén radius In the context of accreting X-ray pulsars the Alfvén radius defines the shell where the ram pressure of the gas, acting inwards, and the magnetic pressure, acting outwards, is in equilibrium. At this radius the plasma starts following the magnetic field lines.

ARF The Ancilliary Response File, often also called the "effective area", is commonly used to store the product of *mirror* effective area, filters, and detector efficiency as a function of energy. The detector efficiency is, among other effects, constrained by the quantum efficiency and the filling factor, compensating gaps in the detector surface. The mirror effective area, usually given in cm^2, is given by the multiplication of collection area of the optics and the reflectivity of the mirrors.

Eddington luminosity The Eddington luminosity is defined as the maximum luminosity where radiation pressure and gravitational attraction are in hydrostatic equilibrium. This assumes **spherical** radiation. Some sources do not emit spherically and can exceed this value..

EEF The Encircled Energy Fraction is the fraction of the total (energy) flux that a detectors collects within a given radius. To be specific, it is the flux integrated over the point spread function (PSF, see below) and depends on energy, radius and off-axis angle.

electron configuration In the notation $n\ell^x$, n stands for the principal quantum number, giving the energy level of the electron ($n = 1, 2, 3, ...$). In X-ray astronomy this is sometimes denoted the K-,L-,M-,... shell. Each shell can contain a maximum of $2n^2$ electrons, for instance, $n = 1$ contains two electrons in s-orbital ($1s^2$), $n = 2$ eight electrons ($2s^2\ 2p^6$), $n = 3$ contains 18 electrons ($3s^2\ 3p^6\ 3d^8$), etc. ℓ stands for the angular quantum number giving the shape (or sub-shell) of the orbital (s,p,d,f,g for $\ell = 1, 2, 3, 4, 5$). Finally, x denotes the number of electrons in that orbital. As an example, neutral iron (atomic number $Z = 26$) has the electron configuration

[Ar] $4s^2$ $3d^6$. [Ar] denotes the reference to the last noble gas in the periodic table in order to shorten the notation. The first 18 electrons are in the configuration of argon with six additional electrons on the M-shell ($n = 3$) in d-orbital ($3d^6$) plus two on the N-shell ($n = 4$) in s-orbital ($4s^2$).

FITS The Flexible Image Transport System is a file format widely used in astronomy and developed by the International Astronomical Union (Wells et al., 1981).

FOV The Field of View is the area on the sky from where the telescope receives light and is usually expressed in square degrees. This is not to be mistaken for the spatial resolution of the telescope, which is given by a combination of detector and telescope, whereas the FOV is entirely constrained by the optics.

FWHM The Full Width at Half Maximum is defined as two times the radius at which a symmetric function has decreased to half of its peak value. Note that this is generally a different quantity than the HEW.

HEW The Half Energy Width, also called the Half Power Diameter (HPD) is the diameter of a circle where half of the incident radiation is enclosed. In the context of X-ray telescopes PSFs can be asymmetric. Therefore, the measurable quantity HEW is a better proxy for the resolution of the telescope than the FWHM. For a Gaussian PSF the HEW coincides with the FWHM to the value of $\sigma \cdot 2\sqrt{2 \ln 2}$.

HMXB High-mass X-ray binaries consist of a compact object (neutron star or black hole) and a high-mass star of O or B type. The accretion disk is typically powered by the strong stellar wind of the star or Be-type accretion. HMXBs have larger magnetic fields than LMXBs and are sometimes seen to exhibit cyclotron lines at $E \gtrsim 20\,\mathrm{keV}$.

HPD Half Power Diameter (see HEW).

JD The Julian date is a reference date from the epoch noon (12h) Jan 1, 4713 BC.

lightcurve In X-ray astronomy a lightcurve is a measure of variability of a source. One usually plots the (logarithmic) flux (e.g. in *cgs* units $\mathrm{erg\,cm^{-2}s^{-1}}$) as a function of time. Lightcurves are usually background subtracted where the background consists of detector noise, straylight and cosmic radiation. Lightcurves of variable X-ray sources can exhibit outbursts on the order of minutes to years.

LMXB Low-mass X-ray binary (see Sect. 2.1.2).

MJD The Modified Julian Date equals JD−2400000.5.

orbital parameters In binary systems the star and compact object orbit around the center of mass. This elliptical motion is parameterized by the orbital period P_{orb} (the time for one full orbit), the semi-major axis a, eccentricity $\epsilon = 1 - b/a$, with b the semi-minor axis, i the inclination of the orbital plane to the tangent plane of the sky, τ the time of periastron, when both objects are closest to each other, and ω the longitude of periastron, i.e. the angle between periastron and ascending node (point where the compact object is in tangent plane).

PSF Point sources will never be displayed as exact points in an image. The Point Spread Function describes this response of the optics of the telescope to a point like source. Often this function is radially symmetric and of Gaussian shape. The resulting image is a convolution of PSF and image and results in an Airy disk for Gaussian PSFs. Essentially, the PSF gives the probability to detect a photon as a function of the distance from its original position on the sky (therefore giving the flux at every location in the image). The PSF additionally depends on energy and **off-axis** angle, which is defined as angular distance between the pointing (center of FOV) and the source. The PSF is best (most localized) if the source is in the center of the FOV ("on-axis"), and blurs/smears out if the source is off-axis (i.e. the telescope points to a location next to the source).

quantum efficiency The quantum efficiency of a detector is a probability which determines how likely an impacting photon is absorbed.

ram pressure In the context of X-ray binaries the pressure of the inwards acting gas, located in the accretion disk, is called the ram pressure.

RMF The Redistribution Matrix File is a 2D matrix which assigns a channel to the energy of the impacting photon. In reverse, the RMF assigns an energy range to each channel. Ideally, the RMF is an identity matrix and each measured photon is assigned to its real energy. However, different effects like intrinsic resolution, partial absorption, signal loss, phonons (lattice vibration due to scattering off defects), charge transfer inefficiency, and escape peaks broaden the RMF and results in the fact, that a measured photons energy can deviate from its real energy.

Roche-lobe In a binary system the Roche lobe is the volume in which orbiting matter is gravitationally bound to the star. The apex in the binary system is the point where gravitational and centrifugal forces from the two stars are in equilibrium (also known as the inner Lagrangian point L_1).

SAA The South Atlantic Anomaly is an area of high background radiation. To be specific, the inner van Allen radiation belt comes closer to Earth's surface. Most instruments of a satellite have to be switched off if they pass the SAA to avoid damage.

SAS The Science Analysis System is a set of tasks, scripts and libraries in order to reduce and analyze data taken with the *XMM-Newton* observatory (Gabriel et al., 2004).

spatial resolution The spatial resolution of a telescope is given by the capability to resolve two point sources. Since the PSF broadens point sources and due to diffraction on the aperture of the optics, the theoretical angular resolution of a telescope is given by the Rayleigh criterion $\theta = 1.220 f\lambda/D$ with focal length f, wavelength λ, and lens diameter D.

standardized Standardization, also called the *Standard score*, shifts and re-scales the values according to $(x - < x >)/\sigma_x$ such that they have zero mean and unit variance. Standardization is a particular type of Normalization.

TDB Barycentric Dynamical Time.

UTC Coordinated Universal Time.

vignetting Reduction of brightness towards the periphery of an image (see also: Sect. 1.2.1).

world coordinates In the equatorial coordinate system right ascension and declination (R.A./Dec.) is usually displayed in sexagesimal form. The connection to decimal degrees is:
α [decimal degrees] = Hours $\times$ 15 + Minutes/4 + Seconds/240 (1 hour = 15°)
δ [decimal degrees] = degree + arcmin/60 + arcsec/3600.

Appendix A

Statistics

A.1 χ^2-statistics

The χ^2-test is a statistical hypothesis test under the assumption that the null hypothesis (i.e. the data is independent of a model) is true. The test can be used to reject this null hypothesis under a particular model choice (i.e. the data is not independent under the application of that model). It was first introduced by Pearson (1900) and is nowadays one of the most widely used statistical hypothesis tests. It requires that the test statistic is χ^2-distributed (e.g. Abramowitz, 1965) which means, that the underlying data has to be independent and normally distributed. However, the counts in a bin or pixel in a physical detector are Poisson-distributed. The central limit theorem states, that the Poisson distribution becomes Gaussian at $\gtrsim 20$ counts and χ^2 statistics become applicable. This is the case at a S/N-ratio of ~ 4.5[1].
The value of the test statistic is

$$\chi^2 = \sum_{i=1}^{n} \frac{(D_i - M_i)^2}{\sigma_i^2} \tag{A.1}$$

which asymptotically approaches a χ^2-distribution. D_i are the data points, M_i the expected values from the model, σ_i^2 the variances and n the number of bins.

Reduced χ^2 and degree of freedom Often, the reduced χ^2 value

$$\chi^2_{\text{red.}} = \frac{\chi^2}{\text{dof}} \tag{A.2}$$

is used to quantify the goodness of fit. The degrees of freedom can be calculated by $\text{dof} = n - m$ with n the number of bins as before and p the number of free parameters. Generally speaking, a value of $\chi^2_{\text{red.}} < 1$ indicates over-fitting (fitting of noise) and $\chi^2_{\text{red.}} > 1$ indicates that the fit has not yet fully captured the data, or, that the error variance has been underestimated.

[1] The S/N-ratio scales as square with the number of counts in a bin. For instance, a S/N-ratio of 5 results in 25 counts per bin (neglecting background). This is the case because the Poisson distribution, $P(k) = e^{-\lambda}\lambda^k/k!$, has variance as well as mean equalling λ ($\equiv$ average number of events per interval).

Likelihood-ratio tests The χ^2-test is often used in combination with a likelihood-ratio test. This test can be used to compare the goodness of fit of two statistical models: the null hypothesis against an alternative hypothesis. The value $-2\log\lambda$ with λ the likelihood ratio[2] asymptotically converges to a χ^2-distribution (Wilks' theorem).
This test requires nested models, where nested means that the one model is a subset of the other. In the context of astrophysics this might be a fit model with an additional Gaussian line component (e.g. in order to fit an iron emission line or a CRSF in absorption). As the value $-2\log\lambda$ is approximately χ^2-distributed, one can compare this value to the required significance level (e.g. 2.71 for 90% CL and 1 dof).
Although the likelihood-ratio test is widely used in astrophysics, Protassov et al. (2002) showed that its use must be handled with care and that the application – especially when fitting weak absorption or emission lines – is not allowed[3].
In order to quantify the relative quality of one model with respect to the other one can use the more sophisticated Akaike Information Criterion instead of comparing plain $\Delta\chi^2$-values. This is further explained and applied in Sect. 3.3.2.

Calculating probabilities and $\Delta\chi^2$ values The cumulative probability distribution (i.e. the fraction within the probability distribution) of the χ^2-distribution reduces to an exponential function for two degrees of freedom:

$$P_{\chi^2;\nu=2}(\Delta\chi^2 \leq X) = 1 - e^{-\frac{X}{2}} \tag{A.3}$$

In this case one can easily compute the $\Delta\chi^2$ and probability for a confidence level of interest.

- How to compute $\Delta\chi^2$-values for two degrees of freedom:

$$x\left[\Delta\chi^2\right] = -2\ln(1 - P_{\nu=2}) = -2\ln\left[1 - \mathrm{erf}\left(\frac{\sigma}{2}\right)\right] \tag{A.4}$$

  e.g. $4.61 = -2\log(1-0.9)$ or $11.83 = -2\log\left[1-\mathrm{erf}\left(\frac{3}{2}\right)\right]$ for 3σ and 2 dof

- The p-value gives the fraction **outside** of the probability distribution:

$$p = 1 - \mathrm{erf}\left(\frac{\sigma}{\sqrt{2}}\right) \tag{A.5}$$

  This can be used to compute the number of instances in a sample at a certain significance level by $N = 1/p$ (e.g. 1σ corresponds to 1 in $1 - \mathrm{erf}(1/\sqrt{2}) = 3.15$ cases).

[2]The likelihood ratio $\lambda(x) = \frac{\sup\{\mathcal{L}(\theta|x):\theta\in\Theta_0\}}{\sup\{\mathcal{L}(\theta|x):\theta\in\Theta\}}$ with null hypothesis $H_0 : \theta \in \Theta_0$ and alternative hypothesis $H_1 = \theta \in \Theta\backslash\Theta_0$ expresses how likely the data is under one or the other model.

[3]The likelihood-ratio test does not adhere to its nominal χ^2-distribution if the parameter space is not an open set. In other words it cannot be used if the parameter lies on the boundary of the parameter space. This, however, is often common, for instance, when fitting a Gaussian line with positive area. If the spectral parameter is tested at the boundary (zero in this case), $-2\log\lambda$ will not adhere to a χ^2-distribution. This is especially precarious for very weak signatures in the data. (Protassov et al., 2002)

- How to compute a significance from a probability:

$$\sigma = \sqrt{2}\,\mathrm{erf}^{-1}(1-p) \tag{A.6}$$

  e.g. $1\,[\sigma] = \sqrt{2}\mathrm{erf}^{-1}(0.683)$. Inverse error function can be numerically approximated e.g. according to Winitzki (2003).

A.2 Akaike Information Criterion

The Akaike Information Criterion is a statistical test which estimates the improvement of one model with respect to the other (Akaike, 1974). For small sample sizes it is computed by

$$\mathrm{AIC} \;=\; \chi^2 + 2k + \frac{2k^2+2k}{n-k-1} \tag{A.7}$$

with $\chi^2 = -2\log\hat{L}$, $\hat{L}$ the likelihood of the fit, k the number of free parameters and n the total number of bins ($n-k = \#\mathrm{dof}$).
Given a set of models, the one with the minimal AIC value is the preferred one. The $+2k$ summand therefore induces a penalty on the number of free parameters and thus avoids overfitting (increasing the number of free parameters almost always improves the goodness of fit). At the same time the χ-value of the fit should be as small as possible (maximum likelihood). In practice one computes the difference in AIC, similar to the difference in $\Delta\chi^2$. Large differences result in statistically significant improvements of the test model. In order to quantify this, one computes the so-called *Chance Improvement Probability* (CIP) by exponentiating the deviation in AIC of the models with and without test parameter:

$$\mathrm{CIP} \;=\; e^{-\frac{1}{2}\Delta\mathrm{AIC}} \tag{A.8}$$

This probability value indicates how likely the improvement one deduces from the new model is only due to random effects. In order to calculate $\Delta\chi^2$ significance thresholds from the AIC, one can solve Eq. A.7 and Eq. A.8 for $\chi_2^2 - \chi_1^2$ which yields

$$\Delta\chi^2 \;=\; -2\ln\mathrm{CIP} - 2(p_2-p_1) - \frac{2p_2(p_2+1)}{n_2-p_2-1} + \frac{2p_1(p_1+1)}{n_1-p_1-1} \quad . \tag{A.9}$$

A.3 What is an upper limit?

An upper limit constrains the true (unknown) parameter of interest to be below this threshold within a given confidence level. This concept was first introduced by Neyman (1937) and is described in the mathematics of statistical interference, to be specific in interval estimation. The stringent mathematical formalism can be found in e.g. Cox & Hinkley (1974, p.49, p.208ff).
A confidence interval is an interval estimate which constrains the given data point under the applied statistics. Let X be a random sample from a probability distribution $Pr(X)$

with θ the parameter of interest. Let further $1-p$ be a value between 0 and 1 (usually close to one). Then the confidence interval of θ at confidence level $1-p$ is given by

$$Pr(u(X) < \theta < v(x)) = 1 - p \quad \forall\, \theta \qquad . \tag{A.10}$$

$u(x)$ and $v(x)$ are called the $1-p$ lower and upper confidence limit of the confidence interval. In other words, the confidence interval $(u(X), v(X))$ contains the parameter of interest θ with probability $1-p$.
As an example a confidence level of 90% means that in 9 out of 10 cases the (unknown) parameter lies within the confidence interval. In the context of Gaussian statistics, confidence levels are usually given at the 1σ (68.3%), 90%, or 95% level. Is it important to mention that in most plots the confidence interval does **not** equal the error bars (these are often standard errors or standard deviations).

Appendix B

ULS tables

ROSAT PSPC Pointed Encircled Energy Fraction (Zimmermann et al., 1998, Eq. 5.13):

$$r_1(E) = \frac{39.95}{E} \tag{B.1}$$

$$r_2(E) = \frac{861.9}{E} \tag{B.2}$$

$$R(E) = \sqrt{50.61E^{-1.472} + 6.8E^{5.62}} \tag{B.3}$$

$$\alpha(E) = 2.119 + 0.212E \tag{B.4}$$

$$\sigma(E,\epsilon) = \sqrt{108.7E^{-0.888} + 1.121E^{6} + 0.219\epsilon^{2.848}} \tag{B.5}$$

$$p_3(E) = 0.075E^{1.43} \tag{B.6}$$

$$p_2(E,\epsilon) = \min\left\{10^{0.639E+0.052E^2-1.635}\cdot e^{-\left(\frac{\epsilon}{12}\right)^2/2}, 1-p_3(E)\right\} \tag{B.7}$$

$$p_1(E,\epsilon) = 1 - p_3(E) - p_2(E,\epsilon) \tag{B.8}$$

$$M(E) = \frac{1}{\frac{1}{2}\ln\left[1+\left(\frac{r_2}{r_1}\right)^2\right] + \frac{1}{[\alpha(E)-2]\left[1+\left(\frac{r_1}{r_2}\right)^2\right]}} \tag{B.9}$$

$$M(r,E) = M(E)\cdot\begin{cases}\frac{1}{2}\ln\left[1+\left(\frac{r}{r_1(E)}\right)^2\right], & r \le r_2(E),\\ \frac{1}{2}\ln\left[1+\left(\frac{r_2}{r_1}\right)^2\right] + \frac{1-\left(\frac{r}{r_2(E)}\right)^{\alpha(E)-2}}{[\alpha(E)-2]\left[1+\left(\frac{r_1}{r_2}\right)^2\right]} & r > r_2(E)\end{cases} \tag{B.10}$$

$$EEF(r,E,\epsilon) = p_1(E,\epsilon)\cdot\left[1-e^{-\frac{1}{2}\left(\frac{r}{\sigma(E,\epsilon)}\right)^2}\right] + p_2(E,\epsilon)\cdot\left[1-e^{-\frac{r}{R(E)}}\right] + p_3(E)\cdot M(r,E) \tag{B.11}$$

Table B.1: *ROSAT* HRI call to the HEASARC catalog ROSHRI for sky position R.A.=187.2779, Dec.=2.052 (quasar 3C 273) with a cone search radius of 1′.

https://heasarc.gsfc.nasa.gov/db-perl/W3Browse/w3query.pl?tablehead=name%3dBATCHRETRIEVALCATALOG+roshri&Action=Query&Coordinates=Equatorial+RA+Dec&Equinox=2000&Radius=1.0&Fields=Begin_Date,End_Date,Count_Rate,Count_Rate_Error,Exposure,Box_Cts,Cir_Bkg,SeqID&Entry=187.2779,2.052&displaymode=BatchDisplay

Table B.2: Pixel positions of the two octagonal *EXOSAT* LE footprint shapes. The image has a size of 2048x2048 pixels.

Shape	Pixel position of the footprint (x/y)					Percentage
Octagonal CMA1	124/902	149/1278	921/2048	1181/2013	1479/2037	81.1%
(Fig. 1.12a)	2048/1464	2048/773	1435/226	886/112		
Octagonal CMA2	1/512	1/1427	590/2048	1452/2048		10.9%
(Fig. 1.12b)	2048/1520	2048/547	1530/1	537/1		

Table B.3: Conversion factors

Mission	Filter	Model	Index	N_H (cm^{-2})	CF soft	CF hard	CF total
EXOSAT-LE	3Lx	plaw	1.5	$1.0 \cdot 10^{20}$	$2.845 \cdot 10^{-10}$	–	–
EXOSAT-LE	3Lx	plaw	2.0	$1.0 \cdot 10^{20}$	$1.808 \cdot 10^{-10}$	–	–
EXOSAT-LE	3Lx	plaw	2.5	$1.0 \cdot 10^{20}$	$1.165 \cdot 10^{-10}$	–	–
EXOSAT-LE	3Lx	plaw	3.0	$1.0 \cdot 10^{20}$	$7.777 \cdot 10^{-11}$	–	–
EXOSAT-LE	3Lx	plaw	3.5	$1.0 \cdot 10^{20}$	$5.407 \cdot 10^{-11}$	–	–
EXOSAT-LE	3Lx	plaw	1.5	$3.0 \cdot 10^{20}$	$4.812 \cdot 10^{-10}$	–	–
EXOSAT-LE	3Lx	plaw	2.0	$3.0 \cdot 10^{20}$	$3.566 \cdot 10^{-10}$	–	–
EXOSAT-LE	3Lx	plaw	2.5	$3.0 \cdot 10^{20}$	$2.642 \cdot 10^{-10}$	–	–
EXOSAT-LE	3Lx	plaw	3.0	$3.0 \cdot 10^{20}$	$1.988 \cdot 10^{-10}$	–	–
EXOSAT-LE	3Lx	plaw	3.5	$3.0 \cdot 10^{20}$	$1.533 \cdot 10^{-10}$	–	–
EXOSAT-LE	3Lx	plaw	1.5	$1.0 \cdot 10^{21}$	$7.460 \cdot 10^{-10}$	–	–
EXOSAT-LE	3Lx	plaw	2.0	$1.0 \cdot 10^{21}$	$6.221 \cdot 10^{-10}$	–	–
EXOSAT-LE	3Lx	plaw	2.5	$1.0 \cdot 10^{21}$	$5.186 \cdot 10^{-10}$	–	–
EXOSAT-LE	3Lx	plaw	3.0	$1.0 \cdot 10^{21}$	$4.356 \cdot 10^{-10}$	–	–
EXOSAT-LE	3Lx	plaw	3.5	$1.0 \cdot 10^{21}$	$3.708 \cdot 10^{-10}$	–	–
EXOSAT-LE	3Lx	plaw	1.7	$1.0 \cdot 10^{20}$	$2.374 \cdot 10^{-10}$	–	–
EXOSAT-LE	3Lx	plaw	1.7	$3.0 \cdot 10^{20}$	$4.274 \cdot 10^{-10}$	–	–
EXOSAT-LE	3Lx	plaw	1.7	$1.0 \cdot 10^{21}$	$6.942 \cdot 10^{-10}$	–	–
EXOSAT-LE	3Lx	plaw	0.5	$1.0 \cdot 10^{20}$	$6.409 \cdot 10^{-10}$	–	–
EXOSAT-LE	3Lx	plaw	1.0	$1.0 \cdot 10^{20}$	$4.387 \cdot 10^{-10}$	–	–
EXOSAT-LE	3Lx	plaw	0.5	$3.0 \cdot 10^{20}$	$8.180 \cdot 10^{-10}$	–	–
EXOSAT-LE	3Lx	plaw	1.0	$3.0 \cdot 10^{20}$	$6.376 \cdot 10^{-10}$	–	–
EXOSAT-LE	3Lx	plaw	0.5	$1.0 \cdot 10^{21}$	$1.040 \cdot 10^{-9}$	–	–
EXOSAT-LE	3Lx	plaw	1.0	$1.0 \cdot 10^{21}$	$8.873 \cdot 10^{-10}$	–	–
EXOSAT-LE	3Lx	bbody	0.06	$1.0 \cdot 10^{20}$	$6.668 \cdot 10^{-11}$	–	–
EXOSAT-LE	3Lx	bbody	0.10	$1.0 \cdot 10^{20}$	$1.399 \cdot 10^{-10}$	–	–
EXOSAT-LE	3Lx	bbody	0.30	$1.0 \cdot 10^{20}$	$5.386 \cdot 10^{-10}$	–	–
EXOSAT-LE	3Lx	bbody	1.00	$1.0 \cdot 10^{20}$	$1.073 \cdot 10^{-9}$	–	–
EXOSAT-LE	3Lx	bbody	0.06	$3.0 \cdot 10^{20}$	$1.252 \cdot 10^{-10}$	–	–
EXOSAT-LE	3Lx	bbody	0.10	$3.0 \cdot 10^{20}$	$2.159 \cdot 10^{-10}$	–	–
EXOSAT-LE	3Lx	bbody	0.30	$3.0 \cdot 10^{20}$	$6.330 \cdot 10^{-10}$	–	–
EXOSAT-LE	3Lx	bbody	1.00	$3.0 \cdot 10^{20}$	$1.156 \cdot 10^{-9}$	–	–
EXOSAT-LE	3Lx	bbody	0.06	$1.0 \cdot 10^{21}$	$2.331 \cdot 10^{-10}$	–	–
EXOSAT-LE	3Lx	bbody	0.10	$1.0 \cdot 10^{21}$	$3.167 \cdot 10^{-10}$	–	–
EXOSAT-LE	3Lx	bbody	0.30	$1.0 \cdot 10^{21}$	$7.734 \cdot 10^{-10}$	–	–
EXOSAT-LE	3Lx	bbody	1.00	$1.0 \cdot 10^{21}$	$1.295 \cdot 10^{-9}$	–	–
EXOSAT-LE	4LX	plaw	1.5	$1.0 \cdot 10^{20}$	$3.252 \cdot 10^{-10}$	–	–
EXOSAT-LE	4LX	plaw	2.0	$1.0 \cdot 10^{20}$	$2.079 \cdot 10^{-10}$	–	–
EXOSAT-LE	4LX	plaw	2.5	$1.0 \cdot 10^{20}$	$1.344 \cdot 10^{-10}$	–	–
EXOSAT-LE	4LX	plaw	3.0	$1.0 \cdot 10^{20}$	$8.992 \cdot 10^{-11}$	–	–
EXOSAT-LE	4LX	plaw	3.5	$1.0 \cdot 10^{20}$	$6.270 \cdot 10^{-11}$	–	–
EXOSAT-LE	4LX	plaw	1.5	$3.0 \cdot 10^{20}$	$5.477 \cdot 10^{-10}$	–	–
EXOSAT-LE	4LX	plaw	2.0	$3.0 \cdot 10^{20}$	$4.105 \cdot 10^{-10}$	–	–
EXOSAT-LE	4LX	plaw	2.5	$3.0 \cdot 10^{20}$	$3.056 \cdot 10^{-10}$	–	–
EXOSAT-LE	4LX	plaw	3.0	$3.0 \cdot 10^{20}$	$2.298 \cdot 10^{-10}$	–	–
EXOSAT-LE	4LX	plaw	3.5	$3.0 \cdot 10^{20}$	$1.765 \cdot 10^{-10}$	–	–
EXOSAT-LE	4LX	plaw	1.5	$1.0 \cdot 10^{21}$	$8.264 \cdot 10^{-10}$	–	–
EXOSAT-LE	4LX	plaw	2.0	$1.0 \cdot 10^{21}$	$7.027 \cdot 10^{-10}$	–	–
EXOSAT-LE	4LX	plaw	2.5	$1.0 \cdot 10^{21}$	$5.972 \cdot 10^{-10}$	–	–
EXOSAT-LE	4LX	plaw	3.0	$1.0 \cdot 10^{21}$	$5.105 \cdot 10^{-10}$	–	–
EXOSAT-LE	4LX	plaw	3.5	$1.0 \cdot 10^{21}$	$4.411 \cdot 10^{-10}$	–	–
EXOSAT-LE	4LX	plaw	1.7	$1.0 \cdot 10^{20}$	$2.721 \cdot 10^{-10}$	–	–
EXOSAT-LE	4LX	plaw	1.7	$3.0 \cdot 10^{20}$	$4.890 \cdot 10^{-10}$	–	–
EXOSAT-LE	4LX	plaw	1.7	$1.0 \cdot 10^{21}$	$7.749 \cdot 10^{-10}$	–	–
EXOSAT-LE	4LX	plaw	0.5	$1.0 \cdot 10^{20}$	$7.118 \cdot 10^{-10}$	–	–

EXOSAT-LE	4LX	plaw	1.0	$1.0 \cdot 10^{20}$	$4.957 \cdot 10^{-10}$	–	–
EXOSAT-LE	4LX	plaw	0.5	$3.0 \cdot 10^{20}$	$8.981 \cdot 10^{-10}$	–	–
EXOSAT-LE	4LX	plaw	1.0	$3.0 \cdot 10^{20}$	$7.138 \cdot 10^{-10}$	–	–
EXOSAT-LE	4LX	plaw	0.5	$1.0 \cdot 10^{21}$	$1.113 \cdot 10^{-9}$	–	–
EXOSAT-LE	4LX	plaw	1.0	$1.0 \cdot 10^{21}$	$9.650 \cdot 10^{-10}$	–	–
EXOSAT-LE	4LX	bbody	0.06	$1.0 \cdot 10^{20}$	$7.641 \cdot 10^{-11}$	–	–
EXOSAT-LE	4LX	bbody	0.10	$1.0 \cdot 10^{20}$	$1.635 \cdot 10^{-10}$	–	–
EXOSAT-LE	4LX	bbody	0.30	$1.0 \cdot 10^{20}$	$6.040 \cdot 10^{-10}$	–	–
EXOSAT-LE	4LX	bbody	1.00	$1.0 \cdot 10^{20}$	$1.146 \cdot 10^{-9}$	–	–
EXOSAT-LE	4LX	bbody	0.06	$3.0 \cdot 10^{20}$	$1.463 \cdot 10^{-10}$	–	–
EXOSAT-LE	4LX	bbody	0.10	$3.0 \cdot 10^{20}$	$2.583 \cdot 10^{-10}$	–	–
EXOSAT-LE	4LX	bbody	0.30	$3.0 \cdot 10^{20}$	$7.042 \cdot 10^{-10}$	–	–
EXOSAT-LE	4LX	bbody	1.00	$3.0 \cdot 10^{20}$	$1.225 \cdot 10^{-9}$	–	–
EXOSAT-LE	4LX	bbody	0.06	$1.0 \cdot 10^{21}$	$2.928 \cdot 10^{-10}$	–	–
EXOSAT-LE	4LX	bbody	0.10	$1.0 \cdot 10^{21}$	$3.823 \cdot 10^{-10}$	–	–
EXOSAT-LE	4LX	bbody	0.30	$1.0 \cdot 10^{21}$	$8.401 \cdot 10^{-10}$	–	–
EXOSAT-LE	4LX	bbody	1.00	$1.0 \cdot 10^{21}$	$1.353 \cdot 10^{-9}$	–	–
EXOSAT-LE	Al/P	plaw	1.5	$1.0 \cdot 10^{20}$	$6.054 \cdot 10^{-10}$	–	–
EXOSAT-LE	Al/P	plaw	2.0	$1.0 \cdot 10^{20}$	$4.608 \cdot 10^{-10}$	–	–
EXOSAT-LE	Al/P	plaw	2.5	$1.0 \cdot 10^{20}$	$3.554 \cdot 10^{-10}$	–	–
EXOSAT-LE	Al/P	plaw	3.0	$1.0 \cdot 10^{20}$	$2.806 \cdot 10^{-10}$	–	–
EXOSAT-LE	Al/P	plaw	3.5	$1.0 \cdot 10^{20}$	$2.268 \cdot 10^{-10}$	–	–
EXOSAT-LE	Al/P	plaw	1.5	$3.0 \cdot 10^{20}$	$7.442 \cdot 10^{-10}$	–	–
EXOSAT-LE	Al/P	plaw	2.0	$3.0 \cdot 10^{20}$	$5.994 \cdot 10^{-10}$	–	–
EXOSAT-LE	Al/P	plaw	2.5	$3.0 \cdot 10^{20}$	$4.896 \cdot 10^{-10}$	–	–
EXOSAT-LE	Al/P	plaw	3.0	$3.0 \cdot 10^{20}$	$4.093 \cdot 10^{-10}$	–	–
EXOSAT-LE	Al/P	plaw	3.5	$3.0 \cdot 10^{20}$	$3.512 \cdot 10^{-10}$	–	–
EXOSAT-LE	Al/P	plaw	1.5	$1.0 \cdot 10^{21}$	$9.843 \cdot 10^{-10}$	–	–
EXOSAT-LE	Al/P	plaw	2.0	$1.0 \cdot 10^{21}$	$8.275 \cdot 10^{-10}$	–	–
EXOSAT-LE	Al/P	plaw	2.5	$1.0 \cdot 10^{21}$	$6.990 \cdot 10^{-10}$	–	–
EXOSAT-LE	Al/P	plaw	3.0	$1.0 \cdot 10^{21}$	$5.982 \cdot 10^{-10}$	–	–
EXOSAT-LE	Al/P	plaw	3.5	$1.0 \cdot 10^{21}$	$5.216 \cdot 10^{-10}$	–	–
EXOSAT-LE	Al/P	plaw	1.7	$1.0 \cdot 10^{20}$	$5.424 \cdot 10^{-10}$	–	–
EXOSAT-LE	Al/P	plaw	1.7	$3.0 \cdot 10^{20}$	$6.819 \cdot 10^{-10}$	–	–
EXOSAT-LE	Al/P	plaw	1.7	$1.0 \cdot 10^{21}$	$9.182 \cdot 10^{-10}$	–	–
EXOSAT-LE	Al/P	plaw	0.5	$1.0 \cdot 10^{20}$	$1.019 \cdot 10^{-9}$	–	–
EXOSAT-LE	Al/P	plaw	1.0	$1.0 \cdot 10^{20}$	$7.931 \cdot 10^{-10}$	–	–
EXOSAT-LE	Al/P	plaw	0.5	$3.0 \cdot 10^{20}$	$1.137 \cdot 10^{-9}$	–	–
EXOSAT-LE	Al/P	plaw	1.0	$3.0 \cdot 10^{20}$	$9.252 \cdot 10^{-10}$	–	–
EXOSAT-LE	Al/P	plaw	0.5	$1.0 \cdot 10^{21}$	$1.368 \cdot 10^{-9}$	–	–
EXOSAT-LE	Al/P	plaw	1.0	$1.0 \cdot 10^{21}$	$1.167 \cdot 10^{-9}$	–	–
EXOSAT-LE	Al/P	bbody	0.06	$1.0 \cdot 10^{20}$	$2.272 \cdot 10^{-10}$	–	–
EXOSAT-LE	Al/P	bbody	0.10	$1.0 \cdot 10^{20}$	$3.202 \cdot 10^{-10}$	–	–
EXOSAT-LE	Al/P	bbody	0.30	$1.0 \cdot 10^{20}$	$7.905 \cdot 10^{-10}$	–	–
EXOSAT-LE	Al/P	bbody	1.00	$1.0 \cdot 10^{20}$	$1.470 \cdot 10^{-9}$	–	–
EXOSAT-LE	Al/P	bbody	0.06	$3.0 \cdot 10^{20}$	$2.874 \cdot 10^{-10}$	–	–
EXOSAT-LE	Al/P	bbody	0.10	$3.0 \cdot 10^{20}$	$3.678 \cdot 10^{-10}$	–	–
EXOSAT-LE	Al/P	bbody	0.30	$3.0 \cdot 10^{20}$	$8.558 \cdot 10^{-10}$	–	–
EXOSAT-LE	Al/P	bbody	1.00	$3.0 \cdot 10^{20}$	$1.541 \cdot 10^{-9}$	–	–
EXOSAT-LE	Al/P	bbody	0.06	$1.0 \cdot 10^{21}$	$3.487 \cdot 10^{-10}$	–	–
EXOSAT-LE	Al/P	bbody	0.10	$1.0 \cdot 10^{21}$	$4.291 \cdot 10^{-10}$	–	–
EXOSAT-LE	Al/P	bbody	0.30	$1.0 \cdot 10^{21}$	$1.004 \cdot 10^{-9}$	–	–
EXOSAT-LE	Al/P	bbody	1.00	$1.0 \cdot 10^{21}$	$1.712 \cdot 10^{-9}$	–	–
EXOSAT-LE	Bor	plaw	1.5	$1.0 \cdot 10^{20}$	$1.823 \cdot 10^{-9}$	–	–
EXOSAT-LE	Bor	plaw	2.0	$1.0 \cdot 10^{20}$	$1.691 \cdot 10^{-9}$	–	–
EXOSAT-LE	Bor	plaw	2.5	$1.0 \cdot 10^{20}$	$1.443 \cdot 10^{-9}$	–	–
EXOSAT-LE	Bor	plaw	3.0	$1.0 \cdot 10^{20}$	$1.126 \cdot 10^{-9}$	–	–
EXOSAT-LE	Bor	plaw	3.5	$1.0 \cdot 10^{20}$	$8.300 \cdot 10^{-10}$	–	–
EXOSAT-LE	Bor	plaw	1.5	$3.0 \cdot 10^{20}$	$1.984 \cdot 10^{-9}$	–	–
EXOSAT-LE	Bor	plaw	2.0	$3.0 \cdot 10^{20}$	$2.105 \cdot 10^{-9}$	–	–
EXOSAT-LE	Bor	plaw	2.5	$3.0 \cdot 10^{20}$	$2.292 \cdot 10^{-9}$	–	–
EXOSAT-LE	Bor	plaw	3.0	$3.0 \cdot 10^{20}$	$2.510 \cdot 10^{-9}$	–	–
EXOSAT-LE	Bor	plaw	3.5	$3.0 \cdot 10^{20}$	$2.673 \cdot 10^{-9}$	–	–
EXOSAT-LE	Bor	plaw	1.5	$1.0 \cdot 10^{21}$	$1.840 \cdot 10^{-9}$	–	–
EXOSAT-LE	Bor	plaw	2.0	$1.0 \cdot 10^{21}$	$1.863 \cdot 10^{-9}$	–	–
EXOSAT-LE	Bor	plaw	2.5	$1.0 \cdot 10^{21}$	$1.933 \cdot 10^{-9}$	–	–
EXOSAT-LE	Bor	plaw	3.0	$1.0 \cdot 10^{21}$	$2.065 \cdot 10^{-9}$	–	–
EXOSAT-LE	Bor	plaw	3.5	$1.0 \cdot 10^{21}$	$2.273 \cdot 10^{-9}$	–	–
EXOSAT-LE	Bor	plaw	0.5	$1.0 \cdot 10^{20}$	$1.906 \cdot 10^{-9}$	–	–
EXOSAT-LE	Bor	plaw	1.0	$1.0 \cdot 10^{20}$	$1.876 \cdot 10^{-9}$	–	–
EXOSAT-LE	Bor	plaw	0.5	$3.0 \cdot 10^{20}$	$1.921 \cdot 10^{-9}$	–	–
EXOSAT-LE	Bor	plaw	1.0	$3.0 \cdot 10^{20}$	$1.927 \cdot 10^{-9}$	–	–
EXOSAT-LE	Bor	plaw	0.5	$1.0 \cdot 10^{21}$	$1.893 \cdot 10^{-9}$	–	–
EXOSAT-LE	Bor	plaw	1.0	$1.0 \cdot 10^{21}$	$1.854 \cdot 10^{-9}$	–	–

EXOSAT-LE	Bor	bbody	0.06	$1.0 \cdot 10^{20}$	$1.512 \cdot 10^{-9}$	–	–
EXOSAT-LE	Bor	bbody	0.10	$1.0 \cdot 10^{20}$	$2.636 \cdot 10^{-9}$	–	–
EXOSAT-LE	Bor	bbody	0.30	$1.0 \cdot 10^{20}$	$1.754 \cdot 10^{-9}$	–	–
EXOSAT-LE	Bor	bbody	1.00	$1.0 \cdot 10^{20}$	$1.946 \cdot 10^{-9}$	–	–
EXOSAT-LE	Bor	bbody	0.06	$3.0 \cdot 10^{20}$	$5.927 \cdot 10^{-9}$	–	–
EXOSAT-LE	Bor	bbody	0.10	$3.0 \cdot 10^{20}$	$3.506 \cdot 10^{-9}$	–	–
EXOSAT-LE	Bor	bbody	0.30	$3.0 \cdot 10^{20}$	$1.735 \cdot 10^{-9}$	–	–
EXOSAT-LE	Bor	bbody	1.00	$3.0 \cdot 10^{20}$	$1.949 \cdot 10^{-9}$	–	–
EXOSAT-LE	Bor	bbody	0.06	$1.0 \cdot 10^{21}$	$5.616 \cdot 10^{-9}$	–	–
EXOSAT-LE	Bor	bbody	0.10	$1.0 \cdot 10^{21}$	$2.614 \cdot 10^{-9}$	–	–
EXOSAT-LE	Bor	bbody	0.30	$1.0 \cdot 10^{21}$	$1.674 \cdot 10^{-9}$	–	–
EXOSAT-LE	Bor	bbody	1.00	$1.0 \cdot 10^{21}$	$1.964 \cdot 10^{-9}$	–	–
EXOSAT-ME	–	plaw	1.5	$1.0 \cdot 10^{20}$	–	$1.550 \cdot 10^{-11}$	–
EXOSAT-ME	–	plaw	2.0	$1.0 \cdot 10^{20}$	–	$1.300 \cdot 10^{-11}$	–
EXOSAT-ME	–	plaw	2.5	$1.0 \cdot 10^{20}$	–	$1.094 \cdot 10^{-11}$	–
EXOSAT-ME	–	plaw	3.0	$1.0 \cdot 10^{20}$	–	$9.262 \cdot 10^{-12}$	–
EXOSAT-ME	–	plaw	3.5	$1.0 \cdot 10^{20}$	–	$7.892 \cdot 10^{-12}$	–
EXOSAT-ME	–	plaw	1.5	$3.0 \cdot 10^{20}$	–	$1.553 \cdot 10^{-11}$	–
EXOSAT-ME	–	plaw	2.0	$3.0 \cdot 10^{20}$	–	$1.303 \cdot 10^{-11}$	–
EXOSAT-ME	–	plaw	2.5	$3.0 \cdot 10^{20}$	–	$1.097 \cdot 10^{-11}$	–
EXOSAT-ME	–	plaw	3.0	$3.0 \cdot 10^{20}$	–	$9.294 \cdot 10^{-12}$	–
EXOSAT-ME	–	plaw	3.5	$3.0 \cdot 10^{20}$	–	$7.925 \cdot 10^{-12}$	–
EXOSAT-ME	–	plaw	1.5	$1.0 \cdot 10^{21}$	–	$1.562 \cdot 10^{-11}$	–
EXOSAT-ME	–	plaw	2.0	$1.0 \cdot 10^{21}$	–	$1.313 \cdot 10^{-11}$	–
EXOSAT-ME	–	plaw	2.5	$1.0 \cdot 10^{21}$	–	$1.108 \cdot 10^{-11}$	–
EXOSAT-ME	–	plaw	3.0	$1.0 \cdot 10^{21}$	–	$9.404 \cdot 10^{-12}$	–
EXOSAT-ME	–	plaw	3.5	$1.0 \cdot 10^{21}$	–	$8.038 \cdot 10^{-12}$	–
EXOSAT-ME	–	plaw	1.7	$1.0 \cdot 10^{20}$	–	$1.445 \cdot 10^{-11}$	–
EXOSAT-ME	–	plaw	1.7	$3.0 \cdot 10^{20}$	–	$1.448 \cdot 10^{-11}$	–
EXOSAT-ME	–	plaw	1.7	$1.0 \cdot 10^{21}$	–	$1.457 \cdot 10^{-11}$	–
EXOSAT-ME	–	plaw	0.5	$1.0 \cdot 10^{20}$	–	$2.152 \cdot 10^{-11}$	–
EXOSAT-ME	–	plaw	1.0	$1.0 \cdot 10^{20}$	–	$1.840 \cdot 10^{-11}$	–
EXOSAT-ME	–	plaw	0.5	$3.0 \cdot 10^{20}$	–	$2.154 \cdot 10^{-11}$	–
EXOSAT-ME	–	plaw	1.0	$3.0 \cdot 10^{20}$	–	$1.842 \cdot 10^{-11}$	–
EXOSAT-ME	–	plaw	0.5	$1.0 \cdot 10^{21}$	–	$2.162 \cdot 10^{-11}$	–
EXOSAT-ME	–	plaw	1.0	$1.0 \cdot 10^{21}$	–	$1.851 \cdot 10^{-11}$	–
EXOSAT-ME	–	bbody	0.06	$1.0 \cdot 10^{20}$	–	$1.599 \cdot 10^{-16}$	–
EXOSAT-ME	–	bbody	0.10	$1.0 \cdot 10^{20}$	–	$6.564 \cdot 10^{-14}$	–
EXOSAT-ME	–	bbody	0.30	$1.0 \cdot 10^{20}$	–	$4.717 \cdot 10^{-12}$	–
EXOSAT-ME	–	bbody	1.00	$1.0 \cdot 10^{20}$	–	$1.140 \cdot 10^{-11}$	–
EXOSAT-ME	–	bbody	0.06	$3.0 \cdot 10^{20}$	–	$1.654 \cdot 10^{-16}$	–
EXOSAT-ME	–	bbody	0.10	$3.0 \cdot 10^{20}$	–	$6.695 \cdot 10^{-14}$	–
EXOSAT-ME	–	bbody	0.30	$3.0 \cdot 10^{20}$	–	$4.741 \cdot 10^{-12}$	–
EXOSAT-ME	–	bbody	1.00	$3.0 \cdot 10^{20}$	–	$1.141 \cdot 10^{-11}$	–
EXOSAT-ME	–	bbody	0.06	$1.0 \cdot 10^{21}$	–	$1.857 \cdot 10^{-16}$	–
EXOSAT-ME	–	bbody	0.10	$1.0 \cdot 10^{21}$	–	$7.168 \cdot 10^{-14}$	–
EXOSAT-ME	–	bbody	0.30	$1.0 \cdot 10^{21}$	–	$4.822 \cdot 10^{-12}$	–
EXOSAT-ME	–	bbody	1.00	$1.0 \cdot 10^{21}$	–	$1.145 \cdot 10^{-11}$	–
ROSAT-PSPC	Open	plaw	1.5	$1.0 \cdot 10^{20}$	$8.846 \cdot 10^{-12}$	–	–
ROSAT-PSPC	Open	plaw	2.0	$1.0 \cdot 10^{20}$	$7.043 \cdot 10^{-12}$	–	–
ROSAT-PSPC	Open	plaw	2.5	$1.0 \cdot 10^{20}$	$5.345 \cdot 10^{-12}$	–	–
ROSAT-PSPC	Open	plaw	3.0	$1.0 \cdot 10^{20}$	$3.992 \cdot 10^{-12}$	–	–
ROSAT-PSPC	Open	plaw	3.5	$1.0 \cdot 10^{20}$	$3.014 \cdot 10^{-12}$	–	–
ROSAT-PSPC	Open	plaw	1.5	$3.0 \cdot 10^{20}$	$1.111 \cdot 10^{-11}$	–	–
ROSAT-PSPC	Open	plaw	2.0	$3.0 \cdot 10^{20}$	$1.022 \cdot 10^{-11}$	–	–
ROSAT-PSPC	Open	plaw	2.5	$3.0 \cdot 10^{20}$	$9.066 \cdot 10^{-12}$	–	–
ROSAT-PSPC	Open	plaw	3.0	$3.0 \cdot 10^{20}$	$7.732 \cdot 10^{-12}$	–	–
ROSAT-PSPC	Open	plaw	3.5	$3.0 \cdot 10^{20}$	$6.409 \cdot 10^{-12}$	–	–
ROSAT-PSPC	Open	plaw	1.5	$1.0 \cdot 10^{21}$	$1.208 \cdot 10^{-11}$	–	–
ROSAT-PSPC	Open	plaw	2.0	$1.0 \cdot 10^{21}$	$1.200 \cdot 10^{-11}$	–	–
ROSAT-PSPC	Open	plaw	2.5	$1.0 \cdot 10^{21}$	$1.213 \cdot 10^{-11}$	–	–
ROSAT-PSPC	Open	plaw	3.0	$1.0 \cdot 10^{21}$	$1.244 \cdot 10^{-11}$	–	–
ROSAT-PSPC	Open	plaw	3.5	$1.0 \cdot 10^{21}$	$1.284 \cdot 10^{-11}$	–	–
ROSAT-PSPC	Open	plaw	1.7	$1.0 \cdot 10^{20}$	$8.134 \cdot 10^{-12}$	–	–
ROSAT-PSPC	Open	plaw	1.7	$3.0 \cdot 10^{20}$	$1.078 \cdot 10^{-11}$	–	–
ROSAT-PSPC	Open	plaw	1.7	$1.0 \cdot 10^{21}$	$1.203 \cdot 10^{-11}$	–	–
ROSAT-PSPC	Open	plaw	0.5	$1.0 \cdot 10^{20}$	$1.166 \cdot 10^{-11}$	–	–
ROSAT-PSPC	Open	plaw	1.0	$1.0 \cdot 10^{20}$	$1.043 \cdot 10^{-11}$	–	–
ROSAT-PSPC	Open	plaw	0.5	$3.0 \cdot 10^{20}$	$1.240 \cdot 10^{-11}$	–	–
ROSAT-PSPC	Open	plaw	1.0	$3.0 \cdot 10^{20}$	$1.180 \cdot 10^{-11}$	–	–
ROSAT-PSPC	Open	plaw	0.5	$1.0 \cdot 10^{21}$	$1.278 \cdot 10^{-11}$	–	–
ROSAT-PSPC	Open	plaw	1.0	$1.0 \cdot 10^{21}$	$1.235 \cdot 10^{-11}$	–	–
ROSAT-PSPC	Open	bbody	0.06	$1.0 \cdot 10^{20}$	$3.298 \cdot 10^{-12}$	–	–
ROSAT-PSPC	Open	bbody	0.10	$1.0 \cdot 10^{20}$	$6.930 \cdot 10^{-12}$	–	–

ROSAT-PSPC	Open	bbody	0.30	$1.0 \cdot 10^{20}$	$1.058 \cdot 10^{-11}$	–	–
ROSAT-PSPC	Open	bbody	1.00	$1.0 \cdot 10^{20}$	$1.303 \cdot 10^{-11}$	–	–
ROSAT-PSPC	Open	bbody	0.06	$3.0 \cdot 10^{20}$	$5.994 \cdot 10^{-12}$	–	–
ROSAT-PSPC	Open	bbody	0.10	$3.0 \cdot 10^{20}$	$1.086 \cdot 10^{-11}$	–	–
ROSAT-PSPC	Open	bbody	0.30	$3.0 \cdot 10^{20}$	$1.095 \cdot 10^{-11}$	–	–
ROSAT-PSPC	Open	bbody	1.00	$3.0 \cdot 10^{20}$	$1.321 \cdot 10^{-11}$	–	–
ROSAT-PSPC	Open	bbody	0.06	$1.0 \cdot 10^{21}$	$1.884 \cdot 10^{-11}$	–	–
ROSAT-PSPC	Open	bbody	0.10	$1.0 \cdot 10^{21}$	$1.532 \cdot 10^{-11}$	–	–
ROSAT-PSPC	Open	bbody	0.30	$1.0 \cdot 10^{21}$	$1.095 \cdot 10^{-11}$	–	–
ROSAT-PSPC	Open	bbody	1.00	$1.0 \cdot 10^{21}$	$1.347 \cdot 10^{-11}$	–	–
ROSAT-PSPC	BRN	plaw	1.5	$1.0 \cdot 10^{20}$	$2.152 \cdot 10^{-11}$	–	–
ROSAT-PSPC	BRN	plaw	2.0	$1.0 \cdot 10^{20}$	$2.428 \cdot 10^{-11}$	–	–
ROSAT-PSPC	BRN	plaw	2.5	$1.0 \cdot 10^{20}$	$2.726 \cdot 10^{-11}$	–	–
ROSAT-PSPC	BRN	plaw	3.0	$1.0 \cdot 10^{20}$	$2.878 \cdot 10^{-11}$	–	–
ROSAT-PSPC	BRN	plaw	3.5	$1.0 \cdot 10^{20}$	$2.731 \cdot 10^{-11}$	–	–
ROSAT-PSPC	BRN	plaw	1.5	$3.0 \cdot 10^{20}$	$2.056 \cdot 10^{-11}$	–	–
ROSAT-PSPC	BRN	plaw	2.0	$3.0 \cdot 10^{20}$	$2.337 \cdot 10^{-11}$	–	–
ROSAT-PSPC	BRN	plaw	2.5	$3.0 \cdot 10^{20}$	$2.788 \cdot 10^{-11}$	–	–
ROSAT-PSPC	BRN	plaw	3.0	$3.0 \cdot 10^{20}$	$3.453 \cdot 10^{-11}$	–	–
ROSAT-PSPC	BRN	plaw	3.5	$3.0 \cdot 10^{20}$	$4.321 \cdot 10^{-11}$	–	–
ROSAT-PSPC	BRN	plaw	1.5	$1.0 \cdot 10^{21}$	$1.811 \cdot 10^{-11}$	–	–
ROSAT-PSPC	BRN	plaw	2.0	$1.0 \cdot 10^{21}$	$1.922 \cdot 10^{-11}$	–	–
ROSAT-PSPC	BRN	plaw	2.5	$1.0 \cdot 10^{21}$	$2.111 \cdot 10^{-11}$	–	–
ROSAT-PSPC	BRN	plaw	3.0	$1.0 \cdot 10^{21}$	$2.407 \cdot 10^{-11}$	–	–
ROSAT-PSPC	BRN	plaw	3.5	$1.0 \cdot 10^{21}$	$2.852 \cdot 10^{-11}$	–	–
ROSAT-PSPC	BRN	plaw	1.7	$1.0 \cdot 10^{20}$	$2.253 \cdot 10^{-11}$	–	–
ROSAT-PSPC	BRN	plaw	1.7	$3.0 \cdot 10^{20}$	$2.152 \cdot 10^{-11}$	–	–
ROSAT-PSPC	BRN	plaw	1.7	$1.0 \cdot 10^{21}$	$1.847 \cdot 10^{-11}$	–	–
ROSAT-PSPC	BRN	plaw	0.5	$1.0 \cdot 10^{20}$	$1.852 \cdot 10^{-11}$	–	–
ROSAT-PSPC	BRN	plaw	1.0	$1.0 \cdot 10^{20}$	$1.960 \cdot 10^{-11}$	–	–
ROSAT-PSPC	BRN	plaw	0.5	$3.0 \cdot 10^{20}$	$1.813 \cdot 10^{-11}$	–	–
ROSAT-PSPC	BRN	plaw	1.0	$3.0 \cdot 10^{20}$	$1.894 \cdot 10^{-11}$	–	–
ROSAT-PSPC	BRN	plaw	0.5	$1.0 \cdot 10^{21}$	$1.738 \cdot 10^{-11}$	–	–
ROSAT-PSPC	BRN	plaw	1.0	$1.0 \cdot 10^{21}$	$1.755 \cdot 10^{-11}$	–	–
ROSAT-PSPC	BRN	bbody	0.06	$1.0 \cdot 10^{20}$	$5.716 \cdot 10^{-11}$	–	–
ROSAT-PSPC	BRN	bbody	0.10	$1.0 \cdot 10^{20}$	$6.442 \cdot 10^{-11}$	–	–
ROSAT-PSPC	BRN	bbody	0.30	$1.0 \cdot 10^{20}$	$1.816 \cdot 10^{-11}$	–	–
ROSAT-PSPC	BRN	bbody	1.00	$1.0 \cdot 10^{20}$	$1.758 \cdot 10^{-11}$	–	–
ROSAT-PSPC	BRN	bbody	0.06	$3.0 \cdot 10^{20}$	$1.522 \cdot 10^{-10}$	–	–
ROSAT-PSPC	BRN	bbody	0.10	$3.0 \cdot 10^{20}$	$6.793 \cdot 10^{-11}$	–	–
ROSAT-PSPC	BRN	bbody	0.30	$3.0 \cdot 10^{20}$	$1.756 \cdot 10^{-11}$	–	–
ROSAT-PSPC	BRN	bbody	1.00	$3.0 \cdot 10^{20}$	$1.749 \cdot 10^{-11}$	–	–
ROSAT-PSPC	BRN	bbody	0.06	$1.0 \cdot 10^{21}$	$1.677 \cdot 10^{-10}$	–	–
ROSAT-PSPC	BRN	bbody	0.10	$1.0 \cdot 10^{21}$	$4.698 \cdot 10^{-11}$	–	–
ROSAT-PSPC	BRN	bbody	0.30	$1.0 \cdot 10^{21}$	$1.633 \cdot 10^{-11}$	–	–
ROSAT-PSPC	BRN	bbody	1.00	$1.0 \cdot 10^{21}$	$1.736 \cdot 10^{-11}$	–	–
ROSAT-HRI	–	plaw	1.5	$1.0 \cdot 10^{20}$	$3.014 \cdot 10^{-11}$	–	–
ROSAT-HRI	–	plaw	2.0	$1.0 \cdot 10^{20}$	$2.792 \cdot 10^{-11}$	–	–
ROSAT-HRI	–	plaw	2.5	$1.0 \cdot 10^{20}$	$2.510 \cdot 10^{-11}$	–	–
ROSAT-HRI	–	plaw	3.0	$1.0 \cdot 10^{20}$	$2.185 \cdot 10^{-11}$	–	–
ROSAT-HRI	–	plaw	3.5	$1.0 \cdot 10^{20}$	$1.859 \cdot 10^{-11}$	–	–
ROSAT-HRI	–	plaw	1.5	$3.0 \cdot 10^{20}$	$3.215 \cdot 10^{-11}$	–	–
ROSAT-HRI	–	plaw	2.0	$3.0 \cdot 10^{20}$	$3.155 \cdot 10^{-11}$	–	–
ROSAT-HRI	–	plaw	2.5	$3.0 \cdot 10^{20}$	$3.093 \cdot 10^{-11}$	–	–
ROSAT-HRI	–	plaw	3.0	$3.0 \cdot 10^{20}$	$2.991 \cdot 10^{-11}$	–	–
ROSAT-HRI	–	plaw	3.5	$3.0 \cdot 10^{20}$	$2.825 \cdot 10^{-11}$	–	–
ROSAT-HRI	–	plaw	1.5	$1.0 \cdot 10^{21}$	$3.230 \cdot 10^{-11}$	–	–
ROSAT-HRI	–	plaw	2.0	$1.0 \cdot 10^{21}$	$3.187 \cdot 10^{-11}$	–	–
ROSAT-HRI	–	plaw	2.5	$1.0 \cdot 10^{21}$	$3.213 \cdot 10^{-11}$	–	–
ROSAT-HRI	–	plaw	3.0	$1.0 \cdot 10^{21}$	$3.305 \cdot 10^{-11}$	–	–
ROSAT-HRI	–	plaw	3.5	$1.0 \cdot 10^{21}$	$3.450 \cdot 10^{-11}$	–	–
ROSAT-HRI	–	plaw	1.7	$1.0 \cdot 10^{20}$	$2.931 \cdot 10^{-11}$	–	–
ROSAT-HRI	–	plaw	1.7	$3.0 \cdot 10^{20}$	$3.189 \cdot 10^{-11}$	–	–
ROSAT-HRI	–	plaw	1.7	$1.0 \cdot 10^{21}$	$3.204 \cdot 10^{-11}$	–	–
ROSAT-HRI	–	plaw	0.5	$1.0 \cdot 10^{20}$	$3.383 \cdot 10^{-11}$	–	–
ROSAT-HRI	–	plaw	1.0	$1.0 \cdot 10^{20}$	$3.199 \cdot 10^{-11}$	–	–
ROSAT-HRI	–	plaw	0.5	$3.0 \cdot 10^{20}$	$3.444 \cdot 10^{-11}$	–	–
ROSAT-HRI	–	plaw	1.0	$3.0 \cdot 10^{20}$	$3.306 \cdot 10^{-11}$	–	–
ROSAT-HRI	–	plaw	0.5	$1.0 \cdot 10^{21}$	$3.501 \cdot 10^{-11}$	–	–
ROSAT-HRI	–	plaw	1.0	$1.0 \cdot 10^{21}$	$3.337 \cdot 10^{-11}$	–	–
ROSAT-HRI	–	bbody	0.06	$1.0 \cdot 10^{20}$	$2.040 \cdot 10^{-11}$	–	–
ROSAT-HRI	–	bbody	0.10	$1.0 \cdot 10^{20}$	$3.149 \cdot 10^{-11}$	–	–
ROSAT-HRI	–	bbody	0.30	$1.0 \cdot 10^{20}$	$2.902 \cdot 10^{-11}$	–	–
ROSAT-HRI	–	bbody	1.00	$1.0 \cdot 10^{20}$	$3.650 \cdot 10^{-11}$	–	–

ROSAT-HRI	–	bbody	0.06	$3.0 \cdot 10^{20}$	$2.956 \cdot 10^{-11}$	–	–
ROSAT-HRI	–	bbody	0.10	$3.0 \cdot 10^{20}$	$3.818 \cdot 10^{-11}$	–	–
ROSAT-HRI	–	bbody	0.30	$3.0 \cdot 10^{20}$	$2.904 \cdot 10^{-11}$	–	–
ROSAT-HRI	–	bbody	1.00	$3.0 \cdot 10^{20}$	$3.680 \cdot 10^{-11}$	–	–
ROSAT-HRI	–	bbody	0.06	$1.0 \cdot 10^{21}$	$4.975 \cdot 10^{-11}$	–	–
ROSAT-HRI	–	bbody	0.10	$1.0 \cdot 10^{21}$	$4.090 \cdot 10^{-11}$	–	–
ROSAT-HRI	–	bbody	0.30	$1.0 \cdot 10^{21}$	$2.856 \cdot 10^{-11}$	–	–
ROSAT-HRI	–	bbody	1.00	$1.0 \cdot 10^{21}$	$3.768 \cdot 10^{-11}$	–	–
EINSTEIN	IPC	plaw	1.5	$1.0 \cdot 10^{20}$	$1.685 \cdot 10^{-11}$	–	–
EINSTEIN	IPC	plaw	2.0	$1.0 \cdot 10^{20}$	$1.680 \cdot 10^{-11}$	–	–
EINSTEIN	IPC	plaw	2.5	$1.0 \cdot 10^{20}$	$1.528 \cdot 10^{-11}$	–	–
EINSTEIN	IPC	plaw	3.0	$1.0 \cdot 10^{20}$	$1.298 \cdot 10^{-11}$	–	–
EINSTEIN	IPC	plaw	3.5	$1.0 \cdot 10^{20}$	$1.070 \cdot 10^{-11}$	–	–
EINSTEIN	IPC	plaw	1.5	$3.0 \cdot 10^{20}$	$1.784 \cdot 10^{-11}$	–	–
EINSTEIN	IPC	plaw	2.0	$3.0 \cdot 10^{20}$	$1.954 \cdot 10^{-11}$	–	–
EINSTEIN	IPC	plaw	2.5	$3.0 \cdot 10^{20}$	$2.022 \cdot 10^{-11}$	–	–
EINSTEIN	IPC	plaw	3.0	$3.0 \cdot 10^{20}$	$1.961 \cdot 10^{-11}$	–	–
EINSTEIN	IPC	plaw	3.5	$3.0 \cdot 10^{20}$	$1.793 \cdot 10^{-11}$	–	–
EINSTEIN	IPC	plaw	1.5	$1.0 \cdot 10^{21}$	$1.685 \cdot 10^{-11}$	–	–
EINSTEIN	IPC	plaw	2.0	$1.0 \cdot 10^{21}$	$1.912 \cdot 10^{-11}$	–	–
EINSTEIN	IPC	plaw	2.5	$1.0 \cdot 10^{21}$	$2.147 \cdot 10^{-11}$	–	–
EINSTEIN	IPC	plaw	3.0	$1.0 \cdot 10^{21}$	$2.391 \cdot 10^{-11}$	–	–
EINSTEIN	IPC	plaw	3.5	$1.0 \cdot 10^{21}$	$2.636 \cdot 10^{-11}$	–	–
EINSTEIN	IPC	plaw	1.7	$1.0 \cdot 10^{20}$	$1.702 \cdot 10^{-11}$	–	–
EINSTEIN	IPC	plaw	1.7	$3.0 \cdot 10^{20}$	$1.861 \cdot 10^{-11}$	–	–
EINSTEIN	IPC	plaw	1.7	$1.0 \cdot 10^{21}$	$1.775 \cdot 10^{-11}$	–	–
EINSTEIN	IPC	plaw	0.5	$1.0 \cdot 10^{20}$	$1.350 \cdot 10^{-11}$	–	–
EINSTEIN	IPC	plaw	1.0	$1.0 \cdot 10^{20}$	$1.553 \cdot 10^{-11}$	–	–
EINSTEIN	IPC	plaw	0.5	$3.0 \cdot 10^{20}$	$1.334 \cdot 10^{-11}$	–	–
EINSTEIN	IPC	plaw	1.0	$3.0 \cdot 10^{20}$	$1.565 \cdot 10^{-11}$	–	–
EINSTEIN	IPC	plaw	0.5	$1.0 \cdot 10^{21}$	$1.252 \cdot 10^{-11}$	–	–
EINSTEIN	IPC	plaw	1.0	$1.0 \cdot 10^{21}$	$1.465 \cdot 10^{-11}$	–	–
EINSTEIN	IPC	bbody	0.06	$1.0 \cdot 10^{20}$	$1.140 \cdot 10^{-11}$	–	–
EINSTEIN	IPC	bbody	0.10	$1.0 \cdot 10^{20}$	$2.031 \cdot 10^{-11}$	–	–
EINSTEIN	IPC	bbody	0.30	$1.0 \cdot 10^{20}$	$2.116 \cdot 10^{-11}$	–	–
EINSTEIN	IPC	bbody	1.00	$1.0 \cdot 10^{20}$	$1.230 \cdot 10^{-11}$	–	–
EINSTEIN	IPC	bbody	0.06	$3.0 \cdot 10^{20}$	$1.837 \cdot 10^{-11}$	–	–
EINSTEIN	IPC	bbody	0.10	$3.0 \cdot 10^{20}$	$2.747 \cdot 10^{-11}$	–	–
EINSTEIN	IPC	bbody	0.30	$3.0 \cdot 10^{20}$	$2.127 \cdot 10^{-11}$	–	–
EINSTEIN	IPC	bbody	1.00	$3.0 \cdot 10^{20}$	$1.214 \cdot 10^{-11}$	–	–
EINSTEIN	IPC	bbody	0.06	$1.0 \cdot 10^{21}$	$4.744 \cdot 10^{-11}$	–	–
EINSTEIN	IPC	bbody	0.10	$1.0 \cdot 10^{21}$	$3.254 \cdot 10^{-11}$	–	–
EINSTEIN	IPC	bbody	0.30	$1.0 \cdot 10^{21}$	$2.064 \cdot 10^{-11}$	–	–
EINSTEIN	IPC	bbody	1.00	$1.0 \cdot 10^{21}$	$1.163 \cdot 10^{-11}$	–	–
EINSTEIN	HRI	plaw	1.5	$1.0 \cdot 10^{20}$	$5.823 \cdot 10^{-11}$	–	–
EINSTEIN	HRI	plaw	2.0	$1.0 \cdot 10^{20}$	$4.721 \cdot 10^{-11}$	–	–
EINSTEIN	HRI	plaw	2.5	$1.0 \cdot 10^{20}$	$3.738 \cdot 10^{-11}$	–	–
EINSTEIN	HRI	plaw	3.0	$1.0 \cdot 10^{20}$	$2.954 \cdot 10^{-11}$	–	–
EINSTEIN	HRI	plaw	3.5	$1.0 \cdot 10^{20}$	$2.358 \cdot 10^{-11}$	–	–
EINSTEIN	HRI	plaw	1.5	$3.0 \cdot 10^{20}$	$6.925 \cdot 10^{-11}$	–	–
EINSTEIN	HRI	plaw	2.0	$3.0 \cdot 10^{20}$	$6.125 \cdot 10^{-11}$	–	–
EINSTEIN	HRI	plaw	2.5	$3.0 \cdot 10^{20}$	$5.335 \cdot 10^{-11}$	–	–
EINSTEIN	HRI	plaw	3.0	$3.0 \cdot 10^{20}$	$4.625 \cdot 10^{-11}$	–	–
EINSTEIN	HRI	plaw	3.5	$3.0 \cdot 10^{20}$	$4.014 \cdot 10^{-11}$	–	–
EINSTEIN	HRI	plaw	1.5	$1.0 \cdot 10^{21}$	$7.962 \cdot 10^{-11}$	–	–
EINSTEIN	HRI	plaw	2.0	$1.0 \cdot 10^{21}$	$7.396 \cdot 10^{-11}$	–	–
EINSTEIN	HRI	plaw	2.5	$1.0 \cdot 10^{21}$	$6.805 \cdot 10^{-11}$	–	–
EINSTEIN	HRI	plaw	3.0	$1.0 \cdot 10^{21}$	$6.286 \cdot 10^{-11}$	–	–
EINSTEIN	HRI	plaw	3.5	$1.0 \cdot 10^{21}$	$5.881 \cdot 10^{-11}$	–	–
EINSTEIN	HRI	plaw	1.7	$1.0 \cdot 10^{20}$	$5.378 \cdot 10^{-11}$	–	–
EINSTEIN	HRI	plaw	1.7	$3.0 \cdot 10^{20}$	$6.612 \cdot 10^{-11}$	–	–
EINSTEIN	HRI	plaw	1.7	$1.0 \cdot 10^{21}$	$7.747 \cdot 10^{-11}$	–	–
EINSTEIN	HRI	plaw	0.5	$1.0 \cdot 10^{20}$	$7.531 \cdot 10^{-11}$	–	–
EINSTEIN	HRI	plaw	1.0	$1.0 \cdot 10^{20}$	$6.848 \cdot 10^{-11}$	–	–
EINSTEIN	HRI	plaw	0.5	$3.0 \cdot 10^{20}$	$7.954 \cdot 10^{-11}$	–	–
EINSTEIN	HRI	plaw	1.0	$3.0 \cdot 10^{20}$	$7.596 \cdot 10^{-11}$	–	–
EINSTEIN	HRI	plaw	0.5	$1.0 \cdot 10^{21}$	$8.408 \cdot 10^{-11}$	–	–
EINSTEIN	HRI	plaw	1.0	$1.0 \cdot 10^{21}$	$8.352 \cdot 10^{-11}$	–	–
EINSTEIN	HRI	bbody	0.06	$1.0 \cdot 10^{20}$	$2.533 \cdot 10^{-11}$	–	–
EINSTEIN	HRI	bbody	0.10	$1.0 \cdot 10^{20}$	$3.846 \cdot 10^{-11}$	–	–
EINSTEIN	HRI	bbody	0.30	$1.0 \cdot 10^{20}$	$7.361 \cdot 10^{-11}$	–	–
EINSTEIN	HRI	bbody	1.00	$1.0 \cdot 10^{20}$	$8.805 \cdot 10^{-11}$	–	–
EINSTEIN	HRI	bbody	0.06	$3.0 \cdot 10^{20}$	$3.781 \cdot 10^{-11}$	–	–
EINSTEIN	HRI	bbody	0.10	$3.0 \cdot 10^{20}$	$4.637 \cdot 10^{-11}$	–	–

EINSTEIN	HRI	bbody	0.30	$3.0 \cdot 10^{20}$	$7.771 \cdot 10^{-11}$	–	–
EINSTEIN	HRI	bbody	1.00	$3.0 \cdot 10^{20}$	$8.932 \cdot 10^{-11}$	–	–
EINSTEIN	HRI	bbody	0.06	$1.0 \cdot 10^{21}$	$5.418 \cdot 10^{-11}$	–	–
EINSTEIN	HRI	bbody	0.10	$1.0 \cdot 10^{21}$	$4.908 \cdot 10^{-11}$	–	–
EINSTEIN	HRI	bbody	0.30	$1.0 \cdot 10^{21}$	$8.540 \cdot 10^{-11}$	–	–
EINSTEIN	HRI	bbody	1.00	$1.0 \cdot 10^{21}$	$9.132 \cdot 10^{-11}$	–	–
GINGA-LAC	Top	plaw	1.5	$1.0 \cdot 10^{20}$	–	$3.087 \cdot 10^{-12}$	–
GINGA-LAC	Top	plaw	2.0	$1.0 \cdot 10^{20}$	–	$2.693 \cdot 10^{-12}$	–
GINGA-LAC	Top	plaw	2.5	$1.0 \cdot 10^{20}$	–	$2.386 \cdot 10^{-12}$	–
GINGA-LAC	Top	plaw	3.0	$1.0 \cdot 10^{20}$	–	$2.147 \cdot 10^{-12}$	–
GINGA-LAC	Top	plaw	3.5	$1.0 \cdot 10^{20}$	–	$1.956 \cdot 10^{-12}$	–
GINGA-LAC	Top	plaw	1.5	$3.0 \cdot 10^{20}$	–	$3.090 \cdot 10^{-12}$	–
GINGA-LAC	Top	plaw	2.0	$3.0 \cdot 10^{20}$	–	$2.696 \cdot 10^{-12}$	–
GINGA-LAC	Top	plaw	2.5	$3.0 \cdot 10^{20}$	–	$2.389 \cdot 10^{-12}$	–
GINGA-LAC	Top	plaw	3.0	$3.0 \cdot 10^{20}$	–	$2.151 \cdot 10^{-12}$	–
GINGA-LAC	Top	plaw	3.5	$3.0 \cdot 10^{20}$	–	$1.960 \cdot 10^{-12}$	–
GINGA-LAC	Top	plaw	1.5	$1.0 \cdot 10^{21}$	–	$3.101 \cdot 10^{-12}$	–
GINGA-LAC	Top	plaw	2.0	$1.0 \cdot 10^{21}$	–	$2.706 \cdot 10^{-12}$	–
GINGA-LAC	Top	plaw	2.5	$1.0 \cdot 10^{21}$	–	$2.400 \cdot 10^{-12}$	–
GINGA-LAC	Top	plaw	3.0	$1.0 \cdot 10^{21}$	–	$2.162 \cdot 10^{-12}$	–
GINGA-LAC	Top	plaw	3.5	$1.0 \cdot 10^{21}$	–	$1.972 \cdot 10^{-12}$	–
GINGA-LAC	Top	plaw	1.7	$1.0 \cdot 10^{20}$	–	$2.918 \cdot 10^{-12}$	–
GINGA-LAC	Top	plaw	1.7	$3.0 \cdot 10^{20}$	–	$2.921 \cdot 10^{-12}$	–
GINGA-LAC	Top	plaw	1.7	$1.0 \cdot 10^{21}$	–	$2.931 \cdot 10^{-12}$	–
GINGA-LAC	Top	plaw	0.5	$1.0 \cdot 10^{20}$	–	$4.201 \cdot 10^{-12}$	–
GINGA-LAC	Top	plaw	1.0	$1.0 \cdot 10^{20}$	–	$3.586 \cdot 10^{-12}$	–
GINGA-LAC	Top	plaw	0.5	$3.0 \cdot 10^{20}$	–	$4.204 \cdot 10^{-12}$	–
GINGA-LAC	Top	plaw	1.0	$3.0 \cdot 10^{20}$	–	$3.589 \cdot 10^{-12}$	–
GINGA-LAC	Top	plaw	0.5	$1.0 \cdot 10^{21}$	–	$4.214 \cdot 10^{-12}$	–
GINGA-LAC	Top	plaw	1.0	$1.0 \cdot 10^{21}$	–	$3.599 \cdot 10^{-12}$	–
GINGA-LAC	Top	bbody	0.06	$1.0 \cdot 10^{20}$	–	$5.096 \cdot 10^{-16}$	–
GINGA-LAC	Top	bbody	0.10	$1.0 \cdot 10^{20}$	–	$6.202 \cdot 10^{-14}$	–
GINGA-LAC	Top	bbody	0.30	$1.0 \cdot 10^{20}$	–	$1.460 \cdot 10^{-12}$	–
GINGA-LAC	Top	bbody	1.00	$1.0 \cdot 10^{20}$	–	$2.258 \cdot 10^{-12}$	–
GINGA-LAC	Top	bbody	0.06	$3.0 \cdot 10^{20}$	–	$5.194 \cdot 10^{-16}$	–
GINGA-LAC	Top	bbody	0.10	$3.0 \cdot 10^{20}$	–	$6.275 \cdot 10^{-14}$	–
GINGA-LAC	Top	bbody	0.30	$3.0 \cdot 10^{20}$	–	$1.464 \cdot 10^{-12}$	–
GINGA-LAC	Top	bbody	1.00	$3.0 \cdot 10^{20}$	–	$2.259 \cdot 10^{-12}$	–
GINGA-LAC	Top	bbody	0.06	$1.0 \cdot 10^{21}$	–	$5.548 \cdot 10^{-16}$	–
GINGA-LAC	Top	bbody	0.10	$1.0 \cdot 10^{21}$	–	$6.533 \cdot 10^{-14}$	–
GINGA-LAC	Top	bbody	0.30	$1.0 \cdot 10^{21}$	–	$1.477 \cdot 10^{-12}$	–
GINGA-LAC	Top	bbody	1.00	$1.0 \cdot 10^{21}$	–	$2.262 \cdot 10^{-12}$	–
ASCA	SIS	plaw	1.5	$1.0 \cdot 10^{20}$	–	–	$1.116 \cdot 10^{-10}$
ASCA	SIS	plaw	2.0	$1.0 \cdot 10^{20}$	–	–	$4.134 \cdot 10^{-11}$
ASCA	SIS	plaw	2.5	$1.0 \cdot 10^{20}$	–	–	$1.949 \cdot 10^{-11}$
ASCA	SIS	plaw	3.0	$1.0 \cdot 10^{20}$	–	–	$1.119 \cdot 10^{-11}$
ASCA	SIS	plaw	3.5	$1.0 \cdot 10^{20}$	–	–	$7.149 \cdot 10^{-12}$
ASCA	SIS	plaw	1.5	$3.0 \cdot 10^{20}$	–	–	$1.149 \cdot 10^{-10}$
ASCA	SIS	plaw	2.0	$3.0 \cdot 10^{20}$	–	–	$4.293 \cdot 10^{-11}$
ASCA	SIS	plaw	2.5	$3.0 \cdot 10^{20}$	–	–	$2.044 \cdot 10^{-11}$
ASCA	SIS	plaw	3.0	$3.0 \cdot 10^{20}$	–	–	$1.188 \cdot 10^{-11}$
ASCA	SIS	plaw	3.5	$3.0 \cdot 10^{20}$	–	–	$7.690 \cdot 10^{-12}$
ASCA	SIS	plaw	1.5	$1.0 \cdot 10^{21}$	–	–	$1.254 \cdot 10^{-10}$
ASCA	SIS	plaw	2.0	$1.0 \cdot 10^{21}$	–	–	$4.815 \cdot 10^{-11}$
ASCA	SIS	plaw	2.5	$1.0 \cdot 10^{21}$	–	–	$2.358 \cdot 10^{-11}$
ASCA	SIS	plaw	3.0	$1.0 \cdot 10^{21}$	–	–	$1.416 \cdot 10^{-11}$
ASCA	SIS	plaw	3.5	$1.0 \cdot 10^{21}$	–	–	$9.533 \cdot 10^{-12}$
ASCA	SIS	plaw	1.7	$1.0 \cdot 10^{20}$	–	–	$4.284 \cdot 10^{-11}$
ASCA	SIS	plaw	1.7	$3.0 \cdot 10^{20}$	–	–	$4.190 \cdot 10^{-11}$
ASCA	SIS	plaw	1.7	$1.0 \cdot 10^{21}$	–	–	$4.211 \cdot 10^{-11}$
ASCA	SIS	plaw	0.5	$1.0 \cdot 10^{20}$	–	–	$1.059 \cdot 10^{-10}$
ASCA	SIS	plaw	1.0	$1.0 \cdot 10^{20}$	–	–	$6.908 \cdot 10^{-11}$
ASCA	SIS	plaw	0.5	$3.0 \cdot 10^{20}$	–	–	$1.069 \cdot 10^{-10}$
ASCA	SIS	plaw	1.0	$3.0 \cdot 10^{20}$	–	–	$6.959 \cdot 10^{-11}$
ASCA	SIS	plaw	0.5	$1.0 \cdot 10^{21}$	–	–	$1.103 \cdot 10^{-10}$
ASCA	SIS	plaw	1.0	$1.0 \cdot 10^{21}$	–	–	$7.215 \cdot 10^{-11}$
ASCA	SIS	bbody	0.06	$1.0 \cdot 10^{20}$	–	–	$1.461 \cdot 10^{-14}$
ASCA	SIS	bbody	0.10	$1.0 \cdot 10^{20}$	–	–	$7.053 \cdot 10^{-13}$
ASCA	SIS	bbody	0.30	$1.0 \cdot 10^{20}$	–	–	$1.081 \cdot 10^{-11}$
ASCA	SIS	bbody	1.00	$1.0 \cdot 10^{20}$	–	–	$3.896 \cdot 10^{-11}$
ASCA	SIS	bbody	0.06	$3.0 \cdot 10^{20}$	–	–	$1.709 \cdot 10^{-14}$
ASCA	SIS	bbody	0.10	$3.0 \cdot 10^{20}$	–	–	$7.812 \cdot 10^{-13}$
ASCA	SIS	bbody	0.30	$3.0 \cdot 10^{20}$	–	–	$1.106 \cdot 10^{-11}$
ASCA	SIS	bbody	1.00	$3.0 \cdot 10^{20}$	–	–	$3.929 \cdot 10^{-11}$

ASCA	SIS	bbody	0.06	$1.0 \cdot 10^{21}$	–	–	$2.854 \cdot 10^{-14}$
ASCA	SIS	bbody	0.10	$1.0 \cdot 10^{21}$	–	–	$1.078 \cdot 10^{-12}$
ASCA	SIS	bbody	0.30	$1.0 \cdot 10^{21}$	–	–	$1.188 \cdot 10^{-11}$
ASCA	SIS	bbody	1.00	$1.0 \cdot 10^{21}$	–	–	$4.039 \cdot 10^{-11}$
ASCA	GIS	plaw	1.5	$1.0 \cdot 10^{20}$	$1.035 \cdot 10^{-10}$	$2.822 \cdot 10^{-11}$	$1.317 \cdot 10^{-10}$
ASCA	GIS	plaw	2.0	$1.0 \cdot 10^{20}$	$3.285 \cdot 10^{-11}$	$2.544 \cdot 10^{-11}$	$5.830 \cdot 10^{-11}$
ASCA	GIS	plaw	2.5	$1.0 \cdot 10^{20}$	$1.075 \cdot 10^{-11}$	$2.266 \cdot 10^{-11}$	$3.341 \cdot 10^{-11}$
ASCA	GIS	plaw	3.0	$1.0 \cdot 10^{20}$	$3.654 \cdot 10^{-12}$	$2.015 \cdot 10^{-11}$	$2.380 \cdot 10^{-11}$
ASCA	GIS	plaw	3.5	$1.0 \cdot 10^{20}$	$1.283 \cdot 10^{-12}$	$1.799 \cdot 10^{-11}$	$1.927 \cdot 10^{-11}$
ASCA	GIS	plaw	1.5	$3.0 \cdot 10^{20}$	$1.048 \cdot 10^{-10}$	$2.837 \cdot 10^{-11}$	$1.332 \cdot 10^{-10}$
ASCA	GIS	plaw	2.0	$3.0 \cdot 10^{20}$	$3.340 \cdot 10^{-11}$	$2.562 \cdot 10^{-11}$	$5.902 \cdot 10^{-11}$
ASCA	GIS	plaw	2.5	$3.0 \cdot 10^{20}$	$1.098 \cdot 10^{-11}$	$2.286 \cdot 10^{-11}$	$3.383 \cdot 10^{-11}$
ASCA	GIS	plaw	3.0	$3.0 \cdot 10^{20}$	$3.746 \cdot 10^{-12}$	$2.036 \cdot 10^{-11}$	$2.410 \cdot 10^{-11}$
ASCA	GIS	plaw	3.5	$3.0 \cdot 10^{20}$	$1.321 \cdot 10^{-12}$	$1.820 \cdot 10^{-11}$	$1.952 \cdot 10^{-11}$
ASCA	GIS	plaw	1.5	$1.0 \cdot 10^{21}$	$1.092 \cdot 10^{-10}$	$2.887 \cdot 10^{-11}$	$1.381 \cdot 10^{-10}$
ASCA	GIS	plaw	2.0	$1.0 \cdot 10^{21}$	$3.527 \cdot 10^{-11}$	$2.621 \cdot 10^{-11}$	$6.149 \cdot 10^{-11}$
ASCA	GIS	plaw	2.5	$1.0 \cdot 10^{21}$	$1.176 \cdot 10^{-11}$	$2.351 \cdot 10^{-11}$	$3.527 \cdot 10^{-11}$
ASCA	GIS	plaw	3.0	$1.0 \cdot 10^{21}$	$4.070 \cdot 10^{-12}$	$2.105 \cdot 10^{-11}$	$2.512 \cdot 10^{-11}$
ASCA	GIS	plaw	3.5	$1.0 \cdot 10^{21}$	$1.456 \cdot 10^{-12}$	$1.892 \cdot 10^{-11}$	$2.038 \cdot 10^{-11}$
ASCA	GIS	plaw	1.7	$1.0 \cdot 10^{20}$	$2.099 \cdot 10^{-11}$	$3.320 \cdot 10^{-11}$	$5.418 \cdot 10^{-11}$
ASCA	GIS	plaw	1.7	$3.0 \cdot 10^{20}$	$1.830 \cdot 10^{-11}$	$3.361 \cdot 10^{-11}$	$5.191 \cdot 10^{-11}$
ASCA	GIS	plaw	1.7	$1.0 \cdot 10^{21}$	$1.410 \cdot 10^{-11}$	$3.504 \cdot 10^{-11}$	$4.914 \cdot 10^{-11}$
ASCA	GIS	plaw	0.5	$1.0 \cdot 10^{20}$	$5.817 \cdot 10^{-12}$	$8.544 \cdot 10^{-11}$	$9.126 \cdot 10^{-11}$
ASCA	GIS	plaw	1.0	$1.0 \cdot 10^{20}$	$1.005 \cdot 10^{-11}$	$5.914 \cdot 10^{-11}$	$6.919 \cdot 10^{-11}$
ASCA	GIS	plaw	0.5	$3.0 \cdot 10^{20}$	$5.502 \cdot 10^{-12}$	$8.590 \cdot 10^{-11}$	$9.140 \cdot 10^{-11}$
ASCA	GIS	plaw	1.0	$3.0 \cdot 10^{20}$	$9.279 \cdot 10^{-12}$	$5.961 \cdot 10^{-11}$	$6.889 \cdot 10^{-11}$
ASCA	GIS	plaw	0.5	$1.0 \cdot 10^{21}$	$4.805 \cdot 10^{-12}$	$8.745 \cdot 10^{-11}$	$9.225 \cdot 10^{-11}$
ASCA	GIS	plaw	1.0	$1.0 \cdot 10^{21}$	$7.794 \cdot 10^{-12}$	$6.121 \cdot 10^{-11}$	$6.900 \cdot 10^{-11}$
ASCA	GIS	bbody	0.10	$1.0 \cdot 10^{20}$	$3.335 \cdot 10^{-32}$	$6.258 \cdot 10^{-12}$	$6.258 \cdot 10^{-12}$
ASCA	GIS	bbody	0.30	$1.0 \cdot 10^{20}$	$5.904 \cdot 10^{-17}$	$1.791 \cdot 10^{-11}$	$1.791 \cdot 10^{-11}$
ASCA	GIS	bbody	1.00	$1.0 \cdot 10^{20}$	$4.954 \cdot 10^{-12}$	$3.336 \cdot 10^{-11}$	$3.831 \cdot 10^{-11}$
ASCA	GIS	bbody	0.10	$3.0 \cdot 10^{20}$	$3.551 \cdot 10^{-32}$	$6.444 \cdot 10^{-12}$	$6.444 \cdot 10^{-12}$
ASCA	GIS	bbody	0.30	$3.0 \cdot 10^{20}$	$6.052 \cdot 10^{-17}$	$1.801 \cdot 10^{-11}$	$1.802 \cdot 10^{-11}$
ASCA	GIS	bbody	1.00	$3.0 \cdot 10^{20}$	$4.992 \cdot 10^{-12}$	$3.346 \cdot 10^{-11}$	$3.845 \cdot 10^{-11}$
ASCA	GIS	bbody	0.10	$1.0 \cdot 10^{21}$	$4.396 \cdot 10^{-32}$	$7.101 \cdot 10^{-12}$	$7.101 \cdot 10^{-12}$
ASCA	GIS	bbody	0.30	$1.0 \cdot 10^{21}$	$6.584 \cdot 10^{-17}$	$1.835 \cdot 10^{-11}$	$1.835 \cdot 10^{-11}$
ASCA	GIS	bbody	1.00	$1.0 \cdot 10^{21}$	$5.126 \cdot 10^{-12}$	$3.381 \cdot 10^{-11}$	$3.894 \cdot 10^{-11}$
HEAO-1	A2	–	–	$1.0 \cdot 10^{20}$	–	$(2.17 \cdot 2.868/2.574 \pm 0.4) \cdot 10^{-11}$	–
HEAO-1	A2	–	–	$3.0 \cdot 10^{20}$	–	$(2.17 \cdot 2.863/2.569 \pm 0.4) \cdot 10^{-11}$	–
HEAO-1	A2	–	–	$1.0 \cdot 10^{21}$	–	$(2.17 \cdot 2.843/2.550 \pm 0.4) \cdot 10^{-11}$	–
ARIEL5	–	–	–	$1.0 \cdot 10^{20}$	–	$(1 \pm 0.15) \cdot 5.3 \cdot 10^{-11} \cdot 2.868/2.574$	–
ARIEL5	–	–	–	$3.0 \cdot 10^{20}$	–	$(1 \pm 0.15) \cdot 5.3 \cdot 10^{-11} \cdot 2.863/2.569$	–
ARIEL5	–	–	–	$1.0 \cdot 10^{21}$	–	$(1 \pm 0.15) \cdot 5.3 \cdot 10^{-11} \cdot 2.844/2.550$	–
UHURU	–	–	–	$1.0 \cdot 10^{20}$	–	$(1 \pm 0.2) \cdot 1.7 \cdot 10^{-11} \cdot 2.868/1.758$	–
UHURU	–	–	–	$3.0 \cdot 10^{20}$	–	$(1 \pm 0.2) \cdot 1.7 \cdot 10^{-11} \cdot 2.863/1.753$	–
UHURU	–	–	–	$1.0 \cdot 10^{21}$	–	$(1 \pm 0.2) \cdot 1.7 \cdot 10^{-11} \cdot 2.844/1.735$	–
Vela5B	–	–	–	$1.0 \cdot 10^{20}$	–	$(6 \cdot 2.868/2.220 \pm 0.4) \cdot 10^{-10}$	–
Vela5B	–	–	–	$3.0 \cdot 10^{20}$	–	$(6 \cdot 2.863/2.218 \pm 0.4) \cdot 10^{-10}$	–
Vela5B	–	–	–	$1.0 \cdot 10^{21}$	–	$(6 \cdot 2.843/2.212 \pm 0.4) \cdot 10^{-10}$	–

Erklärung

Hiermit bestätige ich, dass ich diese Arbeit selbstständig und nur unter Verwendung der angegebenen Hilfsmittel angefertigt habe.

Ort, Datum	Ole König